2020

Classical Engineering Systems Provide Behavioral Analog for Ephemeral Insect and Plant Biomechanics

Nicholas Smith
University of Central Florida

CLASSICAL ENGINEERING SYSTEMS PROVIDE BEHAVIORAL ANALOG FOR EPHEMERAL INSECT AND PLANT BIOMECHANICS

by

NICHOLAS SMITH
B.S. FAMU-FSU College of Engineering, 2016
M.S. University of Central Florida, 2019

A dissertation submitted in partial fulfilment of the requirements
for the degree of Doctor of Philosophy
in the Department of Mechanical and Aerospace Engineering
in the College of Engineering and Computer Sciences
at the University of Central Florida
Orlando, Florida

Summer Term
2020

Major Professor: Andrew Dickerson

ABSTRACT

In this dissertation we consider ephemeral behaviors of two small-scale living systems, mosquitoes and citrus fruit reservoirs. While these two systems share few obvious commonalities, they both express life events that are complex and conclude within approximately 50 milliseconds. We utilize high-speed videography, between 1,000-16,000 fps, to detail how complex behavior can be modeled as classical engineering systems. Beginning with the larger organism we assessed the landing and takeoff behavior of *Aedes aegypti* mosquitoes to ascertain the secrets of their covert interaction with humans. At takeoff, mosquitoes decrease pushing contact time with substrates of low friction through a modified takeoff behavior of striking the substrate with a hind-leg prior to a classic push phase. We propose a 2D analog where the striking leg acts as a rotating cantilever about a fixed end that generates upward momentum with a small penalty in body rotation. Landing mosquitoes are filmed in 2D and modeled as a mass-spring-damper system whose natural frequency, damping coefficient, ratio, and spring constant are determined experimentally and validated through a nonlinear least square solver fitting of the free vibration ODE's general solution. Results indicate mosquitoes behave as an underdamped system to scrub their incoming momentum through extending impact duration, effectively reducing temporal impact force. Shrinking in scale we proceed to characterize citrus reservoir rupture as a passive system capable of microjetting oil through expanding orifices at accelerations greater than 5000 gravities. Citrus reservoirs are modeled as ellipsoidal pressure vessels capped by a thin membrane of contrasting stiffness to the surrounding ductile compressible albedo.

To my wife,

Bethany Grace Smith,

the greatest source of motivation in my career,

may our next journey be accompanied with less entropy.

ACKNOWLEDGMENTS

I acknowledge the following for their contribution to the research:

- Dr. Andrew Dickerson for advising the project, for his abstract viewpoints, and unyielding desire to graduate his students.
- Dr. Ranajay Ghosh and Hossein Ebrahimi for assisting with the solid mechanics in explaining citrus jetting and expert work in FE simulations of peel bending.
- Daren Watson for late night conversation in lab to help keep sanity.
- Erfanul Alam for his peaceful company during tea breaks.
- Dr. Biswas for his assistance in fabricating mosquito inebriation chambers.
- Dr. Kauffman for lending the vibrational unit for the mosquito landing chamber experiments.
- Alexander Olvera for his continued assistance in research.
- Alexis Khalil for CADing flight chamber concepts which were later 3D printed and utilized continually.
- Alexander D'angelo for intense intellectual thought and conjecture in design of flight chambers.
- Grace Clayton for her expert glass-work and dedicated prototyping of insect treadmills.
- Jasmine Balsalobre for her assistance in interpreting and communicating the tendencies of mosquitoes in landing.

- All the other highschool and undrgraduates who I encountered on this journey, all your time spent assisting was truly appreciated and could not be summed in its entirety within the confines of this manuscript.

TABLE OF CONTENTS

LIST OF FIGURES

LIST OF TABLES

CHAPTER 1: INTRODUCTION

1.1 Motivation

Complex organismal behaviors have influenced engineers for centuries. Their highly coordinated kinematics, robust forms, and functions across both time and size scales require analysis. The motivation of this dissertation is both theoretical and experimental, to determine for two species, one active and another passive, classical engineering analogs that describe behaviors. We choose a plant, citrus fruit, and an animal, mosquitoes, to detail behaviors that are both under 50 ms and on the scale of 10 μm$-$10 mm. These time and size scales push the boundary of high-speed videography requiring new filming and experimental techniques.

We begin our focus with the largest scale, the behavior of *Aedes (Ae.) aegypti* mosquitoes in takeoff and landing phases. Their characterization allows for fabrication of bioinspired mechanical designs, an emergent field in the twenty-first century [4, 5]. Foreseen applications are small unmanned aerial systems (sUAS), whose utility range from swarming surveillance [6, 7] to reconnaissance and exploration [8, 9]. While much has been gained in knowledge of how insects fly [10, 11, 12], gauge distances [13, 14], and aggregate cohesively [15]; there is much more to be understood about kinematics of takeoffs and landings on the millimetric scale. The understanding of mechanics behind the interaction between mosquito and substrate may serve engineering as biological inspiration for improving robustness of miniaturized unmanned technologies.

Decreasing in scale we detail the microjetting of citrus reservoirs under compression. An area where engineering developed emergent and global technologies such as inkjet printing [16], drug delivery [17] and microfabrication [18]. These engineered microjets require electronic controls, pumps, and precision nozzles which carry high cost due to complexity and machining. Meanwhile,

fruits have been documented to produce high-speed microjets due to intrinsic biomechanics. Biological jetting is seen in organisms for a multitude of purposes, such as locomotion [19], defense [20], and seed dispersal [21]. The microjetting of citrus fruits is unique in that its' fluid acceleration magnitude is unrivaled in the plant kingdom, produced by an exploitation of contrasting elastic moduli and a flexible membrane. Characterization of the biomechanics producing the high-speed microjets may allow for the adaptation to the biomedical industry with fine tuning of the jet properties [22].

1.2 Background

We start with the background for each subject covered in this thesis; insect takeoffs, landings, citrus microjets, and aggregate motion.

1.2.1 Mosquito Takeoffs

Insect flight encompasses numerous kinematics for a plethora of procedures across species, yet in order to fly all insects are required to perform takeoff and landing operations. The Traditional studies of insect takeoff kinematics have focused on insect morphology [23, 24, 25, 26, 27] and takeoff stimulus [28, 29] without consideration of the role of surface conditions on takeoff mechanics. In nature, insects launch from a vast variety of surfaces offering variation in roughness and surface obstacles with which legs and wings must contend. As technology allows for the miniaturization of robotic flyers, predicted to resolve many surveillance, reconnaissance, and exploratory challenges [7, 30], takeoff conditions and takeoff surface topography pose a greater impact on flyer performance. Small insects provide kinematic templates for successful launching from a vast array of surfaces.

Insect takeoff is both scenario and species dependent. Furthermore insect takeoff may be further delineated into two categories, jumping and non-jumping, where one utilizes leg contributions and the other relies predominantly on wing flapping lift. Mosquitoes are known [28] to employ a two-step takeoff that is initiated with the legs prior to wing engagement, a shared behavior across scale and species. Locust takeoffs are described by a 'jump' prior to the first wingbeat, lasting 33 ms, whereby leg and wing actions are not overlapping [27]. In contrast, droneflies utilize wing and leg thrust in synchrony, gradually increasing stroke amplitude, beginning 10 ms after takeoff initiation, whilst monotonically decreasing leg output force through the twelfth wingbeat [24], exchanging speed for a relatively smooth takeoff, leaving the ground in 40 ms. Other insects choose speed over stability when startled [31], as common fruit flies perform two distinct takeoff strategies, one voluntary and the other responsive [29].

Mosquitoes often require their flight operations be clandestine to avoid detection by large hosts, thereby placing restrictions on forces transmitted to the takeoff surface. The threshold of mechanosensory detection of forces by the nerves surrounding human hair is 70μN [32], which is widely accepted to be the lightest detectable touch. In response, mosquitos have adapted 'light-footed' takeoff sequencing, which varies with weight as they feed [28]. A blood-fed *Anopheles coluzzi* mosquito weighs approximately $3\times$ its unfed bodyweight and adjusts its takeoff by utilizing more wing-based lift and correspondingly slow extension of legs, resulting in a maximum surface reaction force of 0.02 mN over a total takeoff time [28] of 26.3 ms.

Despite the extensive documentation of insect takeoff and external influences, missing from literature is a study that incorporates the affect of surface characteristics on the adaptive takeoff sequence of flyers with multiphase takeoffs, such as mosquitoes. We compare the takeoffs of *Ae. aegypti* mosquitoes, vector of the Zika and yellow fever viruses [33], from a surface the smoothness of glass to a surface the roughness of human skin. Documenting two distinct sequences of takeoff varied by surface roughness, both of the jump then flap behavior. The modification of leg

dynamics is akin to shifting from a 4-leg evenly distributed push to a striking leg followed by 4-leg push. We model the striking leg as a rigid cantilever beam striking the surface to generate upward momentum prior to synchronous leg engagement. Whereby the upward momentum reduces the contact time of the push phase and saves the energetic expense of slipping.

1.2.2 Mosquito Landings

Landings are unique from other flight maneuvers because they require matching the relative motion of a target, which calls for highly-coordinated movements in response to visual, thermal, acoustic, and olfactory signals [34, 13, 35, 36, 37, 38]. Landings are initiated to intercept prey, forage from dynamic surfaces, and perch [39, 14]. Frequent feeding requires flying insects to engage dynamic targets, from flowers swaying in a breeze to mammals in motion, and the mosquito provides an example of an animal which engages both animate and inanimate nutrition sources. Mosquitoes are notorious for covertly feasting on blood, a process which begins with landing and is accomplished across a range of relative velocities and surface orientations. *Aedes (Ae.) aegypti* mosquitoes are among the most prolific and dangerous mosquito species globally [40, 41], and like all mosquitoes, rely on an albuminous diet for maturation of the ova [33, 42]. Remaining undetected by the host during landing, feeding, and takeoff maximizes the probability of a successful meal. Despite their relevance to society, passive and active mechanisms by which mosquitoes initialize this process are understudied. The study of aerial landings across a variety of physiology, and under a plethora of environmental pressures, is not only imperative to understanding biological mechanisms, but may also be extended to the adaptation and survivability of small unmanned aerial systems (UAS).

A common method of smoothly engaging a landing surface by vertebrates is monitoring flight speed and distance to collision simultaneously, while incrementally decelerating as the substrate approaches, requiring binocular stereopsis for computing depth to target [43, 44, 45]. Many aves

glide downward with a lowered tail and rectrices spread fanwise, inducing a deep stall which allows them to drop onto their perch [46, 47], while exhibiting a variety of descent techniques. Pigeons (*Columba livia*) either descend slowly with upward-sloped wings or rapidly by orienting their bodies downward before engaging a stall maneuver in the final moments of flight [46, 48]. By contrast, the vampire bat (*Desmodus rotundus*), which feeds on the ground, initiates landing by entering a quasi-hovering phase above the ground, then lowers forelimbs until their digits make terrestrial contact and when landing in an arboreal perch, bats' legs act as a fulcrum allowing for downward body rotation [46, 49].

The landing strategies of invertebrates differ from those of vertebrates in both timescale, distance, and speed due to highly contrasting anatomy and function. Insects' immobile eyes and fixed focus optics prevent binocular stereopsis to gauge the distance from a substrate outright [43, 50, 51]. Insects instead use image motion to determine substrate distance. They monitor object expansion relative to their own motion, and control flight based on the rate of change of perceived object size [13, 14]. Honeybees (*Apis mellifera*) decelerate to a hover 16 mm from a landing surface, demonstrating that touchdown is indeed modulated through relative distance [14, 52]. Similarly, hawk-moths (*Macroglossum stellatarum*) decelerate upon approaching a flower and hover before initiating touchdown [53]. A female housefly (*Musca domestica L.*) approaches a landing surface at a constant velocity until the object reaches a critical size on its retina to induce deceleration [13]. In contrast, fruit flies (*Drosophila melanogaster*) accelerate towards their landing surface and, upon touchdown, use leg forces to undergo nearly instant deceleration [54].

Detailed *Ae. aegypti* landing mechanics are absent from literature, to the authors' knowledge, but are likely unique from other insects due to diet, wing mechanics [11], physiological proportions, and mass. A mosquito has $1\% - 10\%$ the mass of a housefly, honeybee, and hawkmoth [55, 14]. Their relatively low mass allows for survival of collisions with objects of much larger mass traveling at greater speeds [56], but the influence of mass on landing has not been studied. Typical

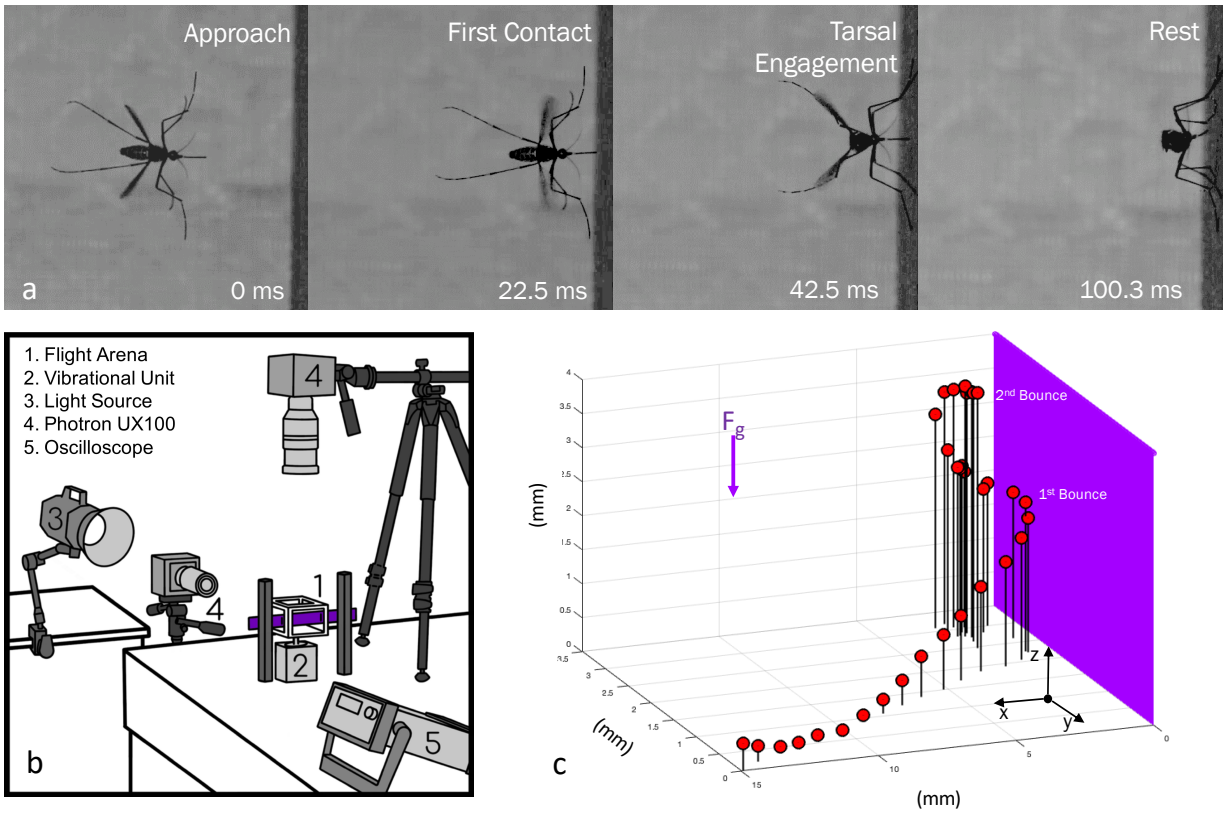

Figure 1.1: **(a)** Photographic landing sequence viewed from above. **(b)** Experimental setup of flight arena and orthogonally-positioned high-speed video cameras. **(c)** Three-dimensional displacement plot of a mosquito landing with 2.5 ms between each position marker.

mosquito flight posture is characterized by fore, mid, and hind-legs raised and splayed, perhaps for the sake of streamlining [33]. The sub-topic of mosquito landing which has received the most attention is their attraction to scents [57], patterns [58, 59], colors [60], and illumination [61].

We observe mosquito landings with high-speed cameras, seen in Fig.1.1, and digitize their motion to quantify landing forces, the employment of various appendages, and the ability of mosquitoes to cleave to surfaces across a range of relative velocities. We document the bounce strategy of mosquito landings, modeling the first touch to rebound as a mass-spring-damper system. The proboscis is modeled as a low stiffness cantilever beam that buckles under the load of landing. Landing mosquitoes behave as an underdamped mass-spring-damper, extending the duration of impact in

order to reduce force imparted to the substrate beneath the subcutaneous detection threshold [32].

1.2.3 Microjets of Citrus Reservoirs

Engineering provides fruitful analogs outside the class insecta and into the plant kingdom as we extend into the genus of Citrus fruit and their microjetting properties. Liquid microjets have long been of interest to the engineering community. While studies of synthetic microjet production and use abound, few studies have considered microjets in nature, which may provide alternative methods for robust jet production through the clever choice of material and geometry, and without cumbersome supporting systems. Examples of microjets in nature include spitting termites of the subfamily *Nasutitermitinae* that spit a viscous salivary toxin in defense of invertebrate attackers [62, 63], and spitting spiders, *Scytodes thoracica*, emit venomous silk from vibrating fangs to snare prey [64]. Outside the realm of arthropods, jetting in nature is commonplace and includes urination in mammals [65], spitting of venomous snakes [66], and squirting cucumbers [21], but these examples do not approach the microscale.

It is believed all fruits in the citrus family have been developed by cross-breeding three core fruits in the last 1000 years: the mandarin orange, pummelo, and citron [67]. All citrus fruits tested exhibited oil jetting behavior, but despite this shared characteristic, there remains no determinate evolutionary function of the oil, and no mention of oil atomization in the literature to the authors' knowledge. The volatile oils may be an attractant to pollinators [68], but are toxic to many arthropods [69, 70, 71]. Citrus oils are known to be phytotoxic [72] and anti-microbial [73], and so potentially able to protect the fruit and seeds from infection and select predation. Citrus fruits experiencing blunt impact often suffer internal reservoir rupture leading to spoiled fruit as adjacent cells burst in contact with oil [74]. Commercially, citrus oils are extracted for their aroma [75], flavoring food [76], and cleaning products [77].

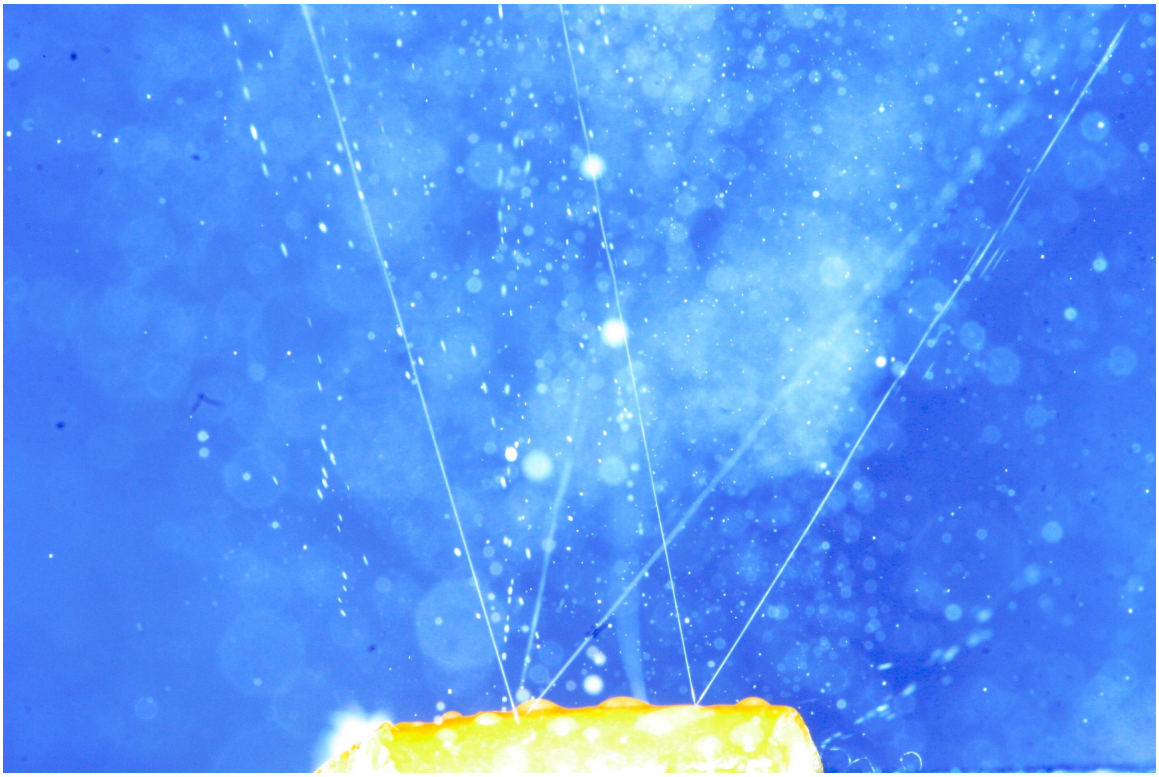

Figure 1.2: Image of oil jets issuing from sub-surface oil glands in the highly bent peel of a navel orange. The highly unstable jets issue at velocities that produce motion blur in the photo, giving the appearance of jet stability over longer distances.

We observe the oil reservoir in response to external bending deformation, may rupture the outer surface of citrus exocarp, producing high-speed microjets, by an exhaustive emptying of the fruit's aromatic volatile oil, as seen in Figure 1.2. These free jets are best witnessed after a fruit is peeled and by bending the peel such that the flavedo, or rind, faces outward (Figure 1.2, Figure 1.3**a**). Oil reservoirs reside in the mesocarp, or albedo, a compressible foam-like layer commonly known as the 'pith' that fills the space between the fruit locules and the thinner, stiffer flavedo [78]. The flavedo caps the reservoirs and shields the fruit from the environment. Gland placement within the peel and relative size can be seen in Figure 1.3**b,c**. The spaces between glands house stomata, the fruits' gas exchange pores [79] that measure approximately 20 μm in diameter. A layer of glossy boundary cells separates the oil in the reservoirs from the absorbent albedo [80], and is clearly

seen in Figure 1.3**b**, where the window into the reservoir is a fortuitous result of cutting. Ruptured reservoirs result from pressurizing the oil through externally applied forces. When its failure stress is reached, the flavedo cracks, allowing the pressurized oil to escape and the albedo to expand into the vacated space, deforming the reservoir, as seen in Figure 1.3**d**.

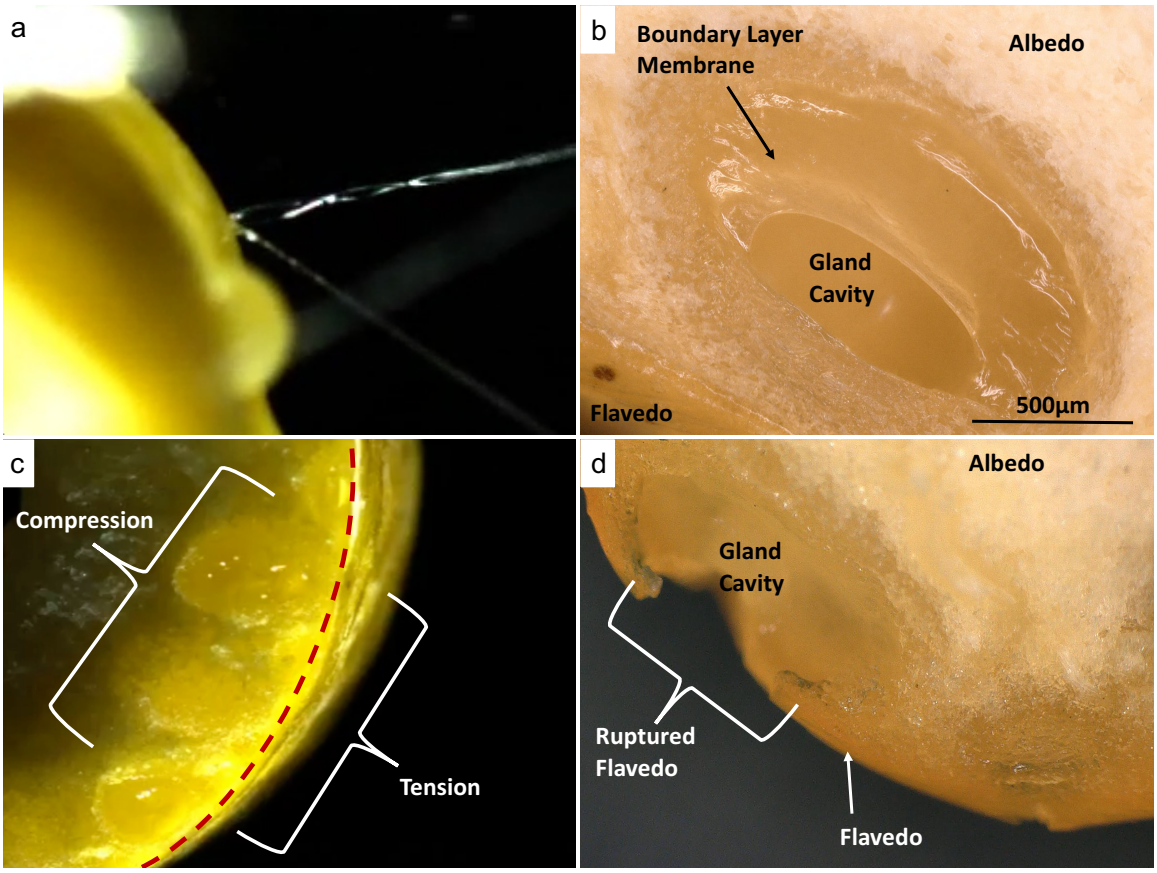

Figure 1.3: Microscopic images of **(a)** oil ejection from oil gland reservoir through the flavedo, **(b)** a cross-sectional view of a singular oil gland with boundary layer membrane partially intact, **(c)** a group of unbroken oil glands subjected to external bending, and **(d)** a cross-sectional view of an oil gland after rupture. The gland in (d) appears slightly collapsed due to ingress of the albedo toward the flavedo during rupture.

We hypothesize citrus fruit jetting is made possible by the composite peel structure housing the oil reservoirs, namely a soft reservoir boundary capped by a stiffer film. To test this hypothesis, we purchase, peel, squeeze, and film the jetting of oil from five *Citrus* (*C*) species readily available in most markets (Movie S1). These species, listed in Table 5.1, have a range of sizes and show

large variability in bulk fruit and reservoir volume within a species. We find no dependence of reservoir volume with fruit volume (Fig. C.4). Although comparative experiments are performed, we focus much of our effort on one fruit, the Florida navel orange, *C. sinensis*. We buy cold-pressed, commercially available orange oil for rheological measurement, and find it has a density $\rho = 0.823 \pm .010$ g/mL (N=10), dynamic viscosity $\mu = 0.96 \pm 0.02$ cP (N=12), and surface tension $\gamma = 29.4 \pm 0.3$ dynes/cm (N=5).

1.3 Thesis Outline

In this thesis we investigate the behavioral mechanics of citrus fruit and *Ae. aegypti* mosquitoes to develop analogs to classical engineering systems. We select our engineering analogs as ellipsoidal pressure vessels, mass-spring-damper systems, and cantilever beams in expressing the events of mircojetting, landing kinematics, and leg-strikes in takeoff. We develop novel experimental techniques to discover the biomechanics by which our chosen species engage their environment. This dissertation is primarily derived from recent publications and submissions [81, 82, 15]. Chapter 2 details the experimental procedure and setup for each subsequent chapter, as techniques are reused and modified for following research topics.

In Chapter 3 we begin the mosquito to substrate interaction analysis by filming the takeoff sequence of *Ae. aegypti* mosquitoes on substrates of contrasting surface roughness, from roughness of human skin to glass. Mosquito takeoff strategies have two distinct kinematics, a traditional quadrupedal push with subsequent wing engagement and a modified push where upward momentum is generated by a leg-strike before quadrupedal push is engaged. These strategies were dependent upon surface roughness with reduction in substrate contact time through a leg-strike. We rationalize the modified behavior as a means of building momentum through swinging a non-contacting leg, modeled as a cantilever beam, in order to reduce the energy expenditure of slipping on the substrate.

In Chapter 4 we present experimental results for behavior of mosquitoes throughout the landing phase of flight, complimentary to Chapter 3 in understanding all phases of insect to substrate interactions outside the blood-meal. We model the behavior as an underdamped mass-spring-damper system where the mosquito clings throughout the residual undulation. We notice a buckling under landing load of the proboscis which agrees with the forces imparted in the initial contact of our model system. We predict landing velocities for mosquitoes to remain clandestine in human interaction, matching the majority of experimental landing velocities recorded, explaining the well documented human experience of not feeling a mosquito until after a blood-meal has ceased.

In Chapter 5 we examine our second species, citrus fruit, and their capabilities of microjetting. Through high-speed videography and imaging we characterize the biomechanics behind the jetting of oil reservoirs within the rind of citrus fruit. We detail the jet kinematics by modeling the jet as a collection of spherical oil droplets moving throughout space and solve for the velocity decay for subcritical Reynolds numbers. Using an ellipsoidal pressure vessel model we then calculate the bursting pressure through two means, hoop stress and fluid kinematics, which agree with a simulation of an ellipsoidal pressure vessel housed within a ductile membrane capped by a stiff outer membrane. Noting the stomata acting as a perforated edge surrounding the capped end we detail the rupture stress to be governed by Griffith's crack criteria matching the scaling of jetting velocity to elastic modulus. In Chapter 6 we conclude by discussing the implication of our work along with suggesting future avenues of research.

CHAPTER 2: METHODOLOGY

The experimental methodologies for research topic in this dissertation, insect takeoff, landings, and flight through insecticides.

2.1 Mosquito Takeoffs

We being by defining the research methodologies employed in the mosquito takeoff experiments.

2.1.1 Takeoff experiments

Takeoffs were filmed using Photron AX-100 and UX-100 high-speed cameras at 1000-4000 fps and 1/8000 shutter. The glass mosquito flight arena is shown in Figure 2.1 and measures $76 \times 79 \times 152$ mm. A 7.5 mm ID glass tube is inserted 100 mm above the arena floor through which mosquitoes walk to enter the the arena, emerging on a horizontal takeoff platform measuring 21 mm^2.

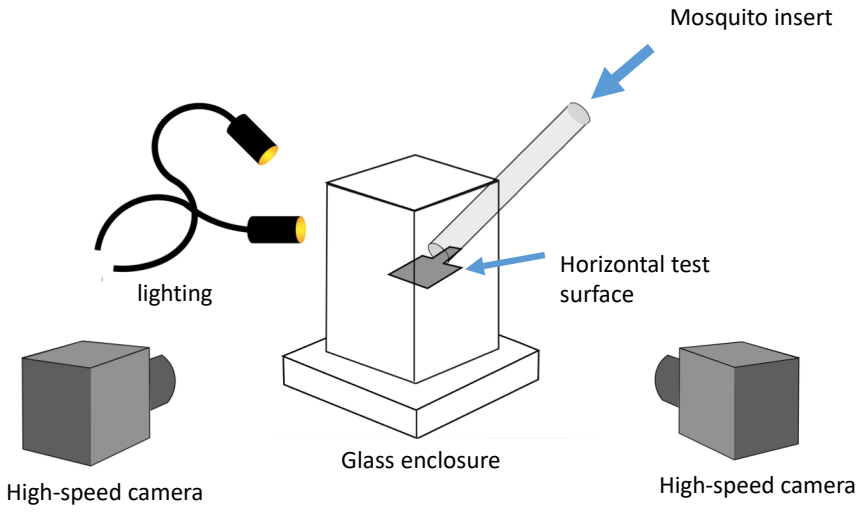

Figure 2.1: Image of mosquito flight arena experimental setup.

Mosquitoes are transported with an aspirator to a larger diameter holding area at end of the tube (not pictured), allowing mosquitoes to exit toward the arena under their own volition. The tube dwell times ranged from 1-15 min. Mosquitoes preferred to exit the holding area when the capacity exceeded 15 mosquitoes. No anesthesia was used prior to takeoff experiments. Following experiments, mosquitoes were anesthetized with carbon dioxide for removal from the flight arena. Individuals were euthanized following trials to avoid pseudoreplication.

2.1.2 Surface characterization

Surface A is an unmodified, polished acrylic sheet. Surface B is made by roughening polished acrylic with a 12.7-cm (5-inch) orbital hand sander using 220 grit sandpaper. Surface roughnesses is measured using a KLA-Tencor Alpha-Step 500 profilometer in two dimensions to ensure surface homogeneity. Scanning electron microscope (SEM) images were garnered with a Phenom G1 desktop SEM.

2.1.3 Mosquito mass measurements

Mass measurements were performed using a Sartorius Secrua 225D-1s microbalance using 20 anesthetized and fully-intact mosquitoes. Simultaneous mass measurement of 20 mosquitoes reduces the influence of instrument error. Leg mass is done by gender in a similar manner by anesthetizing a group of mosquitoes and extracting 20 rearmost legs, those used for the leg-strike takeoffs. The center of mass of the leg was determined digitally using imageJ and by assuming the density of leg tissue is uniform throughout. A binary image used to estimate a leg's center of mass and produced from Figure 3.1**b** is provided in Fig. S1.

2.2 Mosquito Landings

2.2.1 Landing experiments

The landings of non-blood fed female *Ae. aegypti* mosquitoes are filmed within a plastic 3D-printed flight arena affixed with acrylic walls. The arena measures 70 x 100 x 140 mm, as seen in Figure 1.1**b**. A purple substrate equal to the container width and 40 mm in height is placed at one end of the arena as a landing platform; darker hues elicit landings at a rate 9x higher than clear or white substrates [61]. Mosquitoes are anesthetized with CO_2 for placement into the flight arena, and given sufficient time to recover from anesthetization before filming. A landing substrate is suspended in the container and supported by external pillars. To encourage resting mosquitoes into flight, the arena is vibrated at 25 Hz for up to 5 seconds. After cessation of vibration, only landings that originate from an orthogonal distance greater than 10 mm is saved for analysis.

Landings are filmed using Photron AX-100 and UX-100 high-speed cameras at 2000-4000 fps in single and dual camera configurations to extract kinematic measurements. In single camera experiments, we view landings from above and measure the position and velocity in a horizontal plane orthogonal to the landing substrate. Two cameras are utilized for 3D reconstruction, where an additional camera is placed to view the landing surface in its entirety. 3D trajectories are extracted from paired videos DLTdv7 in MATLAB [83]. The classic Euler angles of the mosquito is captured using three coplanar points, reconstructed using Horn's method to determine the yaw, pitch and roll of the mosquito throughout it's flight.

2.2.2 Proboscis characterization

The proboscis is modeled as an end-loaded cantilever beam. The proboscis is excised from the head and affixed to a rigid rod with UV-curable glue. A Keyence VHX-900 digital microscope is

used to measure its diameter and cantilevered length at a magnification of 150x, and when set to record at 30 fps, films the accumulation of a water droplet produced by an ultrasonic humidifier. The subsequent deflection of the proboscis under the weight of the droplet is measured in Tracker.

2.2.3 Leg damping analysis

Damping characteristics are determined by using a modified cubic flight arena of characteristic length $a = 37.5$ mm to inhibit free flight and ground the mosquitoes. The mosquitoes are vibrated at a fixed frequency of 25 Hz for a few seconds to establish sinusoidal behavior, and then vibration is ceased. Videos are analyzed with Tracker.

2.3 Citrus Microjetting

2.3.1 High-speed image analysis and microscopy

All *Citrus* fruits used in experiments were obtained from local groceries. Once peeled, specimens were used within 15 minutes to preserve material properties. Oil jets were filmed with Photron Mini UX100 and AX100 cameras at 4,000 - 16,000 fps, depending on the scale and phenomenon of interest. Jets were initiated by placing peels between stationary pliers. Jet velocity, diameter, and breakup distance were measured digitally using Open Source Physics Tracker software. Pores from which jets issue were imaged pre- and post-jetting with a Keyence VHX-900 digital microscope with built-in area and dimension measurement capability.

2.3.2 *Material property measurements*

Tensile testing is performed with a MTS Tytron 250, using a 50 N load cell, and pulled at a rate of 0.3 mm/s. We prepare tensile test samples by mechanically separating flavedo and albedo with a sharp blade immediately after peeling. Samples of flavedo and albedo are cut into a rectangular sections 12 mm (polar) x 25 mm (equitorial). Flavedo samples to measure strain energy release rate G_c are cut into rectangular sections 25 mm (polar) x 50 mm (equitorial), and given a $8-15$ mm manufactured flaw in the form of a thin cut orthogonal to the direction of applied loading. Such flaws lie within $30-60\%$ the width of the sample.

2.3.3 *Finite element simulations*

To simulate the bending of a citrus peel and measure the pressure field surrounding an oil reservoir, we perform an analysis with ABAQUS (Dassault Systèmes) general static step, using a RVE with rotational boundary conditions at the side walls. To avoid rigid body motion, we fix one node of this unit cell on the middle symmetric plane and mesh with quadratic tetrahedron elements (C3D10) around reservoir geometry and quadratic hexagonal elements (C3D20) in other regions. A linear elastic material model was used for all simulations and gland fluid was modeled as incompressible.

2.3.4 *Oil gland reservoir and fruit volume measurements*

We image orange peel cross sections with a Nikon D850 SLR camera and digitally trace the outer boundaries of gland reservoirs in images. We assume reservoirs are symmetric about the jetting axis and use MATLAB to perform shell integration volume calculations for the coordinates of reservoir boundaries captured in photos. Whole fruits volume measurements were taken by recording the fluid displaced during complete submersion.

CHAPTER 3: MOSQUITOES MODULATE LEG DYNAMICS AT TAKEOFF TO ACCOMADATE SURFACE ROUGHNESS

In this combined theoretical and experimental study, we investigate the takeoffs, as seen in Figure 3.1**a**, of *Ae. aegypti* mosquitoes from surfaces of contrasting roughness. In §3.1, we present the two observed takeoff kinematics, a push and a modified push dubbed a 'leg-strike'. We present a 2D model for the kinematics associated with a leg-strike takeoff and determine the associated substrate forces for both strategies. We rationalize takeoff techniques by comparing surface features with those found on the mosquito tarsi, and discuss the implications of our study and avenues for future research in §3.2. We provide a summary from our work in §3.3.

3.1 Results

We film 106 horizontal takeoffs of non-blood fed, male and female, *Ae. aegypti* mosquitoes at 1000-4000 fps in a custom flight arena in which mosquitoes emerge from a tube onto a platform of varying surface roughness (see §2.1.1). Restriction of the tube diameter prevents flight inception within the tube, mandating mosquitoes launch from the horizontal platform. Using this method, no anesthetization was used to place mosquitoes onto the takeoff platform. Under voluntary takeoff conditions, we observe *Ae. aegypti* mosquitoes employ two distinct takeoff strategies. The first, dubbed a 'push', is described by the quick extension of legs to their maximum extent. Most commonly, all six legs participate in pushing but we occasionally observe a 4- or 5-legged push. Legs consist of three sections, the femur, tibia, and tarsus, as shown in Figure 3.1**b**. During takeoff, only the tarsi contact the ground. As the mosquito body moves upward, the tarsi slide inward, frequently meeting before lifting off. The second strategy, a 'leg-strike', is initiated by the downward swing of one elevated hind leg. The transfer of momentum from the subsequent strike against the

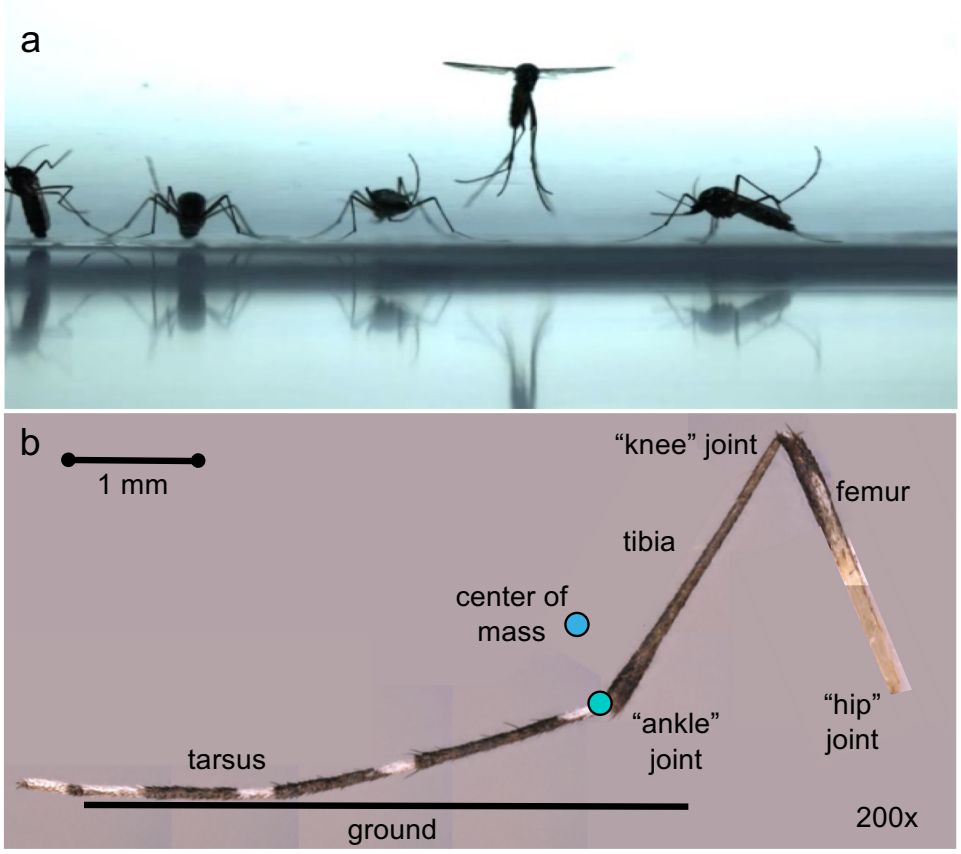

Figure 3.1: Image of **(a)** multiple mosquitoes sitting at base platform with one mid-action takeoff and **(b)** a composite image of a mosquito's striking leg at 200x.

substrate initiates body lift. Following the leg-strike, a six-legged push commences, comparable to a purely pushing takeoff. Below we compare the performance and substrate forces for both takeoff types.

3.1.1 Pushes

Mosquitoes begin a pushing takeoff with their legs planted on the takeoff platform. In unison, the legs straighten and draw inward, pushing the mosquito's body upward as wingbeats commences. This sequence of leg extension and body lift is displayed pictorially in Figure 3.2 and shown in Movie S1. In the following calculations of force and power, we consider only the dynamics of

female mosquitoes. The legs experience rapid extension during pushing, beginning with a contracted angle of $88.5 \pm 16.9°$, N=5, and extending to $120.2 \pm 20.5°$, N=5, over the course of time preceding the first wingbeat $\tau_w = 5.5 \pm 2.2$ ms, N=10, and corresponding to the leftmost region of Figure 3.2. The resulting angular velocity, 16 rev/s, is sufficient to produce a lift velocity of $U = 0.38 \pm 0.17$ m/s, N=10, generating an upward acceleration equivalent to 7 gravities (g).

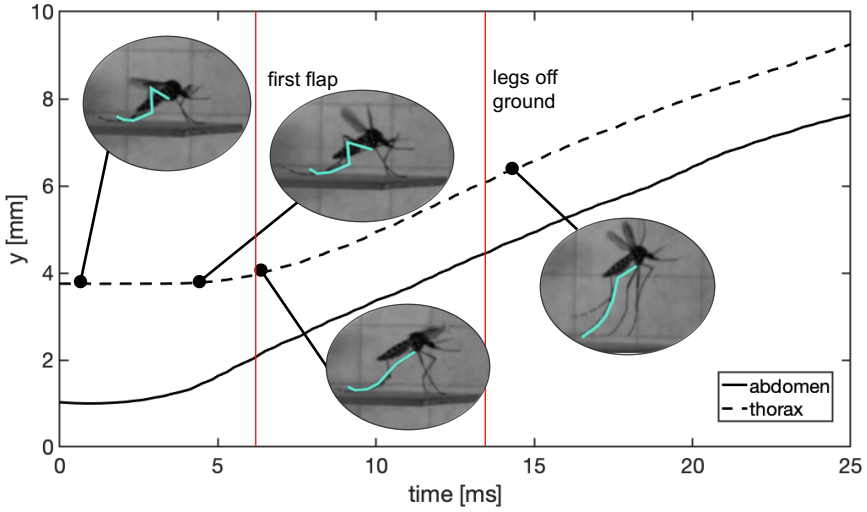

Figure 3.2: Steps defined for a push takeoff overlaid onto an elevation vs. time plot for abdomen and thorax positions

We assume that each leg contributes equally to liftoff in our analysis. We likewise assume that pushing forces are greatest before wingbeats begin, since the aerodynamic lift force created by the wings is $\sim 1-5$ times greater than that of the legs [28], and so we only consider the short moments prior to the first full wingbeat τ_w in our analysis of applied substrate forces. The total time to tarsal liftoff $\tau_{lift} = 11.6 \pm 1.6$ ms, N=10. Finally, we assume the force provided by the legs remains constant throughout τ_w and that tarsi do not slip outwardly, as done in previous studies [84, 85, 86, 87]. We discuss the implications of this assumption and provide an alternative in §3.2. Conservation of momentum and impulse yields

$$F_P = \frac{m}{6}\left(\frac{U}{\tau_w} + g\right), \tag{3.1}$$

where $F_P = 0.027$ mN is the normal pushing force per leg exerted on the takeoff platform, $m = 2.06$ mg is the mosquito's body mass, averaged over 30 individual females, and $g = 9.81$ m/s^2 is the acceleration due to gravity. We note this value is well below the cutaneous neuron mechanosensory threshold of human hair [32], 0.07 mN, but greater than those previously measured for *Anopheles coluzzi* [28]. The average power generated by a pushing leg during takeoff is given by

$$P_P = \frac{mU}{6}\left(\frac{U}{2\tau_w} + g\right), \tag{3.2}$$

where $P_P = 5.78\ \mu$W.

3.1.2 Leg-strikes

Leg-strike takeoffs are modifications to pushing takeoffs, and are of similar duration to purely pushing takeoffs at $\tau_w = 9.6 \pm 1.6$ ms, N=10, and $\tau_{lift} = 13.1 \pm 2.3$, N=10. Achieving nearly identical vertical body velocity at first wingbeat, $U = 0.35 \pm 0.17$ m/s, N=10. The takeoff begins as an elevated rear leg swings rapidly downward and strikes the takeoff substrate at $U_{leg} = 0.59 \pm 0.06$ m/s, N=25, measured by tracking the 'ankle joint' of the leg as denoted in Figure 3.1**b**. The tracked position on the leg is a surrogate for the leg's center of mass, which is nearby and likewise denoted in Figure 3.1**b**. The downward swing of the leg is pictured in Figure 3.3 and shown in Movie S2. Through video analysis at 10,000 fps we measure leg swing distance $d_s = 1.8 \pm 0.4$ mm, N=3, and impact time $\tau_i = 0.8 \pm 0.10$ ms, N=3. Following impact of the swing, all legs push upward, and generates a comparable ground reaction force. The force of the striking leg $F_{LS} = 0.025$ mN and is given by

$$F_{LS} = \frac{m_{leg} U_{leg}}{\tau_i}, \tag{3.3}$$

where the mass of the striking leg $m_{\text{leg}} = 33.5\ \mu\text{g}$. Like F_{P}, F_{LS} lies well below the mechanosensory threshold in humans [32], and thus a striking leg is imperceptible to a human host. The average power required to achieve U_{leg} is

$$P_{\text{LS}} = \frac{m_{\text{leg}} U_{\text{leg}}^2}{2\tau_{\text{s}}}, \tag{3.4}$$

where the swing time from first movement until first contact with the ground is represented as

$$\tau_{\text{s}} = \frac{d_{\text{s}}}{\chi U_{\text{leg}}}, \tag{3.5}$$

and experimentally measured $\chi = 0.71$ compensates for the ramp in leg speed up from zero to U_{leg}. The resulting power given to the single striking leg $P_{\text{LS}} = 1.36\ \mu\text{W}$ is considerably less than the power required of a pushing leg according to Equation 3.2, $P_{\text{P}} = 5.78\ \mu\text{W}$.

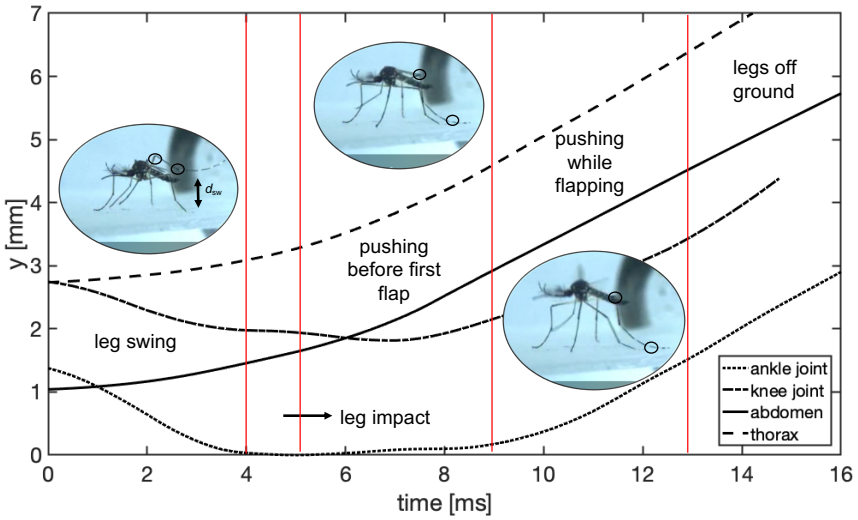

Figure 3.3: Steps defined for a leg-strike takeoff overlaid onto a elevation vs. time plot for abdomen, thorax, 'knee' and 'ankle' joint positions.

A leg's center of mass striking the ground at a perpendicular distance $\ell = 2.58 \pm 0.14$ mm from the

body's center of mass has consequences on body pitch and lift. If we estimate the center of mass to lie midway between the aft of the abdomen and the base of the proboscis, we may calculate the pitch of the body during the strike by first finding the angular acceleration $\alpha = (F_{\mathrm{LS}}/\bar{I})\ell = 18.7 \times 10^3$ rad/s^2 imparted to the body during the leg's impact time, for a cylindrical mosquito of length $L = 4.48 \pm 0.34$ mm. The mass moment of inertia for a cylinder rotating longitudinally about its center is $\bar{I} = mL^2/12$. The corresponding change in body angle during the ephemeral impact time τ_{i} is a minuscule 0.34°. Such as small rotation is not perceptible in tracking data. We calculate the impulsive force of the striking leg generates an upward body velocity fo 0.01 m/s, which is 3% the body velocity at first wingbeat. It may appear the leg-strike is a little consequence, but the result is unloaded tarsi at the onset of the pushing phase, which is likely to retard tarsal engagement of the surface when pushing commences, allowing for increased traction.

3.1.3 Surface roughness drives takeoff strategy

The two surfaces used in this study are pictured in Figure 3.4**a,b**, alongside an *Ae. aegypti* tarsus at the same scale. Surface A (Figure 3.4**a**) is polished acrylic, having an arithmetic mean deviation roughness $R_{\mathrm{q}} = 3.1$ nm, the approximate roughness of glass [88]. Surface B (Figure 3.4**b**) is acrylic roughened with sandpaper, and has $R_{\mathrm{q}} = 43$ μm, approximately the roughness of human skin [89]. The mosquito tarsus (Figure 3.4**c**) is covered in feathery scales which aid in standing on a water surface [90], roughly 10-15 μm in size according to our measurements.

Takeoff strategy is driven by surface roughness. As seen in Figure 3.4**d**, polished Surface A resulted in leg-strikes (66%) dominating pushes (34%), N=44, when considering both male and female mosquitoes. Surface B, the rougher of the two, evokes greater frequency of pushing (56%) and leg-strikes (44%) in minority, N=62. We find takeoffs from these two surfaces to be statistically different when performing a Fisher's exact test for contingency, with $p = 0.0301$. However,

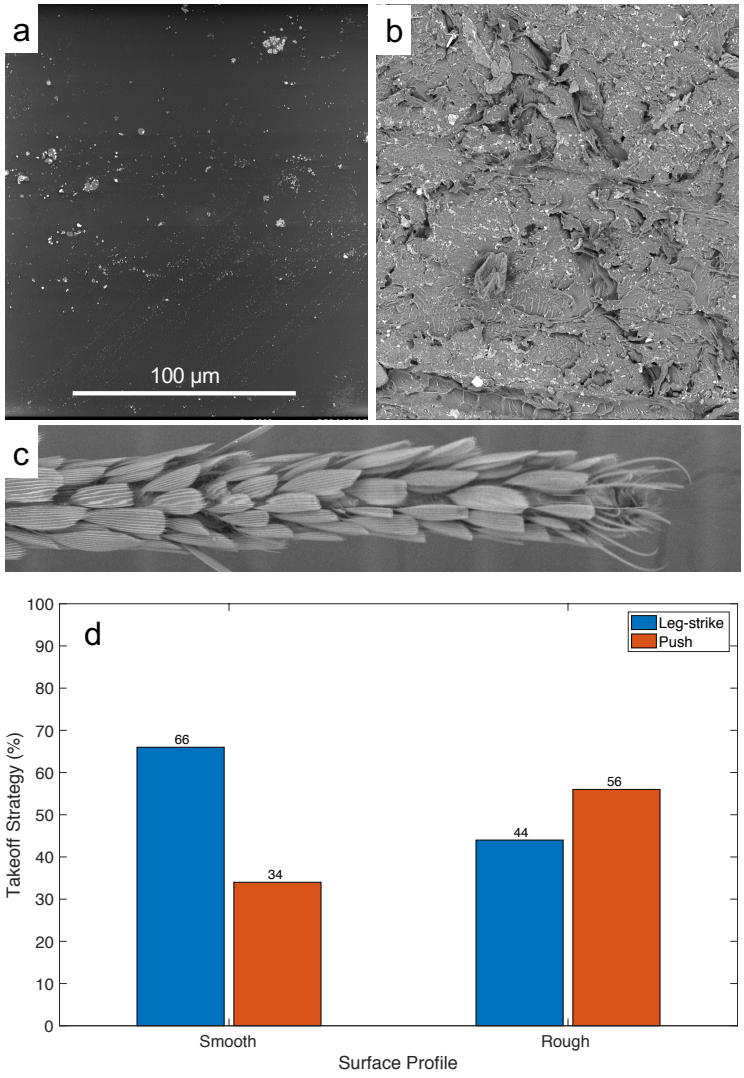

Figure 3.4: SEM images of **(a)** Surface A, polished acrylic, $R_a = 3$ nm, **(b)** Surface B, roughened acrylic ($R_a = 300$ μm), and **(c)** the *Ae. aegypti* tarsus. The bar plat in **(d)** shows takeoff preference by percentage of unfed *Ae. aegypti* from smooth (Surface A) and roughened (Surface B) takeoff platforms. Genders, combined for this plot, are not statistically different.

no such strategy preference exists based on gender for either surface Surface A ($p = 0.5350$) or Surface B ($p = 0.5792$).

We rationalize the shift in strategy preference by observations of purely pushing takeoff on polished and roughened surfaces. When pushing from roughened Surface B, mosquitoes tarsi remain in

place through the bulk of leg extension and draw inward as legs reach their maximum extent (Figure 3.2). The alignment of the feathery structures on the tarsi likely provide anisotropic friction and aid this maneuver. As seen in Figure 3.4**c**, the features on the tarsus match the scale of the disparities on Surface B, but are larger than the disparities of Surface A. In contrast to Surface B, pushing from Surface A may result in the outward slip of the tarsi (Movie S3), thereby reducing the efficacy of the push. Traction on Surface A is so little that we observe some mosquitoes rest their abdomen on the takeoff platform prior to takeoff due to the severe splaying of their legs.

3.1.4 Model for optimal leg-strike takeoff

Table 3.1: Takeoff measurements for push and leg-strike takeoffs (N=10).

	m_{leg}	m_{body}	U (m/s)	U_{L} (m/s)	τ_{bw} (ms)	τ_{t} (ms)
Push	33.1 µg	2.06 mg	0.38 ± 0.17		5.5 ± 2.2	11.6 ± 1.6
Legstrike			0.35 ± 0.17	0.59 ± 0.06	9.6 ± 1.6	13.1 ± 2.3

Mosquitoes may exercise a range of leg-striking speeds to initiate takeoff, as would any flyer employing this method of launch. However, choice of leg-striking speed will influence takeoff dynamics in both leg-strike and push phases of takeoff. A mosquito launching from a host should do so quickly with sufficient velocity to escape the surface and do so undetected. Therefore, we surmise mosquitoes instinctively keep total takeoff time consistent while minimizing force exerted on the host. We rationalize the observed leg impact speed U_{leg} by modeling each portion of takeoff, swing, impact, and push, while fixing time to first flap τ_{w}, takeoff speed U, leg swing distance d_{s}, and leg impact time τ_{i} to the average observed in experiments and provided in Table 3.1.

As a result of the leg striking the ground, the body is pushed upward at

$$U_0 = U_{\text{leg}} m_{\text{leg}}/m. \tag{3.6}$$

The time remaining for the pushing phase is $\tau_w - \tau_s - \tau_i$, over which the six pushing legs need to generate an additional upward body velocity of $U - U_0$. Combining Equations 3.1, 3.3, 3.5, and 3.6, we develop a model by which we can vary U_{leg} and generate F_{LS}, and the pushing force per leg in the portion of takeoff following leg impact,

$$F_{P,LS} = \frac{m}{6}\left(\frac{U - U_0}{\tau_w - \tau_s - \tau_i} + g\right) \tag{3.7}$$

The curves for F_{LS} and $F_{P,LS}$ are given in Figure 3.5**a** for a range of U_{leg} values. The upper bound of U_{leg} is set such that the striking leg does not exceed the mechanosensory threshold of 0.07 mN. Slower U_{leg} values require greater forces by the pushing legs. This model, however, will not predict the value of F_P given by Equation 3.1 as $U_{leg} \to 0$ because a very slow U_{leg} will require very large pushing forces for a takeoffs constrained to τ_w. Therefore, we must apply a lower bound $U_{leg,\,min} = g\tau_i(m/m_{leg}) = 0.49$ m/s, the minimum speed required to generate a force equal to the mosquito weight, 0.02 mN. Below $U_{leg,\,min}$ the striking leg cannot generate upward motion.

By choosing the intersection of the curves in Figure 3.5**a**, $U_{leg} = 0.64$ m/s and $F_{P,\,LS} = 0.027$ mN, a model mosquito minimizes the greatest force exerted on the host substrate, minimizing the chance of detection. We note the force-minimizing leg-strike velocity predicted by our model is very close to the observed average of 0.59 m/s.

The curves for power produced by a striking leg, P_{LS}, and pushing leg, P_P from Equations 3.2 & 3.4 respectively, are shown in Figure 3.5**b**. We note the intersection of these curves lies at $U_{leg} = 0.69$ m/s and 2.16 μW, less than half the pushing power of a leg in a purely push takeoff at 5.78 μW (§3.1.1). According to our model, at the observed leg-strike velocity of 0.59 m/s, the force and power of a pushing leg following the leg strike is 0.029 mN and 2.4 μW. We therefore conclude the choice of U_{leg} is driven by reaction forces and not leg power.

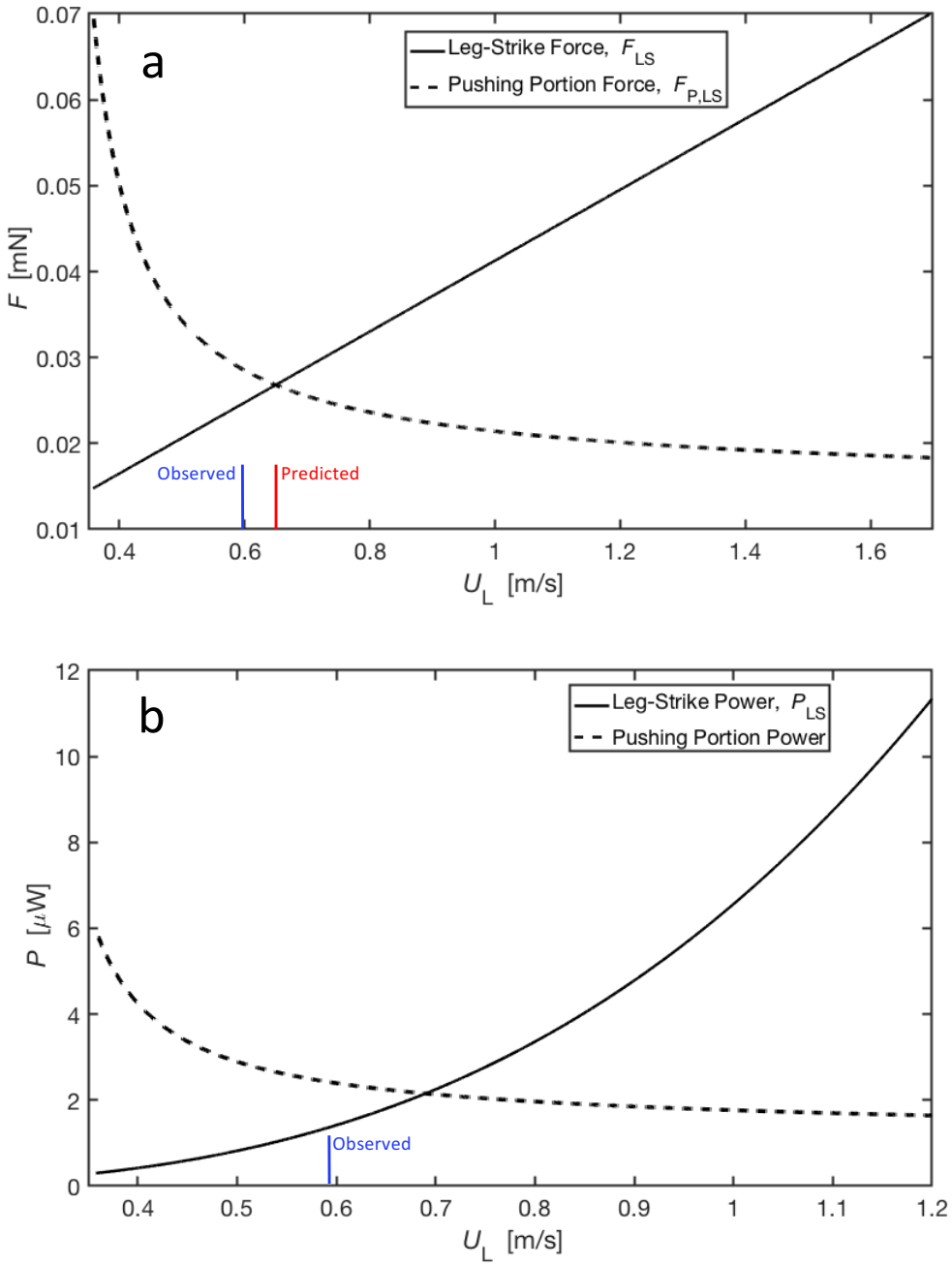

Figure 3.5: Model generated plots show the variance of leg-strike and pushing **(a)** forces and **(b)** power across a range of leg-strike impact velocity. The model predicted impact velocity based on force of 0.65 m/s is close to the observed average of 0.59 m/s

3.2 Discussion

Our study reveals that *Ae. aegypti* mosquitoes employ two distinct takeoff strategies, a push and a leg-strike, and each strategy's proportion of utilization is influenced by takeoff surface roughness. To combat tarsal slipping on smooth surfaces, a leg-strike provides an initial boost skyward, decreasing the effort required by the subsequent pushing phase. Leg-strikes also consume 75% more time to execute than a purely push-based takeoff, while still producing a nearly identical vertical velocity of ~ 0.35 m/s at the instant of first full wingbeat. The extra time is consumed by swinging a hind leg downward, producing a force comparable to the force of a pushing leg.

A greater understanding of the leg dynamics in launching mosquitoes may lead to enhanced functionality of sUAS and terrestrial robots alike. Robotic jumpers [91, 92, 93, 94, 95, 96, 97] utilize the ubiquitous biological strategy of jumping to locomote across challenging terrain [92, 96, 98], a strategy likely to be found in the next generation of extraterrestrial explorers [99, 100, 101, 102]. Jumping permits flyers to become airborne before engagement of in-flight thrust sources, while terrestrial jumpers gain the ability to navigate difficult terrain not suitable for more common wheel- and track-based travel. Challenges robotic jumpers must overcome include takeoff angle modulation, self-righting upon landing, sequential jumping, and steering. Certain robots, such as the 'sand flea' [103], are able to jump tens of feet. However, certain terrain stand to challenge robotic design, which results in the inability to achieve maximum height and steering [91]. In the case of a polished surface such as ice, the performance of jumpers may be compromised, but the utilization of a leg-strike type jump may subvert detrimental slippage. Such takeoffs allow biomimetic devices an enhanced ability to optimize launch behaviors for power and speed requirements when encountering a myriad of terrain features.

Determination of pushing force and power

For takeoffs which employ as few as four pushing legs, the figures for force and power presented

above must be recalculated. For purely pushing takeoffs, $F_P = 0.041$ mN. For leg-strike takeoffs, the pushing phase legs would exert $F_P = 0.043$ mN. We note these values remain well below 0.07 mN limit [32], which suggests the choice in number of participating legs is more critical for takeoff stability or direction than takeoff performance.

The assumption of constant F_P over the entire course of pushing motion provides an average value. If this assumption is violated, the average force value can be much less than the peak value. We may alternatively find F_P over the time course of takeoff by examining upward motion of the mosquito body and assuming the body is rigid and not rotating. Second order numerical differentiation of the thorax track in Figure 3.2 produces a temporal curve for F_P given in Fig. S2, corresponding to an upward body acceleration of 11.3 gravities (g). The peak force per leg is 0.038 mN, with an average of 0.030 mN over 5.2 ms. We note this peak force is less than 0.07 mN and not dramatically greater than the previously calculated $F_P = 0.027$ mN. If only four legs are engaged in pushing, the peak push force would be 0.058 mN per leg.

In comparison to fleas [104, 105] and leafhopper insects [85, 106], mosquitoes are not adept jumpers. Fleas (*Boreus hyemalis*) and leafhoppers (*Ulopa reticulata*) generate accelerations as high as 150 g and 235 g, respectively, by elastic recoil of a resilin spring within the thorax [104, 85]. In leafhopppers, the corresponding power per muscle mass for the hind leg extensors is 25 mW/mg, where muscle mass is taken to be 11% of the body mass [85]. At just 11.3 g and using all 6 legs, it is unlikely mosquitoes employ elastic energy release when pushing, but instead use direct muscle contraction as in flight [107]. The mass of the mosquito's extensor muscles is unknown to the authors, but if we conservatively assume the combined extensor muscle mass for all six legs is 5% of the body mass, the mosquito would have a power per muscle mass value of 0.34 mW/mg, which is comparable to the power density of the in-flight muscles of other insects [107].

Determination of leg-strike force

During leg impact, the leg converts its kinetic energy into body lift over a sub-millisecond impact time. Predictions of leg-strike velocity given by our impact model in §3.1.4 are sensitive to the magnitude of leg impact time. An increase in the impact time of 1 ms requires a doubling of the velocity of the striking leg. Fortunately for mosquitoes, this impact time is passively governed by the material properties of their leg segments and joints. Leg deformation upon impact sets the impact time. Mosquitoes possess tubular legs [33], enabling the legs to attain stiffnesses higher than solid legs of the same mass. Greater leg stiffness shortens impact times and according to Equation 3.3 enables more efficacious force transfer. Clever choice of leg materials and geometry in sUAS will enable optimal takeoff performance by controlling leg deformation.

Prediction of slipping losses

As tarsi slip on Surface A, a bit of takeoff energy from pushing legs is lost to friction during lateral motion. If we assume the mosquito generates the same force on Surfaces A and B, we may estimate the pre-leg energy lost to friction as $E_{\text{slip}} \approx d_{\text{slip}} F_{\text{P}} = 0.054\ \mu\text{J}$, where $d_{\text{slip}} = 0.6 \pm 0.4$ mm, N=5, is the distance of tarsal slip and F_{d} is estimated from Equation 3.1. The per-leg energy used during a slip-free takeoff can be estimated as $E_{\text{P}} = F_{\text{P}} \Delta z = 0.036\ \mu\text{J}$, where $\Delta z \approx 1$ mm is the change in height of the center of mass from a resting position to the first wingbeat. We note this approximation for pushing energy is in agreement with $\tau_{\text{w}} P_{\text{P}} = 0.025\ \mu\text{J}$ from Equation 3.2. Therefore the mosquito is poised to use $E_{\text{slip}} = (d_{\text{slip}}/\Delta z) E_{\text{P}} = 1.5 E_{\text{P}}$ for failure to choose the appropriate takeoff technique. Leg-strike takeoffs reduce the energy lost to slipping by positioning the legs closer to an orthogonal posture with the surface prior to the pushing phase of takeoff and subsequently reducing d_{slip} to < 1 mm.

Biological implications

As presented in §3.1.3, there is no statistical difference between female and male utilization of takeoff procedure, implying the disparity in weight between the genders does not greatly impact

takeoff preference. Furthermore, mosquitoes (*Anopheles coluzzi*) are able to modulate takeoff kinematics following a blood meal, in which their mass grows by 3×, to maintain their liftoff speed [28]. Blood-fed *Anopheles coluzzi*, weighing 80% more than the females we study, liftoff at 0.23 m/s. This suggests there may be an optimal vertical takeoff velocity envelope for insects at the scale of mosquitoes, or with similar wingbeat kinematics, but this remains an area for future research. If the *Ae. aegypti* used in this study were allowed to blood-feed, we likewise expect wings to assume a greater role in takeoff force generation and vertical velocities at first wingbeat to decrease.

While our study highlights the mechanics of leg-initiated takeoffs by mosquitoes, it does not answer why takeoffs begin with leg motion. We surmise that leg-initiated takeoffs performed by mosquitoes are not principally done for efficiency nor speed. Any energy savings gained by reducing the number of wingbeats, $O(10)$, performed is minute by comparison to the number of wingbeats performed over a single flight, $O(10^4)$. Wings, and membrane wings in particular, are known to have increased performance near the ground [108] due to vortex interaction with a solid surface. The unique wing stroke kinematics of mosquitoes [109] may induce instabilities near the ground, but this is undetermined at this time. Time savings from using legs are likely meager as well. The time of leg action prior to the first full wingbeat is less than 10 ms. If leg action were to achieve the same dynamical consequences of 5 wingbeats, a mosquito beating its wings at 608 ± 41 Hz, N = 3, would consume 8.2 ms to achieve a comparable elevation. Therefore, the most likely cause for leg engagement is wing obstruction. As seen in Figure 3.6 and Movies S1-S3, wings moving from their resting position to their flight posture need to traverse a plane that intersects resting legs. By rapidly extending the legs downward, the legs leave the region occupied by beating wings. In Movie S4, we provide an instance where a mosquito is able to flap into the spaces between the middle and hind legs during leg extension, with wings contacting legs during this action. It is not clear if such a strategy would be effective if legs remained completely static,

but is clear that legs are extended prior to the first full wingbeat. In flight, outwardly extended legs are positioned forward and aft of the stroke plane.

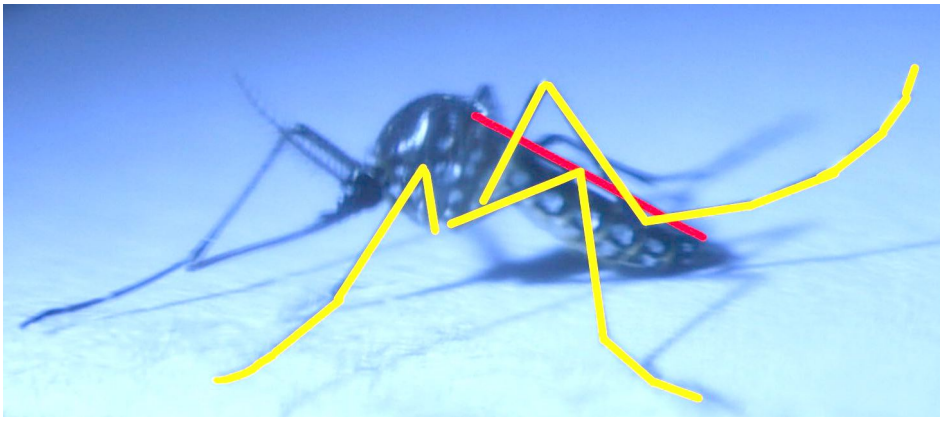

Figure 3.6: Photo of a resting mosquito with wings traced in red and left legs traced in yellow, showing the obstruction of wing traversal to the flapping plane by the legs.

Mosquitoes engaging a leg-strike sacrifice time for a low-slip takeoff, similar to Drosophila trading stability for acceleration in escape takeoffs [31, 29]. The shift of takeoff strategy from one surface to another suggests that insects are capable of judging the suitability of surface for takeoff, a capability which likely extends to other families of insects. Examples of fine adjustments to takeoffs may includes locust jumps from very loose sand or mosquitoes from liquid surfaces [90]. As takeoff surfaces become more complex, with surface features on the mesoscale, undiscovered takeoff techniques may emerge. Future studies are needed explore the methods and limits of insect evaluation of surface characteristics from temporal and topographical perspectives.

3.3 Chapter Summary

In this study we find *Ae. aegypti* mosquitoes taking off from horizontal surfaces employ two distinct strategies of takeoff, a 'push' and a 'leg-strike', the choice of which is influenced by surface roughness. Both strategies produce similar upward body velocities as the insect begins to beat its wings, 0.38 m/s and 0.35 m/s respectively, over brief timespans, 5.5 ms and 9.6 ms. On the

smoother surface tested, the majority of individuals (66%) employ a leg-strike action prior to a pushing action, which reduces tarsal slip. On the rougher surface, leg-strikes frequency reduces to 44%. The push takeoffs have one phase prior to wingbeat commencement, the extension of the legs. The force exerted on the takeoff surface by each pushing leg remains below the mechanosensory threshold of human skin, 0.07 mN. By comparison, leg-strike takeoffs have three phases, the downward swing of a rear leg, the impact of the leg, and the subsequent extension of all legs. The striking leg is modeled as a rotating cantilever beam attached to a cylindrical body where the values for force and body rotation are determined. The forces exerted by the striking leg, 0.025 mN, and pushing legs, 0.027 mN, likewise remain below the aforementioned threshold, with a minimal resultant body rotation of 0.34°. By fixing takeoff time and upward body velocity before the first full wingbeat, we conclude that mosquitoes choose a leg-strike velocity that allows them to minimize the peak force exerted to the takeoff substrate, potentially a human host.

CHAPTER 4: LANDING MOSQUITOES BOUNCE WHEN ENGAGING A SUBSTRATE

In this experimental study we reveal the passive mechanisms mosquitoes employ to engage hosts undetected. We observe mosquito landings with high-speed cameras and quantify displacement, landing forces, the employment of various appendages, and the ability of mosquitoes to cleave to surfaces across a range of relative velocities. We begin §4.1.1 with a description of the landing sequence and kinematics. We discuss the proboscis deformation upon landings §4.1.2 and model the proboscis as a cantilever beam buckling under impact force. In §4.1.3 we model the mosquitoes displacement at first contact with that of a classical mass-spring-damper system. We discuss implications of our results and propose future research avenues in §4.2, and provide concluding remarks in §4.3.

4.1 Results

4.1.1 Description of landing and orientation preference

The walls of the flight arena are briefly vibrated to encourage flight of resting mosquitoes. Mosquito landings are considered for analysis if a forward appendage (forelimbs or proboscis) initiates contact with the landing surface. All analyzed landings are shown in Figure 4.1 as smoothed curves and in Fig.S1 as raw curves. Temporal velocity for all landings are is plotted in Fig.S2. Mosquito flight posture is characterized by both forelimbs projecting outward with $\theta_{\text{legs}} = 118.4 \pm 8.1^{\circ}$, $N = 5$ with respect to one another if measured from the thorax dorsal center. Typical flight posture is shown in Figure 4.2**a,c** (Movie S1). Such a foreleg posture avoids lateral engagement of substrates up to an angle of incidence $\alpha = \theta_{\text{legs}}/2 = 59.2 \pm 4.1^{\circ}$. We limit our scope of analysis

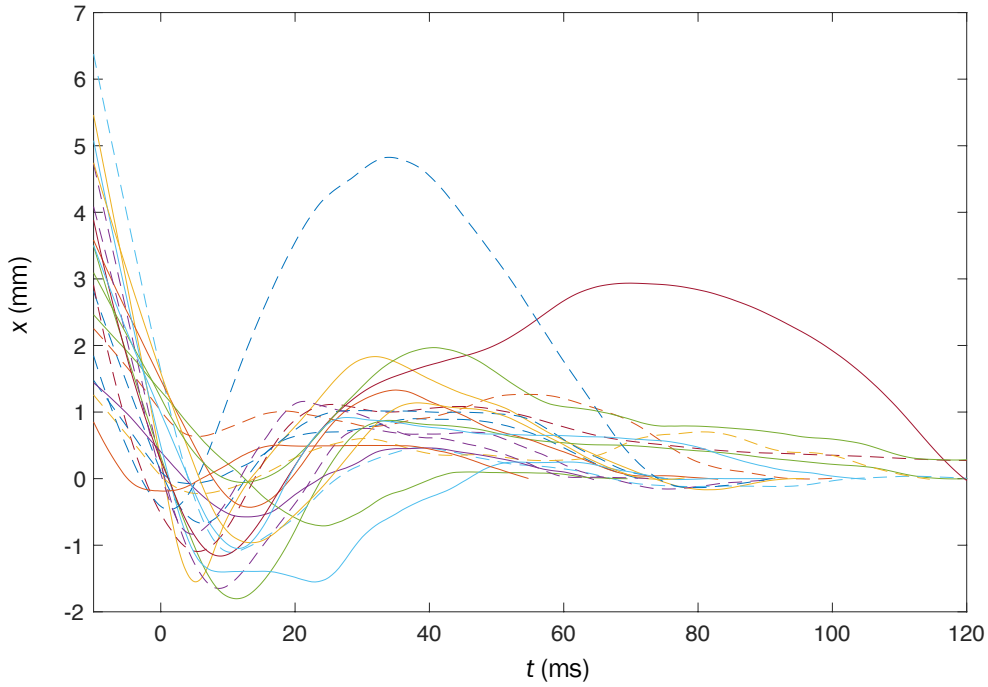

Figure 4.1: Normal-to-substrate displacement for all 20 analyzed landings. The tracked point on the mosquito is the interface of the proboscis with the head. The final resting position the tracked point corresponds to $x = 0$. First contact of any portion of the mosquito with the landing surface corresponds to $t = 0$. Dashed-curves indicate the proboscis is the first member to contact the substrate, while solid lines indicate tarsi initiate contact. Curves are smoothed with a Savitzky-Golay filter at 10% span.

to landings in which the angle of incidence of approach is less than α to eliminate landings which were slowed, or otherwise influenced, by grazing contact of aft legs and wings prior to substrate engagement.

Mosquitoes approach the test surface with a normal velocity $v_{\mathrm{n}} = -0.24 \pm 0.14$ m/s, N $= 20$, as shown in Figure 4.1 for $t < 0$. Upon tarsal contact with the substrate specimens rapidly decelerate, shown graphically in Figure 4.1 and Figure 4.2**a-b**. Sensing of the substrate prior to touchdown is likely done with a combination of vision and self-induced pressure wave detection [110]. Encounters with the substrate intermittently occur proboscis first, shown in Figure 4.2**d**, and produce compression of the forelegs and often buckling/deformation of the proboscis, lengthening impact time, seen in Figure 4.2**e**. Mosquitoes bounce from the surface at a normal velocity 0.16 ± 0.08 m/s,

N=19, and reverse course back toward the substrate at an average distance of 1.7 mm. A bounce is witnessed when the torso experiences movement away from the substrate. Landings in which tarsi do not separate from the substrate following initial contact display a single bounce. A double bounce landing is plotted in three dimensions in Figure 1.1**c**, two dimensions in Figure 4.2**a**, and pictured in Figure 4.2**f**. Only a single trial displayed no bounce. Mosquitoes display a bounce pattern which ceases when tarsal grip is sufficient to overcome bounce acceleration, within 3 bounces (Movie S2). Every bounce and subsequent approach acts to reduce the mosquitoes' incoming momentum by at least 50%, N=19. With forelimb tarsi securely in place, the abdomen and remaining legs swing downward to contact the surface as the wings cease flapping. Once coming to their resting position, Figure 4.2**g**, wings then rotate inward at an average angular velocity $12,977 \pm 4,844$ deg./s, $N = 5$ (left wing) and $12,943 \pm 4,932$ deg./s, $N = 4$ (right wing) to rest atop the abdomen approximately 100 ms after approach, as pictured in Figure 1.1**a**.

While we analyze only landings onto vertical surfaces in this study, we do quantify the frequency of landings onto vertical and horizontal surfaces within our flight chamber. Over the time-course of 5 minutes, beginning at the cessation of arena vibration, we count the number of landings onto the purple substrate when oriented vertical and horizontal, in separate trials. For each trial, 50 female mosquitoes were placed in the arena simultaneously. We count 29 ± 3, $N = 3$, landings on the vertical surface and a meager 3 ± 2, $N = 3$, landings on the horizontally oriented surface, a result which is in line with previous observation of mosquito preference [40]. We note that for many mosquito hosts, humans for example, vertically oriented surface area exceeds that of horizontally-oriented surface area.

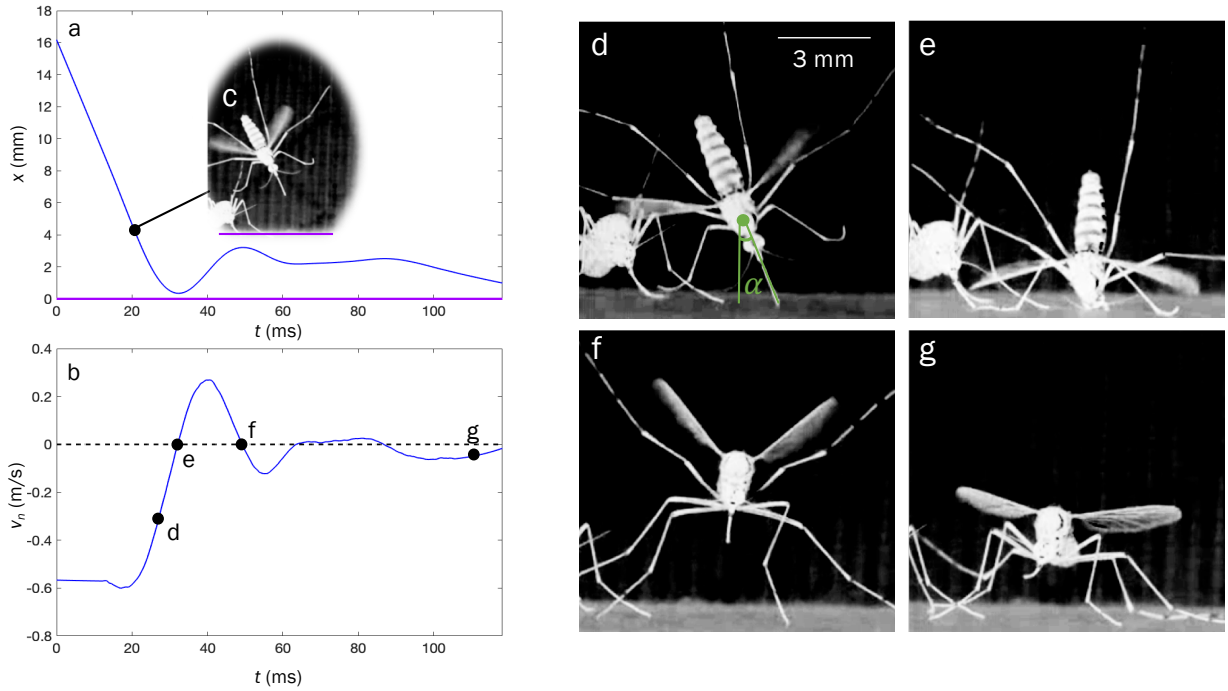

Figure 4.2: Mosquito landing plots for **(a)** Normal-to-substrate displacement versus time. **(b)** Temporal normal-to-substrate velocity. Data in plots (a) and (b) is smoothed with Savitzky-Golay filter at 10% span. **(c)** Initial deceleration of mosquito. **(d)** First contact of proboscis. **(e)** Collapse of the proboscis with head nearly contacting surface. **(f)** Maximum bounce displacement. **(g)** Final stabilization of landing position with eminent wing retraction.

4.1.2 Impact energy and proboscis bending

As legs compress, wings flap, and proboscises deform, mosquitoes absorb their in-flight kinetic energy $E_\mathrm{k} = mv_\mathrm{n}^2/2 = 0.061\ \mu$J, where the average mosquito mass $m = 1.66$ mg, N=30. In the absence of detailed wing kinematics and computational fluid dynamics, parsing the energy absorbed in the legs U_l from that absorbed by the wings U_w is not feasible, and is thus beyond the scope of the current study. Therefore, we quantify the energy absorbed U_p via proboscis deflection δ_p, preceding the initial bounce, seen in Figure 4.3**a,b** (Movie S3). Proboscis deflection is not seen in subsequent bounces and was present in 16 of 20 recorded landings. Altogether we may write $E_\mathrm{k} = U_\mathrm{p} + U_\mathrm{l} + U_\mathrm{w}$, and note that potential energy is neglected in our consideration of conservation

of momentum in the direction perpendicular to the landing surface.

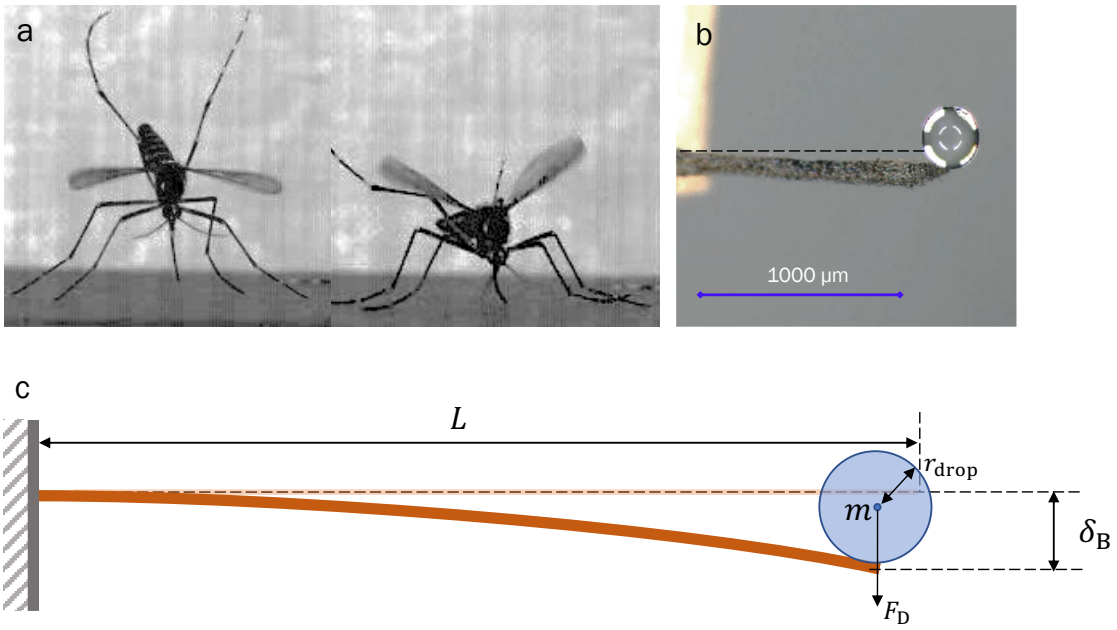

Figure 4.3: Mosquito landing with proboscis **(a)** initiating contact with substrate, and deflecting from normal force. **(b)** Modulus experiment with mosquito proboscis fixed on one end and loaded on free end with a water droplet. **(c)** Diagram of measured parameters depicting proboscis deflection due to end load.

Deflection of the proboscis δ_p is measured approximately $5-80\%$, N $= 16$, of proboscis length $L = 1.0-2.1$ mm. We acknowledge this degree of deformation very likely places the proboscis outside the linear-elastic regime. However, to gain an understanding of the role proboscis deformation plays in the landing process without knowing precise deformed curvature, we employ linear-elastic assumptions. We model the proboscis as an end-loaded cantilever beam where the proboscis deflection stores elastic strain energy $U_P = k_{eff}\delta_p^2/2$ and force is applied normal to the beam axis. The effective stiffness of the proboscis k_{eff} can be written in terms of elastic modulus E_p, area moment of inertia $I = \pi r^4/4 = 2.16\times10^{-6}\,\text{mm}^4$, and L, such that $k_{eff} = 3E_pI/L^3$, where proboscis radius $r = 43\pm2\ \mu$m, N $= 3$. The elastic modulus of the proboscis is determined by

measuring its deflection δ_D under the weight F_D of a droplet (see §2), such that

$$E_p = \frac{F_D \ell^3}{3I\delta_D}, \tag{4.1}$$

where the cantilevered proboscis length $\ell = 917 \pm 97$ μm, N = 3 and $\delta_D = 3.2 \pm 1.3$ μm, N = 3. Deflection of a proboscis by a drop can be seen in Figure 4.3b, and schematized in Figure 4.3c. We measure $E_p = 1.56 \pm 0.16$ MPa, N = 3, and from above,

$$U_p = \frac{3E_p I \delta_p^2}{2L^3}. \tag{4.2}$$

For the maximum observed value of $\delta_p = 0.8L$ and $L = 1$ mm, $U_p = 0.0032$ μJ. In the most extreme cases the proboscis is able to absorb up to $U_p/E_k \approx 5.4\%$ of the kinetic energy of the average mosquito approach.

If instead we consider an axially loaded proboscis, the critical buckling load P_{cr} required to produce tip movement δ_p, analogous to buckling a column,

$$P_{cr} = \frac{\pi^2 E_P I}{4L^2}, \tag{4.3}$$

we calculate $P_{cr} = 8.3\,\mu$N, well below the human detection threshold, 70 μN [32]. The exact energy calculation associated with buckling would require extensive post-buckling analysis and is complicated by complex material behaviors at large deformation. Such characteristics are not known for proboscises. Recent research in the crushing of slender structures indicates a rapid collapse of load bearing capacity at the onset of instability for even complex structures under both axial and bending loads [111, 112]. Conservatively, we assume linear force P degradation such that $P = P_{cr}$ at loading onset and $P = 0$ at complete collapse. The energy transferred to the proboscis is the sum of the collapse energy $U_{col} \approx P_{cr}L/2 = 0.0042$ μJ and the assumed negligible elastic

energy. Thus, $U_{\mathrm{col}}/E_{\mathrm{k}} \approx 6.9\%$. The agreement in values of U_{p} and U_{col} indicates the primary mechanisms for dissipating energy associated with orthogonal flight motion are leg compression and wing aerodynamics, discussed in §4.1.3.

4.1.3 Impact force mitigation by foreleg properties

Foreleg compression at touchdown lengthens impact time and reduces impact force by distributing momentum across multiple joints. Modeling the mosquito as a simple mass-spring-damper, where the legs act as the damped spring, allows for the determination of their effective damping coefficient c and stiffness k for comparison to those ideal for force reduction. To characterize dynamic response we vibrate the box floor beneath standing mosquitoes at a fixed frequency, 25 & 50 Hz. Upon nearly impulsive cessation of floor movement we measure free response of mosquito bodies and solve the corresponding equation of motion,

$$\ddot{x} + \beta \dot{x} + \omega_n^2 x = 0, \tag{4.4}$$

where $\beta = c/m$ and $\omega_{\mathrm{n}} = \sqrt{k/m}$. The amplitude reduction factor provides the damping ratio ζ of the mosquito,

$$\ln \frac{x_1}{x_2} = \frac{2n\pi\zeta}{\sqrt{1-\zeta^2}}, \tag{4.5}$$

where n is the number of cycles between amplitude measurements x_1 and x_2 equal to unity in our system (Figure 4.4a). Solving Equation 4.5 with both 25 and 50 Hz responses, $\zeta_{\mathrm{exp}} = 0.36 \pm 0.10$, N = 8, indicating the mosquito behaves as an underdamped system, explaining mosquitoes' propensity to bounce after first contact. The natural frequency of the mass-spring-damper analog $\omega_{\mathrm{n}} = \omega_{\mathrm{d}}/\sqrt{1-\zeta^2} = 256 \pm 39$ rad/s, where $\omega_{\mathrm{d}} = 239 \pm 36$ rad/s is measured from spatio-temporal data. The spring constant $k = m\omega_{\mathrm{n}}^2 = 0.109 \pm 0.002$ N/m, the critical damping coefficient $c_{\mathrm{c}} =$

$\sqrt{4mk} = 8.5 \pm 1.2 \times 10^{-4}$ N-s/m, and the actual damping coefficient $c = \zeta c_c = 3.1 \pm 0.5 \times 10^{-4}$ N-s/m. The general solution to Equation 4.4 is,

$$x(t) = e^{-(\beta/2)t}[A\sin(\gamma t) + B\cos(\gamma t)], \tag{4.6}$$

where $\gamma = \frac{1}{2}\sqrt{4\omega_n^2 - \beta^2}$, $A = [\beta x(0)/2 + \dot{x}(0)]/\gamma$, and $B = x(0)$. Using the aforementioned values of k and c, we plot Equation 4.6 in a dashed-black line next to a temporal track of a typical landing event, in Figure 4.4b, matching the initial condition $x(0) = 2$ mm of the data. We note reasonable agreement with experimental data through the first 20 ms of landing. Equation 4.6 does not capture the influence of aerodynamic damping of the wings, the wing-in-ground effect, and potential coulomb damping in the joints. Moreover, Equation 4.6 predicts the mosquito will accelerate slightly, a consequence of modelling legs as damped, outstretched springs.

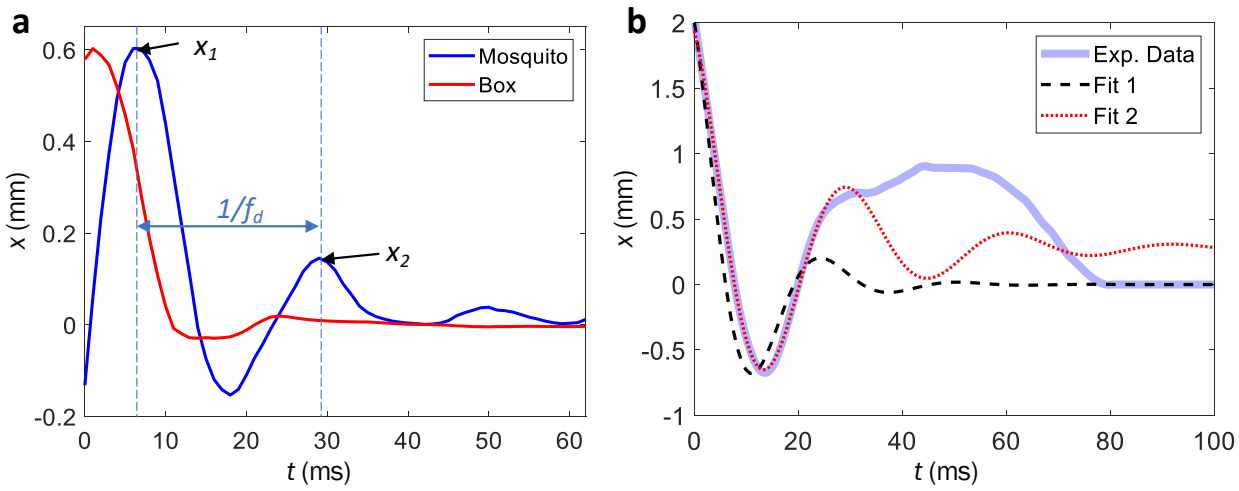

Figure 4.4: (a) Mosquito displacement over time for a mosquito standing on the floor of a box vibrating at 50 Hz. The curve is smoothed with a Savitzky-Golay filter at 10% span. (b) Experimental landing data, Fit 1 based on Equation 4.6, and Fit 2 from Equation 4.7.

An improved fit may be garnered by prohibiting the virtual spring in the mosquito leg to be ex-

tended prior to impact, adding a constant bias C, and phase shift ϕ,

$$x(t) = C + De^{(-\zeta\omega_n t)}\sin(\omega_d t + \phi). \tag{4.7}$$

Equation 4.7 is fit to the raw experimental data in Figure 4.4b with a nonlinear least squares solver, where C, D, ζ, ω_n, ω_d, and ϕ are free parameters. We plot the best fit provided by Equation 4.7 with a red curve in Figure 4.4b. The resulting $k = 0.07$ N/m, $c = 1.6 \times 10^{-4}$ N-s/m, and $\zeta = 0.23$ agree with those calculated from experiments of mosquito free vibration following an impulsively-stopped vibrating floor (Equation 4.5).

By setting $B = x(0) = 0$ in Equation 4.6 and taking the second time derivative we produce an equation for temporal substrate force that utilizes k, c, and ζ calculated through free vibration experiments,

$$F(t) = mAe^{-(\beta/2)t}\left[\frac{1}{4}\beta^2\sin(\gamma t) - \gamma^2\sin(\gamma t) - \beta\gamma\cos(\gamma t)\right]. \tag{4.8}$$

A range of $\dot{x}(0) = v_n$ is used plot the F against t in Figure 4.5. We plot only the first 10 ms, sufficient time for rebound to begin, as seen in Figure 4.4b. We assume the mosquito distributes the load uniformly between two front legs and neglect aerodynamic effects. The slowest mosquito landing provides an impact acceleration of 0.6 gravities, while the fastest impact produces 5.5 gravities. The range of landing velocities in our study is in agreement with in-flight velocities recorded in other studies [113, 114, 115]. The landing force of the average mosquito in our study is approximately 40 μN, falling short of human detection. However, covert landings are not universal as 3 trials (10%) record a magnitude of normal velocity greater than that which meets the human force detection threshold [32], 0.42 m/s. This result aligns with authors' experience of occasionally sensing a landing mosquito, less common than sensing the mosquito bite.

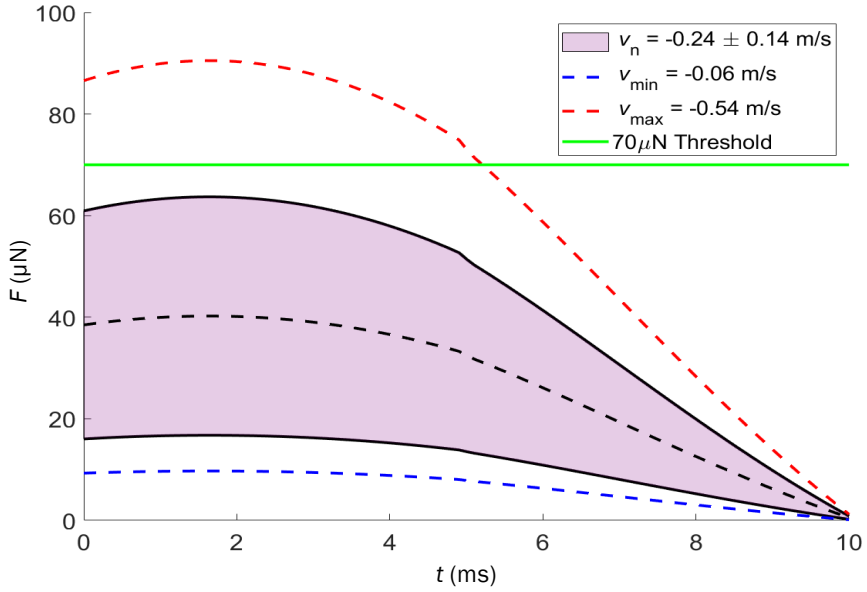

Figure 4.5: The temporal substrate force from Equation 4.8 for various landing velocities. Blue and red curves represent the slowest and fastest observed velocities, respectively, while the purple cone denotes the standard deviation around the average observed velocity.

4.2 Discussion

Our study reveals *Ae. aegypti* mosquitoes employ bouncing sequences, leg compression, and proboscis deformation to engage landing surfaces. Unlike bees [52], houseflies [116], and fruit flies [54], we do not witness mosquitoes prepare for landing by adjusting leg posture or body rotation. Their substrate interactions often have head and torso contact with the substrate (Figure 4.2e), but the associated forces are easily survivable and relatively small in the insect realm [56]. Proliferation mandates that landings are completed discreetly, below that which a host can sense, so that blood meals are completed unencumbered. Thus a mosquito employs multiple appendages to scrub momentum and reduce the force imparted by any one member. Any flyer, biological or engineered, aiming to land discreetly may control the effective length x_{eff} of impact over which flight is slowed under constant acceleration. Rearranging the equation of motion and assuming no reactions other

than those provided by the substrate,

$$x_{\text{eff}} = mv_n^2/F', \tag{4.9}$$

where F' is the landing force not to be exceeded. For mosquitoes we calculate $x_{\text{eff}} = 1.4 \pm 0.5$ mm for initial impact if using $F' = 70$ μN. This value of x_{eff} would be traveled in $\sim$6 ms, is $\approx 23\%$ of a mosquito body length [33], and $\approx 33\%$ of the mosquito foreleg, which appear exceedingly achievable. Yet, we observe greater compression distances by the proboscis alone, $\delta_{\text{P}} = 1.71$ mm, an observation that may be tied to insect perception rather than kinetics. However, it was recently discovered mosquitoes can sense sound pressure waves generated by their flapping wings rebounding from nearby surfaces, a sensory cue that is used to divert from unavoidable surfaces [110].

While the timescale over which landings occur is rapid, it is comparable to the timescale of takeoff [82] and lengthy compared to the timescale of a single wingbeat [117]. Thus, it is possible leg compression at landing is not wholly passive. Active engagement of leg muscles may contribute to the discrepancy between our passive model and experimental response of a landing mosquito. An active force modifier may be added to Equation 4.4 to better match mosquito responses, but the magnitude and time-response of such a force is currently unknown and an area for future work. Regardless of active contribution by legs to slow the mosquito, a passive model well-describes mosquito landing.

The spread posture of mosquito legs during flight, the same as upon landing approach, may serve a purpose beyond the previously proposed drag reduction benefits [33]. The oblique angle between the two forward tarsi, θ_{legs}, ensures that approach angles $\alpha \lesssim 60^\circ$ toward a vertical surface result in the contact of both forward tarsi. The engagement of the tarsi closest to the substrate induces body rotation to produce foreleg-substrate contact within 8.2 ms. The pliability of a proboscis to

absorb impact energy is meager in comparison to the complementary work of legs and wings, and does not obstruct the foreleg tarsi from contacting the surface. The low critical force for proboscis buckling, P_{cr}, allows the mosquito proboscis to collapse in the tangential direction at velocities well below the average value of v_{n}, ensuring the proboscis does not interfere with leg engagement.

We cannot confirm landings onto hosts are representative of those captured in this study, which may be described as controlled crashing. Mosquitoes use a variety of thermal, olfactory, and self-induced airflow cues in addition to vision to track their hosts [118, 110], but it is unclear how non-visual cues aid in clandestine landing. Mosquitoes are also nocturnal, avoiding obstacles invisible to their compound eyes [119]. We have witnessed activity in response to human attractants to be rather uncontrolled crashes when mosquitoes probe nets for passage [40], suggesting such behavior has no landing intent. Mosquitoes are likewise more qualitatively attracted to purple than the polished and translucent acrylic trialed in preliminary experiments, and previous literature suggests they can easily distinguish solid colors from patterns [42, 58, 120, 121]. The 40-mm high purple landing strip should stand out against its background and change in size as the mosquito approaches. If host landings differ from those on our surface, we expect they produce smaller substrate forces than we calculate as mosquitoes more adequately prepare for impact.

4.3 Chapter Summary

In this study we find *Ae. aegypti* mosquitoes experience bouncing when engaging surfaces to disperse in-flight momentum. In the first bounce, a mosquito will decrease its impact velocity by approximately 50%, and passively rotate its body, by virtue of its in-flight posture, to engage both pairs of fore- and mid-legs. Landings occur in approximately 100 ms from first contact to wing retraction, and are accompanied by proboscis deflection, which crumples as mosquitoes strike surfaces at an average normal-to-substrate speed of 0.24 m/s. We model the mosquito as a sim-

ple mass-spring-damper, finding a damping ratio of 0.36 ± 0.10, indicating mosquitoes behave as an underdamped system when engaging a surface, explaining their propensity for bouncing after their initial, and occasionally, subsequent impacts. We solve the ODE for free vibration with the assumption of uniform load distribution among both forelegs which indicates mosquitoes with normal-to-substrate speeds below 0.42 m/s, or 0.94 mph, are unperceptible by humans.

CHAPTER 5: HIGH-SPEED MICROJETS ISSUE FROM BURSTING OIL GLAND RESERVOIRS OF CITRUS FRUIT

We now shift our focus to our smallest organismal structure, citrus oil reservoirs. In this experimental and theoretical study we reveal the passive mechanisms permitting the jetting of minuscule amounts of oil at accelerations greater than 5,000 gravities. We begin §5.1 describing the sequence leading up to rupture, proceed to calculate the internal bursting pressure of reservoirs by hoop stress and fluid statics, and then present our scaling model in of an elliptical pressure vessel being capped by a stiff membrane. In §5.2 we present a discussion of our results and provide avenues of future research. We conclude with a summary of our work in §5.3.

5.1 Results

5.1.1 Rupture process

The process leading to reservoir rupture begins by establishing a strain gradient through a cross-section of a citrus peel. Physically, the gradient is established by bending a section of peel through a large angle of deflection, as seen with the Florida navel orange in Figure 5.1**a** and Movie S2. Bending increases stresses in the flavedo, with the most perceptible increase in the direction normal to the dashed blue line drawn in Figure 5.1**a-d**. The surface of a gland, as seen looking down onto a flavedo, can be seen in Figure 5.1**b-d** and outlined by a dashed black ellipse. As the magnitude of bending increases, a failure precursor wrinkle forms on the flavedo surface atop the oil reservoir, as seen in Figure 5.1**c,e**. Further bending induces the failure seen in Figure 5.1**d**, unveiling a channel to the gland reservoir. A higher resolution photograph of flavedo failure at jetting can be found in Fig.S2. The crack in Figure 5.1**d** begins atop the reservoir and is arrested by stomata surrounding

the gland. Stomata are outlined in Figure 5.1**e** and are small, nearly circular voids in the flavedo.

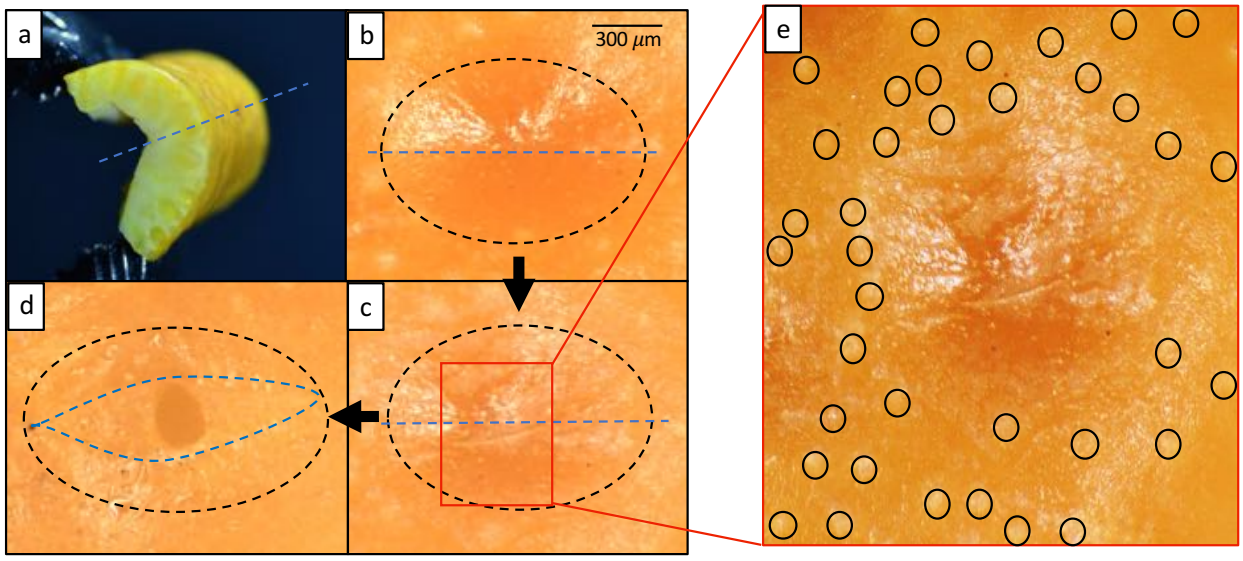

Figure 5.1: The process of glandular rupture. The process begins with bending a peel **(a)**. From an external view of the flavedo, the unstressed gland in **(b)** is stressed to eminent failure in **(c)** and to failure in **(d)**, which shows the channel leading to the oil reservoir. A zoom box of a crack forming prior to failure is shown in **(e)**. Black dashes outline gland extents beneath the flavedo and the blue dashed lines represent the line normal to externally applied stress.

5.1.2 Citrus jet kinematics

Through high-speed videography at $4,000-16,000$ fps, we film and track microjet expulsion from the five species of citrus hybrids listed in Table 5.1. Jets were produced by squeezing the exocarp of peeled fruits with fixed pliers. The sequence of jetting lasts about 0.5 s, where some jets finish before others begin. Digital tracking and measurement allows for characterization of initial jet velocity, temporal velocity decay of ejected jet fronts, and diameters of intact and broken jets.

We measure jet exit velocities V_0 across all hybrids within two weeks of purchase, finding a singular minimum of 1.58 m/s (mandarin) and singular maximum of 29.65 m/s (orange), with an average $V_0 = 8.47 \pm 4.03$ m/s (N=545) across all species. The average, standard deviation, minimum, and

Table 5.1: Citrus hybrid species used in this study and associated measurements. Velocity measurements were taken within the first two weeks of purchase.

Species	V_0 (m/s)	V_{min} (m/s)	V_{max} (m/s)	Cavity Vol. (mm^3)	Fruit Vol. (cm^3)
Florida Navel Orange					
C. sinensis	10.21 ± 5.25 (N=109)	2.98	29.65	0.83 ± 0.44 (N=100)	257 ± 29 (N=30)
Key Lime					
C. aurantiifolia	9.75 ± 3.26 (N=109)	3.41	16.80	0.25 ± 0.13 (N=100)	76 ± 12 (N=30)
Ruby Red Grapefruit					
C. paradisi	8.41 ± 3.45 (N=109)	2.13	16.83	0.79 ± 0.47 (N=100)	366 ± 58 (N=30)
Lemon					
C. limon	7.11 ± 2.98 (N=109)	2.10	14.13	0.63 ± 0.34 (N=100)	120 ± 19 (N=30)
Mandarin					
C. reticulata	6.83 ± 2.71 (N=109)	1.58	11.96	0.70 ± 0.42 (N=100)	73 ± 10 (N=30)

maximum V_0 for each hybrid is presented in Table 5.1. We find average V_0 for a citrus species to be independent of reservoir and total fruit volume (Fig. S1).

Florida navel oranges serve as the model organism to characterize jetting kinematics because of their attainability. Jet diameters are measured to be $D_0 = 102 \pm 20$ μm (N=10), using three individual oranges. We note that diameter measurements were taken as if jets had circular cross-sections, which is a simplification, as discussed in the Online Supplement. These measured jets have a corresponding range of $\mathrm{Re} = \rho V D_0/\mu = 349 - 1620$, indicating laminar flow.

Following emergence from a reservoir at V_0, jets rapaidly break up into streams of droplets, losing all streamline velocity $V_s(t)$ in less than 100 ms. We discuss jet instability in the Online Supplement. The temporal decay of $V_s(t)$ for a spherical droplet neglecting body forces can be expressed [122] as

$$m\frac{\mathrm{d}V_s}{\mathrm{d}t} = -3\pi\mu_a d f V_s, \tag{5.1}$$

where m is the droplet mass, d is droplet diameter, $\mu_a = 0.01845$ cP is the dynamic viscosity of air,

and f is the drag factor. Clift and Gauvin [123] provide an expression for f valid for subcritical $\mathrm{Re}_d = \rho_a V_s d/\mu_a$, where $\rho_a = 1.184$ kg/m^3 is the density of air.

$$f = 1 + 0.15\mathrm{Re}_d^{0.687} + 0.0175\mathrm{Re}_l \left(1 + 4.25 \times 10^4 \mathrm{Re}_l^{-1.16}\right)^{-1} \tag{5.2}$$

Integration of Equation 5.1 produces a curve for $V_s(t)$ that captures the deceleration of droplets, as seen in Figure 5.2**a**. Matching this model to experimental data is highly sensitive to the measurement of d, which is difficult at this scale and velocity; pixelation, image blur, and glare artifacts disrupt droplet outline clarity. For the droplet tracked in Figure 5.2**a,b**, we measure a droplet on-screen to have $d = 120$ μm whereas the model suggests the droplet has $d = 100$ μm. More generally, we measure orange jet droplets to have an average diameter $d = 119 \pm 31$ μm (N=50). Additional sources of model departure may include droplet elongation while in flight, and non-uniform shape as the droplets oscillate after breakup. We predict droplet evaporation does not significantly impact droplet kinematics. From a quiescent pool, we measure the evaporative flux of oil to be 0.156 ± 0.035 mg/min-cm^2 (N=5, 74°F, 52% RH). While moving droplets will evaporate more quickly, an evaporative flux 10x that measured for a quiescent pool yields a droplet volume change of $< 1\%$ for a 100 μm diameter droplet over a 100 ms flight.

The model of temporal velocity decay in 5.1 also provides insight into the change in jet size due to deceleration preceding breakup. While it is not possible to discern the exact breakup distance for these small jets, we do observe discrete droplets 2 mm from the flavedo surface (Movie S3). In the inset of Figure 5.2**b**, we plot the predicted velocity of a jet over the short distance relevant to breakup. Over 2 mm from emergence, the jet with $V_0 = 8.55$ m/s loses approximately 1% of its initial velocity, translating into an increase of diameter near 1 μm.

Jet velocities will deviate from those observed when jets fire out of the plane of observation of

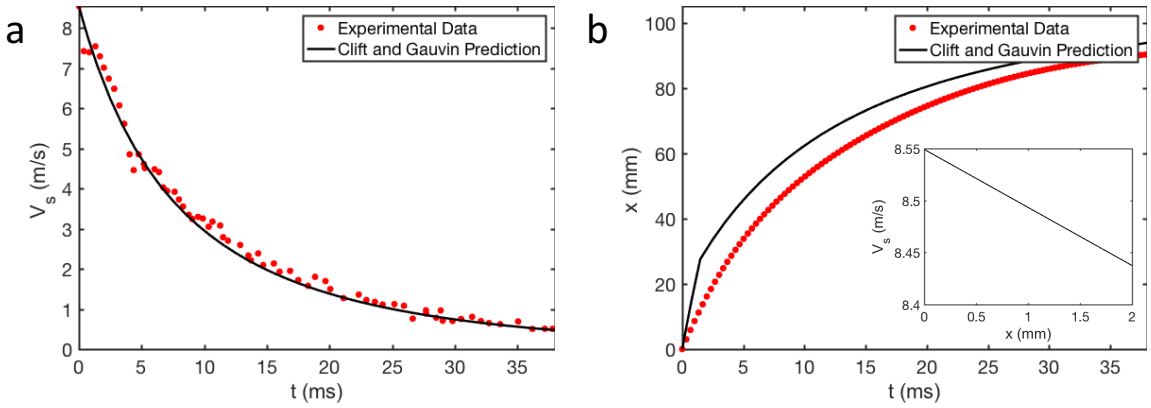

Figure 5.2: Temporal tracks of **(a)** droplet velocity and **(b)** position show droplet deceleration is rapid after expulsion from the gland.

the camera. This deviation is quantifiable such that the actual velocity $V_{0,a} = V_0/\cos\phi$, where ϕ is the angle of deviation from the viewing plane. We average 5 frames to quantify V_0, but combat error in velocity measurements by constraining tracking to jets that remain in focus for at least 40 frames (10 ms) for the focal depth of our lens $f_d = 7$ mm. A jet with $V_0 = 10$ m/s will have an average velocity $V_{\text{avg}} = 6.62$ m/s over the time of interest $\tau = 10$ ms according to Equations 5.1 & 5.2, and could have a maximum velocity measurement deviation $e = |\cos\phi - 1| = 0.55\%$, where $\phi = \arctan(f_d/\tau V_{\text{avg}}) = 6.0°$. For $V_0 > 4$ m/s, $e < 2.9\%$. The slowest recorded jet at $V_0 = 1.58$ m/s, $e < 8.6\%$.

5.1.3 Bursting pressure

We assume changes in pressure within the reservoir are negligible from the instant of flavedo rupture to the emergence of fluid into the atmosphere, which occurs over a period not observable with our camera at 16,000 fps, less than 63 μs. We consider a streamline from the gland reservoir center to the exocarp orifice, as seen in Figure 5.3**a**. The differential pressure between points 1 and 2 along the streamline may be expressed by a balance of static and dynamic pressures, neglecting

body forces,

$$P_1 - P_2 = \frac{1}{2}\rho\left(V_2^2 - V_1^2\right) + \Gamma, \tag{5.3}$$

where $P_2 = 0$ is atmospheric pressure, $V_1 = 0$ is oil velocity at rest in the reservoir, $V_2 = V_0$ is the oil velocity at bursting, and Γ is the excess pressure drop, namely the viscous loss imposed by flow constriction through a microscale orifice. Hasegawa *et al.* (1997) provides experimental data for pressure drop through orifices of comparable size and for $0 < \mathrm{Re} < 1000$ [124]. We infer that $\Gamma \approx 1.25\rho V_0^2$ at $\mathrm{Re} = 900$, which is independent of orifice geometry at that scale. From Equation 5.3 we calculate a gauge pressure for reservoir bursting $P_{\mathrm{burst}} = P_1 = 1.75\rho V_0^2 = 111$ kPa $= 16$ psi, for $V_0 = 8.76$ m/s, as measured one day after purchase.

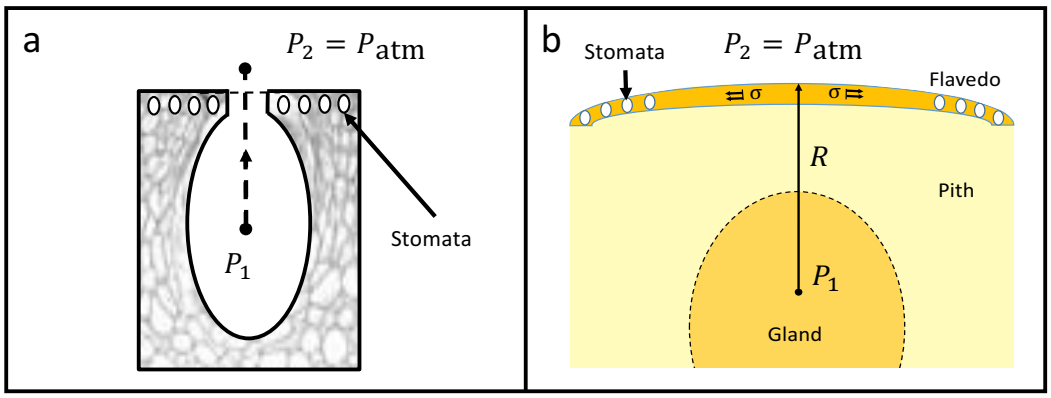

Figure 5.3: Schematics of oil gland reservoirs corresponding to two methods for calculating internal bursting pressure: **(a)** total pressure of flowing oil, and **(b)** hoop stress.

By measuring material properties of the flavedo, we may alternatively estimate P_{burst} from the hoop stress; which predicts the static fluid pressure at the moment of bursting without considering fluid flow,

$$P_{\mathrm{burst}} = \frac{\sigma_c t_{\mathrm{fl}}}{R}, \tag{5.4}$$

where σ_c is the critical stress to propagate a material flaw dictated by Griffith's theory [125], t_{fl} is flavedo thickness, and R is the radius of curvature of the flavedo cap at rupture. We find $t_{\text{fl}} = 84 \pm 28$ μm (N=10) for navel orange flavedos, and measure the radius curvature $R \approx 2-4$ mm upon bulk jetting inception, as seen in Figure 5.3**b**. Using tensile test data, we determine a range of critical stresses $\sigma_c = 2.22 \pm 0.23$ MPa (N=3) for oranges tested 1 day following purchase. Further discussion of the material properties of peels and the use of Griffith's theory is given in §5.1.4, and validation of hoop stress assumptions is given in §5.1.5. The range in values of R, t_{fl}, and σ_c yields $P_{\text{burst}} = 28 - 137$ kPa $= 4.0 - 19.9$ psi, which is in reasonable agreement with the value of P_{burst} predicted by Equation 5.3. Due to this agreement, we infer the hoop stress in the flavedo is very close to the hoop stress in the wall of the reservoir; the flavedo is extremely thin. We are unable to measure hoop stress in the reservoir walls directly due to inability to measure σ_{c} in the boundary layer membrane.

5.1.4 Relation of jet velocity to flavedo failure

Table 5.2: Stiffness and velocity values for all species tested at various times past purchase.

Species	V_0 (m/s)	E_{fl} (MPa)	V_0	E_{fl}	V_0	E_{fl}
	Day 1		Day 8		Day 15	
Key Lime						
C. aurantiifolia	10.61 ± 3.88 (N=9)	193 ± 31 (N=5)	12.40 ± 1.65 (N=9)	302 ± 57 (N=3)	13.88 ± 3.46 (N=9)	268 ± 72 (N=3)
Ruby Red Grapefruit						
C. paradisi	8.83 ± 3.52 (N=9)	125 ± 18 (N=5)	9.64 ± 1.51 (N=9)	116 ± 17 (N=3)	9.42 ± 4.63 (N=9)	52 ± 13 (N=3)
Florida Navel Orange						
C. sinensis	8.76 ± 4.94 (N=9)	97 ± 10 (N=5)	9.88 ± 3.13 (N=9)	113 ± 38 (N=3)	10.86 ± 1.63 (N=9)	113 ± 38 (N=3)
Lemon						
C. limon	6.91 ± 2.74 (N=9)	47 ± 13 (N=5)	8.61 ± 2.85 (N=9)	92 ± 25 (N=3)	9.27 ± 1.78 (N=9)	213 ± 110 (N=3)
Mandarin						
C. reticulata	6.63 ± 2.07 (N=9)	31 ± 11 (N=5)	7.68 ± 2.51 (N=9)	68 ± 18 (N=3)	8.66 ± 2.71 (N=9)	75 ± 27 (N=3)

We hypothesize that high-speed jetting requires a soft, compressible base layer, and a stronger, and stiffer external covering that withstands the buildup of fluid pressure in the reservoir and fails abruptly. To test our hypothesis, we seek a relation between jetting velocity and flavedo stiffness,

E_{fl}. We begin by mechanically separating flavedo from albedo to perform independent tensile tests, in contrast to previous studies which considered material properties of an intact peel [126, 127]. We find the albedo layer, averaging $E_{\text{al}} = 790 \pm 580$ kPa across all test species, two orders of magnitude less stiff than the flavedo layer, whose average stiffness at small strain ranges from $30 - 300$ MPa, reported in Table 5.2 and Figure 5.4 for each species. A typical stress-strain curve for an orange flavedo is seen in Figure 5.4**a**, and shows failure at engineering stress $\sigma_{\text{eng}} = 53$ MPa at large engineering strain $\varepsilon = 0.3$. On average, orange flavedos exhibited $E_{\text{fl}} = 103$ MPa for those tested 1 and 8 days following purchase and experienced complete failure around $\sigma_{\text{eng}} = 50$ MPa, which is comparable to the strength of acrylonitrile butadiene styrene (ABS).

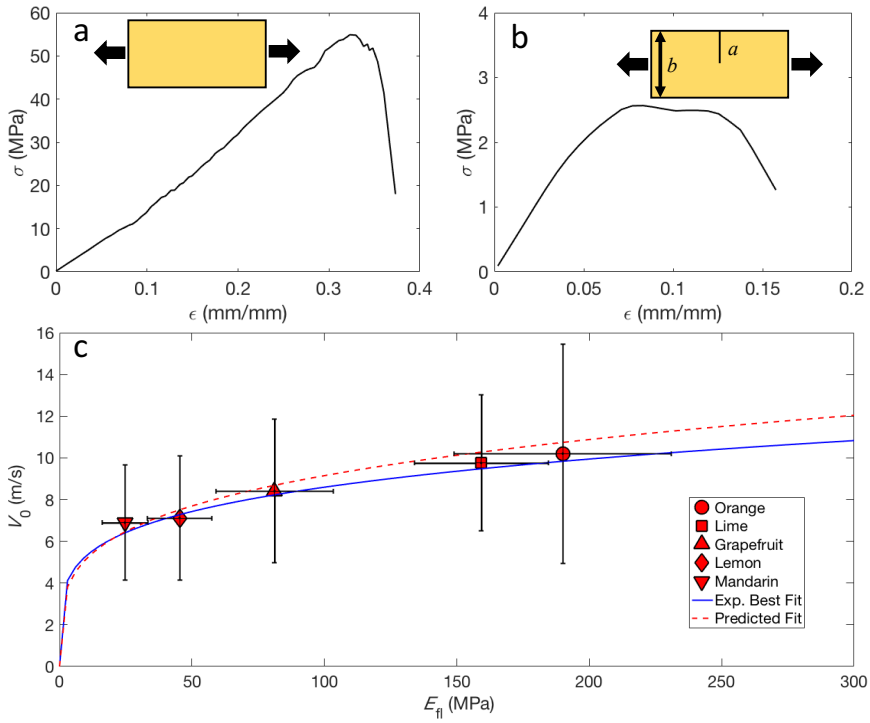

Figure 5.4: **(a)** Stress-strain curve for determining flavedo stiffness E_{fl} in an orange, with schematic of test specimen shown in the inset. **(b)** Stress-strain curve for crack propagation stress σ_{c}, with schematic of test specimen shown in the inset. **(c)** The relation between jet exit velocity (N=9 for each point) and E_{fl} (N=5 for each point), for fruits measured 1 day (filled symbols) and 8 days (open symbols) after purchase to quantify the effects of ripeness on jetting velocities and flavedo properties.

In §5.1.1, we describe that cracks in the flavedo begin atop the reservoir and are arrested by stom-

ata surrounding the gland. Over the region of interest, the 100 μm opening through which a jet emanates (Figure 5.1**d**), failure of the flavedo resembles the propagation of a flaw under remote tensile stress. Based on the flavedo's response under tension, as seen in Figure 5.4**a,b**, we treat the flavedo as linearly elastic just prior to failure and apply Griffith's theory [128, 129, 130] to form a scaling relation between flavedo stiffness and fluid jet velocity.

Before presentation of the scaling model derived from Griffith's theory, we address the impact of curvature on the validity of its use. Curvature induces coupling between bending and extension, which can result in deviation from the ideal flat material geometries used in traditional Griffith theory [131]. However, for curved sheets with low radii of curvature, deviation from ideal behavior is negligible. Folias (1970) [131] derived a scaling law to compare the ratio of near crack tip stresses in curved and flat sheets, σ_{curved} and σ_{flat} respectively. The ratio $\sigma_{\text{curved}}/\sigma_{\text{flat}} \approx (1 + 0.49\lambda^2)^{-1/2}$ for $\lambda < 1$, where $\lambda = a_0[12(1-\nu^2)]^{1/4}(Rt)^{-1/2} = 0.17$, $a_0 = D_0/2 = 50$ μm is half the flaw length, and $t = t_{\text{fl}}$ is the sheet thickness. We set Poisson's ratio $\nu = 0.49$ as done by previous works [132, 133] on comparable materials. When applied to citrus flavedos we find $\sigma_{\text{curved}}/\sigma_{\text{flat}} \approx 0.99$, indicating little influence of curvature on elastic behavior. Our use of D_0 as the length of the material flaw from which flavedo cracks begin is discussed in §5.1.5.

Griffith's theory [128, 130, 129] predicts the critical stress needed to propagate a material flaw in the flavedo and is expressed as,

$$\sigma_c = \sqrt{\frac{E_{\text{fl}} G_c}{2a_0\pi}}. \tag{5.5}$$

We address the variables in Equation 5.5 as dependent or independent of E_{fl}.

The strain energy release rate G_c is related to fracture toughness and elastic modulus as [130]

$$G_c = K_{\text{I}}^2 E_{\text{fl}}^{-1}, \tag{5.6}$$

where

$$K_{\mathrm{I}} = \sigma_{\mathrm{c}} \sqrt{2b \tan \frac{\pi a}{2b}} \cdot \frac{0.752 + 2.02\left(\frac{a}{b}\right) + 0.37\left(1 - \sin \frac{\pi a}{2b}\right)^3}{\cos \frac{\pi a}{2b}} \tag{5.7}$$

is the stress intensity factor [130], accurate to within 0.5% for any a/b. The value of G_c across the range of fruits used in the study is found by performing tensile fracture tests on peel samples measuring approximately 20 mm x 45 mm with precut 'cracks' of length $0.2b \geq a \leq 0.40b$, where b is the width of the test sample (inset of Figure 5.4**b**). A typical stress-strain curve for crack propagation tensile tests is shown in Figure 5.4**b**. We note the critical stress $\sigma_{\mathrm{c}} = 2.5$ MPa occurs at a moderate strain $\varepsilon = 0.15$ and is much less than the failure stress witnessed for uncut tensile samples. For oranges, $\sigma_{\mathrm{c}} = 2.22 \pm 0.23$ MPa (N=3), which dictates the value of P_{burst}, and according to Equation 5.3 is related to V_0. From Equations 5.6 & 5.7 we find $G_c = 1 - 14$ kPa-m across all species, and find no clear trend between G_{c} and E_{fl} (Fig.S3). We thus fix G_c as constant for our scaling argument.

We consider characteristic flaw length $2a_0$ in unbroken peels to be the size of the jet opening, and is fixed as constant for all species for our analysis . Therefore, from Equation 5.5 the scaling relation may be written, $\sigma_c \sim E_{\mathrm{fl}}^{1/2}$, and from Equation 5.3 we find $P_{\mathrm{burst}} \sim \rho V_0^2$. For the problem at hand, ρ remains constant and is omitted from subsequent scaling relations. Likewise, we see no trend in R from one fruit to another but find it is dependent on albedo thickness t_{al}, which is highly variable from one specimen to another and across individual fruits. We discuss the impact of variation in t_{al} in §5.2. Accordingly, Equation 5.4 provides the relation $P_{\mathrm{burst}} \sim \sigma_c$. Combining these relations yields the prediction,

$$V_0 \sim E_{\mathrm{fl}}^{1/4}. \tag{5.8}$$

We plot V_0 against E_{fl}, in Figure 5.4, and report the associated values in Table 5.2. The effect of fruit

aging is quantified by testing subsets of individual fruit specimens on 1, 8, and 15 days following purchase, such that these fruits produce both tensile test samples and velocity measurements. Data for days 1 and 8 is plotted in Figure 5.4 while data for day 15 is plotted only in Fig.S4c; signs of rot and excessive levels of material degradation are present two weeks after purchase. We fit Equation 5.8 to the combined data with $R^2 = 0.94$.

A power law best fit of the combined day 1 and 8 data yields

$$V_0 \sim E_{\mathrm{fl}}^{0.29}, \quad (R^2 = 0.96). \tag{5.9}$$

Thus among these species, we observe a clear dependency of jet velocity on flavedo stiffness. Generally the flavedos stiffen and jets attain higher velocities with age. It is noteworthy that the predicted exponent (0.25) is within the 95% confidence intervals of our experimental best fit (0.29), indicating excellent agreement between the predicted exponent and the measured one. We attribute this small discrepancy, which scales as $E_{\mathrm{fl}}^{0.04}$, to simplifications in our model, most likely regarding variation in peel properties across species and some nonlinear effects, discussed in §5.2. We report pre-factors, exponents, and coefficients of determination for the aforementioned fits of the form $V_0 = mE_{\mathrm{fl}}^n$ in Table 5.3. Days 1, 8, and 15 are all fit with Equations 5.8 & 5.9 separately in Fig.S4, and include standard deviation bounds.

Table 5.3: Fitting parameter data corresponding to the curves in Figure 5.4 of the form $V_0 = mE_{\mathrm{fl}}^n$.

Fit Type	*Day 1 & Day 8*	*Day 1*	*Day 8*
Exp. Fit			
m	*2.310*	*2.543*	*2.291*
n	*0.2926*	*0.2671*	*0.2979*
R^2	*0.9551*	*0.9689*	*0.9480*
Model Fit			
m	2.833	2.752	2.901
n	0.2500	0.2500	0.2500
R^2	0.9350	0.9652	0.9331

5.1.5 *Exocarp bending simulation*

A notable material property contrast between albedo and flavedo layers is elastic modulus. FE simulations allow us to test a range of moduli and reservoir geometry to determine their impact on P_{burst}. Additionally, FE modeling provides a view of the pressure distribution in the volume surrounding the reservoirs and across the flavedo surface. We model a unit of peel comprised of $t_{\text{al}} = 3.90$ mm thick albedo containing a single oil gland reservoir covered by $t_{\text{fl}} = 100$ μm of flavedo, as seen in Figure 5.5. We assume the entire peel geometry can be reconstructed by tessellating this representative volume element (RVE). The remote bending load on the peel (Figure 5.1**a**) is transferred to the RVE by rotations on either side of the unit cell as denoted in Figure 5.5**a**. Oil in the reservoir is modeled as static, incompressible and not subject to body forces. The reservoir geometry is made to mimic that observed in peel cross sections, an ellipsoid with longitudinal radius α and transverse radius β. Ratios α/β are chosen such that the volume of the reservoirs remain a constant 1 mm^3.

We set the values of E_{fl} and E_{al} according to ranges in experimental data, and fix Poisson's ratio at 0.49 and 0.25 respectively, as done by previous works [132, 133] on analogous materials. For

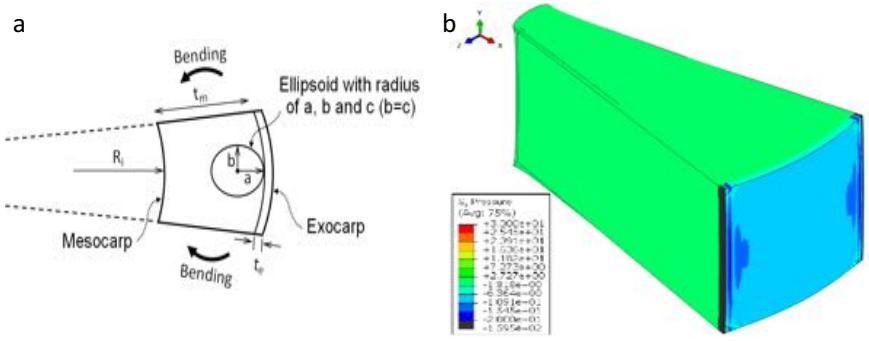

Figure 5.5: **(a)** Schematic of unit cell undergoing rotation at boundaries. **(b)** In-plane hoop stress showing approximately uniform tensile conditions with a local maximum at the center. This region of greater stress is most likely to fail first, which is supported by experiments. The white ellipsoid is the gland beneath the flavedo.

all simulated moduli and fluctuations in peel bending curvature $\Delta\kappa$, in-plane hoop stress contours across the flavedo indicate higher stress atop the oil reservoir, shown in Figure 5.5**b**, supporting the previous calculation of P_{burst} by a hoop stress model in Equation 5.4 and our choice of $a_0 = D_0/2$. Here, $\Delta\kappa = 0$ corresponds to a round, and unperturbed fruit with $R = 40$ mm. We plot oil gland reservoir pressure P as a function of bending severity, as $\Delta\kappa$ is increased from $0 - 0.25$ mm^{-1}, as seen in Figure 5.6**a**. The dotted lines show increasing P for greater curvature using range of material stiffness ratio $\eta = E_{\text{fl}}/E_{\text{al}} = 100$ (dashed line) and 500 (solid line), and $\alpha/\beta = 1.75$. Greater discrepancies in stiffness produce greater reservoir pressures. Pressures in the range of $80 - 160$ kPa is in good agreement with the estimate for fluid pressure given by Equation 5.3, 111 kPa, and the range predicted by Equation 5.4, $28 - 137$ kPa.

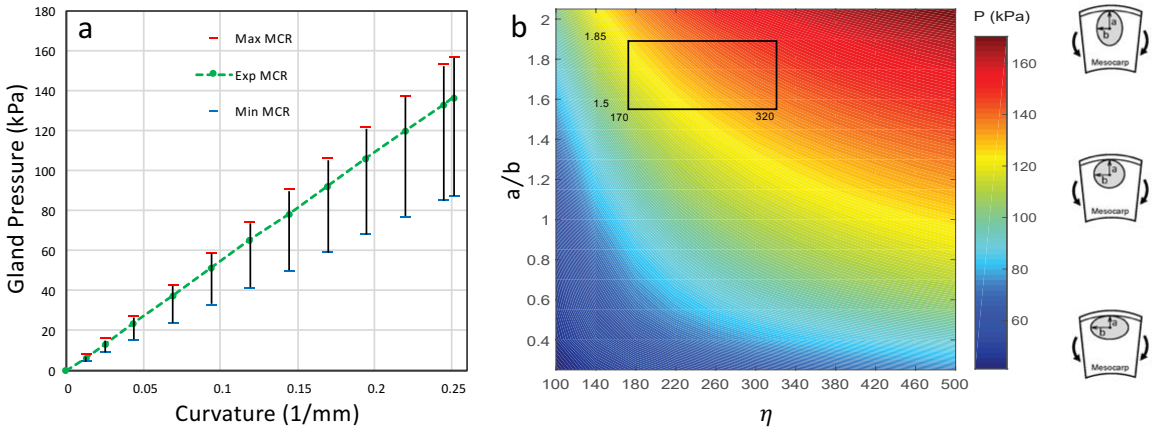

Figure 5.6: Pressure in oil gland reservoir simulated by varying **(a)** change in curvature for fixed $\alpha/\beta = 1.75$, and **(b)** gland eccentricity α/β and material stiffness ratio $\eta = E_{\text{fl}}/E_{\text{al}}$. The box in (b) bounds experimental values of α/β.

By fixing $\Delta\kappa = 0.25$ (mm^{-1}), a highly bent peel, we can perform a parametric FE simulation to understand the influence of reservoir shape (α/β) and η on P. The phase plot in Figure 5.6**b** shows that for $\alpha/\beta < 1$, P remains low, even for large values of η. Pressures are highest for vertically lobed reservoirs, such that $\alpha/\beta \approx 2$. Like Figure 5.6**a**, the plot in Figure 5.6**b** shows that contrasting flavedo and albedo stiffness is likewise critical to the generation of high fluid pressure and will elevate fluid pressure when α/β is slightly adverse. Experimentally observed ranges for

α/β are bounded by the black box in Figure 5.6**b**.

5.2 Discussion

Our study elucidates the mechanisms underlying the high-speed microjets emitted from the exocarps of citrus fruit. The velocity of these jets is a result of quickly releasing internal oil gland reservoir gauge pressures in the approximate range of $30-140$ kPa. The buildup and release of pressure is made possible by the composite nature of the citrus peel, namely a thick, compressible albedo that houses reservoirs and is capped by a thin, stiff flavedo. In general, fruit aging causes flavedo modulus to increase and produce greater jetting velocities. A greater understanding of this system may lead to technologies which mimic the bursting of oil reservoirs to disperse or aerosolize small amounts of fluid and new tools to characterize fruit.

The choice of applying Griffith's criteria in §5.1.4 requires simplifying assumptions. Using uniaxial tensile test data, we find the flavedo is a nonlinear, stiffening material before failure, with a small strain elastic modulus, $E_{\text{fl}} = 31-302$ MPa. While this is contrary to Griffith's theory of fracture [128, 129, 130], the flavedo does not exhibit pronounced ductile behavior. The reason for brittle behavior following stiffening is unclear but could be a result of little resistance to crack growth (flat R-curve) [125] offered by loosely held polymeric chains. This justifies the use of a single fracture toughness parameter for the current study. In recent past, a computational study using atomistic simulations captured strain stiffening, hyperelastic behavior on crack propagation, and found significant influence of hyperelastic behavior on the crack tip dynamics but the fundamental scaling law which we have used, $\sigma_{\text{c}} \sim E_{\text{fl}}^{1/2}$, was found to be valid [134]. For hyperelastic strain stiffening materials (such as neo-Hookean or exponential hardening), recent work [135] has shown that energy release rate remains very close to linear elastic fracture mechanics (LEFM) values for moderate values of $k = G_{\text{c}}/Ea_0$ (< 1) and moderate stress tri-axiality. According to Figure 5.4**c**,

the fruits most critical to curve fitting lie the furthest from the origin. And so for limes, $k \approx 1/3$. The authors [135] found the agreement even better if the stiffening is exponential in nature. We are thus justified in basing our scaling analysis on LEFM in this study.

This study highlights that citrus jet velocity is a function of flavedos' fracture toughness, most clearly demonstrated by Equation 5.4. Therefore, peeling citrus does not require careful extraction of the albedo, nor does natural variation in albedo thickness across the fruit impact local jet velocities. However, the curvature of the peel during jetting is strongly dependent on albedo girth. The line in Figure 5.6**a**, will decrease in slope with decreasing albedo thickness, therefore requiring higher values of $\Delta\kappa$ to achieve a critical bursting pressure.

The size of citrus oil reservoirs and the velocity of oil ejection result in large accelerations by jetting fluid. Liquid at rest in the pockets is accelerated to velocities in excess of 10 m/s over the distance of approximately 1 mm. Assuming the fluid is incompressible and acceleration is constant, parcels of fluid in the reservoir will experience 5,100 gravities (g) of acceleration before exit which is comparable to the acceleration of a bullet leaving a rifle. In nature this acceleration is outdone only be the mantis shrimp [136] (*Stomatopoda*) at over 10,000 g and Dung Cannon fungus [137] (*Pilobolus crystallinus*) at 180,000 g, but is perhaps unmatched in the plant kingdom. A notable contender in the plant kingdom is the bunchberry dogwood flower, which launches stamen at 2,400 g as petals open at 2,200 g [138].

Our results and FE investigations predict reservoir fluid pressures in agreement with Equations 5.3 & 5.4, but it would appear citrus fruits achieve suboptimal configuration from the standpoint of achieving even higher pressures by not maximizing η. However, note that top right corner of the phase plot would represent much stiffer flavedos. This material synthesis is likely limited due to the biological origin of the material. Therefore, the system leverages reservoir geometry for enhanced performance (high P_{burst}) indicating the observed values of α/β. Such is a recurring theme in

many biological systems where the limitations of material properties are overcome by geometry or topology of the structure [139, 140, 141, 142, 143, 144, 145, 146, 147, 148, 149, 150, 151]. In contrast, an outer layer with very low strength would not withstand the stresses associated with pressure rise in the small reservoirs, and would thus rupture at lower pressures and produce slower, yet more stable jets.

5.3 Chapter Summary

In this study, we demonstrated that high-speed micro-jetting of oils contained in citrus exocarps subjected to external bending stresses share commonality across citrus species. Oil jets emitted from citrus peels are capable of achieving initial velocities greater than 10 m/s, and are propelled by internal bursting pressures of $60-190$ kPa. The generation of such pressure is made possible by the composite nature of the peel, a pliable albedo bed of modulus $E_{\text{al}} = 790$ kPa surrounding each oil gland reservoir is capped by a stiffer, thin flavedo of $E_{\text{fl}} = 25-195$ MPa. The stiffness of the flavedo cap determines the internal bursting pressure of a gland and ensuing jet velocity. Finite element simulations reveal oil gland reservoirs' ellipsoidal geometry permit higher pressures than do spherical reservoirs.

CHAPTER 6: CONCLUSION

We have detailed the results of this combined theoretical and experimental dissertation on how classical engineering systems are analogs to complex insect and plant biomechanics. We began investigating the behavioral biomechanics between mosquitoes and substrates in Chapter 3 in their takeoff phase of flight. *Ae. aegypti* mosquitoes taking off from horizontal surfaces employ two distinct strategies of takeoff, a 'push' and a 'leg-strike', the choice of which is influenced by surface roughness, where each strategy produces similar upward body velocities of 0.38 m/s and 0.35 m/s, respectively. The 'leg-strike' is a modified 'push' style that begins with a swinging hind-leg that strikes the substrate at 0.59 m/s before engagement of quadrepedal pushing. We model the swinging leg as a rotating cantilever beam and the mosquito body as a cylinder rotating longitudinally, whereby the swinging leg produces an upward body velocity of 0.01 m/s with a corresponding body rotation of 0.34°. An analysis of the force imparted to the substrate for both strategies reveals that mosquitoes remain clandestine, never exceeding the subcutaneous threshold for detection. In Chapter 4 we assess the landing phase of mosquitoes and their subsequent rebound off the substrate. The 'bounce' of the mosquito works to scrub momentum for subsequent landing attempts, reducing incoming velocity by 50%. We modeled the motion of the mosquito upon first contact as a mass-spring-damper system and solve for damping ratio, coefficient, and spring constant experimentally. We detail that mosquitoes behave as an underdamped system, with a damping ratio of 0.36, and validate the model by fitting the general solution of the ODE for free vibrations to mosquito landing motion with a nonlinear least squares solver. We differentiate the general solution and solve for the force imparted over a range of initial velocities to find mosquitoes remain clandestine underneath a relative velocity of 0.42 m/s. Future researchers may determine the trade in lift generation by the engagement of flapping wings in the takeoff phase and the effect wing flapping has throughout the 90° rotation in body pitch through landing.

In Chapter 5 we focus on our smallest organismal specimen, citrus reservoirs. We filmed the microjets of 5 citrus species under compression using high-speed videography in 2D, and detail how the peels composite nature allows for their production. We find the jetted oil accelerates out the reservoir at rates greater than 5,000 gravities, and through fluid kinematics we determine an internal bursting pressure range of $30-140$ kPa. We compare this with hoop stress and find similar results for internal bursting pressure, $28-137$ kPa. We propose a scaling model derived from Griffith's criteria that predicts initial jet velocity scales with elastic modulus to the quarter power, and experimentally find the power-law best fit of 0.29 across our 5 citrus species. We hypothesize that the pressure generation is due to the contrasting stiffness around a pressure vessel, where the reservoir is modeled as an ellipsoidal pressure vessel surrounded by a compressible ductile membrane (the albedo) and capped by a thin stiff membrane (the flavedo). A FE simulation is done and confirms for highly bent peels ($\Delta k = 0.25$) with a contrasting stiffness ratio range of $100-500$, the pressure generation produces between $60-160$ kPa. Future researchers may look to exploit the contrasting elastic moduli in fabrication of composite materials, where functional jetting may be tuned by material stiffness ratio and fluid pocket eccentricity.

Organismal response to environmental pressures provide fruitful analogs for engineers to incorporate into their own designs. As engineering design and fabrication continue to explore the scales of the meso, micro, and nano the research of organismal behavior at these scales will prove advantageous. It is my hope that this collection of investigations into ephemeral behavioral from organisms on the mesoscale produce new avenues with which to contend with commonplace environmental pressures. In this dissertation we have modeled both insect and citrus fruit behavior as classical engineering system through high-speed videography.

APPENDIX A: ORGANISMAL AGGREGATIONS DISPLAY FLUIDIC PROPERTIES

In this appendix we extend the classification of engineering analogs to that of collective motion in insects, mammals, and fish. We propose fluidic behaviors are analogs to aggregate motion. By reviewing published literature on collective behavior we draw parallels to fluidic properties. We begin §A.1 by discussing how starling, locust, and ant aggregations display behavior which parallels fluid phases. We proceed to compare aggregate response to both viscosity in §A.1.2 and surface tension in §A.1.3. We conclude by summarizing the behaviors that drew close resemblance to fluidic properties in §A.2.

A.1 Discussion

A.1.1 Phase

Density and compressibility

Density is defined as the degree of compactness of a substance and has physical units of mass per volume. For fluids, large density is achieved by heavy and closely-packed molecules, and liquids are thus denser than gases. In the context of organismal aggregations, density may be characterized in a number of ways, to examine how inter-member spacing elicits particular aggregate behaviors. In general, the grouping of conspecifics to a threshold density enables information transfer and collective behavior through interactions between members [152, 153]. The simplest metric of aggregation density ρ is the number of individuals N in a given area A (in two dimensions) or volume V (in three dimensions), without regard to the mass of the individual. However, definition of the boundary of the aggregation area or volume is not straightforward [154]. The presence of inclusions within the aggregation or concave regions on the border mean that simple approaches such as a convex hull poorly represent the true aggregation area or volume [3]. Instead, it is first necessary to determine the minimum scale of concavities which characterize the aggregation and

then to account for those using an alpha-shape algorithm which identifies concavities larger than this minimum scale and excludes them from the area or volume [3]. An alternative metric of density in organismal aggregations is the packing fraction, which takes into account both the aggregation density and the organism area or volume. The need for this metric is motivated by observing that the packing of an aggregation of 100 starlings in a cubic meter is much greater than the packing of 100 bees in that same volume [154]. In three-dimensional aggregations, the volume occupied by an organism often is represented by a sphere with radius r, and the packing fraction is thus $\phi = 4/3\pi\rho r^3$, which is the ratio between the volume individually occupied by the collection of N spheres and the aggregation volume as a whole. However, it should be noted that some elongated organisms such as fish and bacteria are better represented by ellipsoids than by spheres [155], and the corresponding ellipsoidal packing fraction would then be $\phi_e = 4/3\pi\rho abc$, where a, b, and c are the ellipsoid's principal semi-axes. Gases are dilute and thus have a low packing fraction whereas the packing fraction of liquids is substantially greater.

A related and possibly more biologically relevant parameter related to aggregation density is the nearest neighbor distance. After all, each aggregation member does not have the capability to determine the aggregation density as a whole but instead can sense the distance from itself to a small number of neighbors [3] and adjust its own position accordingly. Nearest neighbor distances are often expressed in terms of a characteristic body dimension such as body length or wingspan. For starling flocks [3], Ballerini *et al.* (2008) determined nearest neighbor distance distributions from three-dimensional reconstructions of two-dimensional images where individuals appear as particles as seen in Figure A.1**a**, much like experimental use of particle image velocimetry (PIV). These researchers found that individual starlings retain a minimum average working distance from other members of $1-4$ wingspans [3]. The reason for this spacing is unknown but the minimum density is likely bounded by communication limits and the maximum density bounded by high probability of collision with other members. Distributions of nearest neighbor distances in organismal

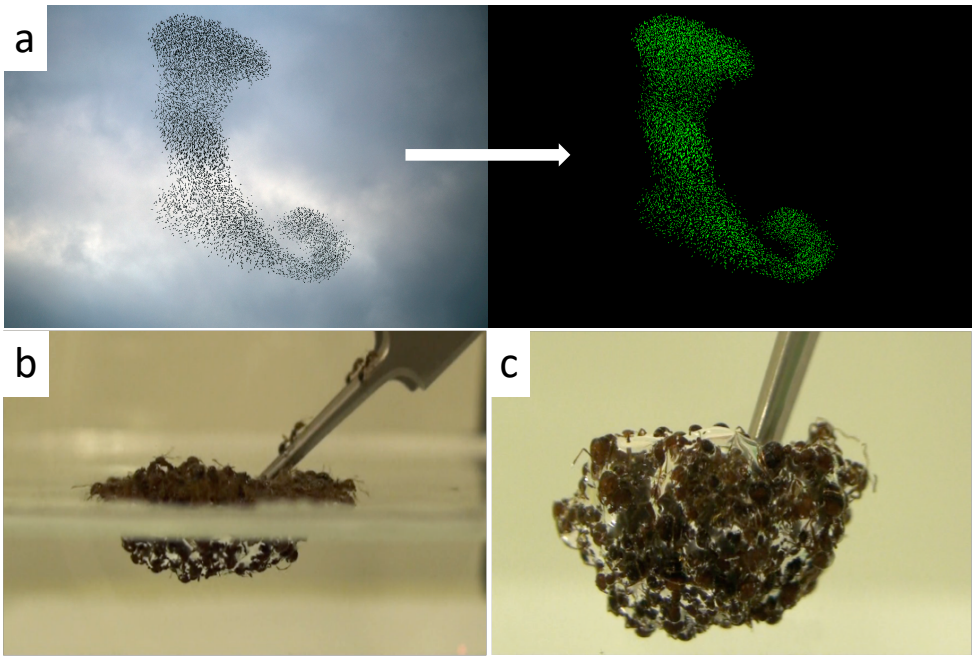

Figure A.1: Images of **(a)** starling flock to be used for stereophotogrammetry (left) and the same image after post-processing where birds are treated as particles (right) [1]. **(b)** partially submerged fire ant raft [2], **(c)** fully submerged fire ant raft [2].

aggregations are often well described by log-normal distributions [155, 156, 157].

A characteristic which both organismal aggregations and fluids share is that the density may not be homogeneous throughout the domain. For example, a compressible fluid droplet being acted upon by an external surface force would experience a pressure gradient in the fluid reflecting the higher density (or smaller distance between fluid molecules) in that region. A simple example of this phenomenon would be the high-speed impact of an unyielding ball on an air-filled balloon. Similarly, organismal aggregations have heterogeneous density. Starling flocks, for example, exhibit variable density with anisotropic spacing throughout the flock volume [3]. Starling interactions rely on topological distance, meaning they rely on the motion of $6-7$ of their nearest neighbors to change direction and respond to perturbations, independent of their interstitial spacing [158, 159, 160]. Heterogeneous density may be characterized in animal groups and in collections of particles by

parameters such as the integrated conditional density and the pair distribution function [154].

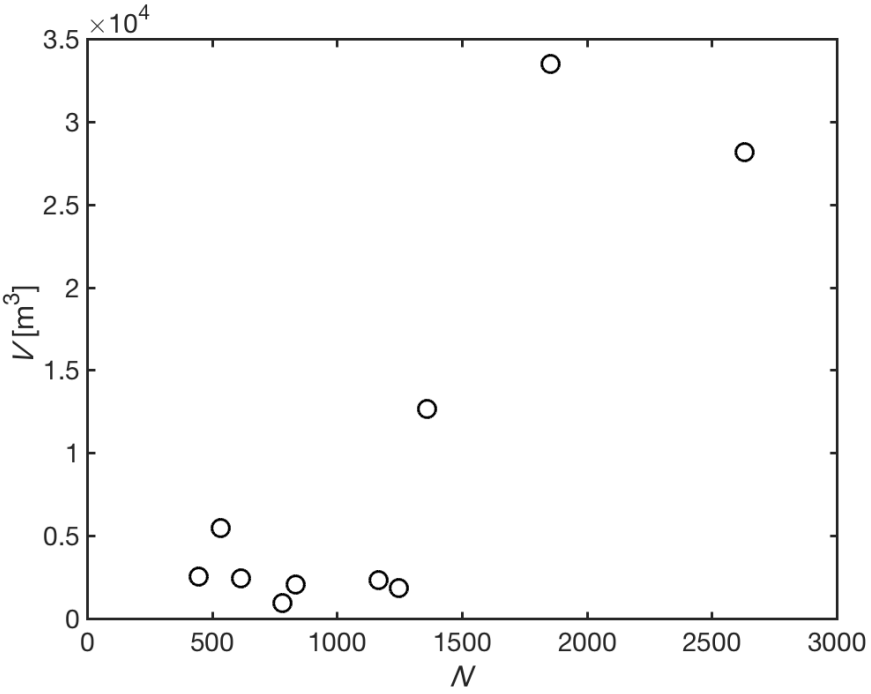

Figure A.2: Starling flock volume as a function of flock population [3].

As with unbounded fluids, starling flock volume is independent of the number of members [158, 3]. For example, a particular flock of $N = 530$ members amassed a cubic volume $V = 5470$ m^3, whereas a similar flock of $N = 1250$ had $V = 1840$ m^3. We plot V vs N data from Ballerini *et al* (2008) in Figure A.2. Such a spread in density does not allow for the calculation of a compressibility factor $Z = C \times (V/N)$, where C is an unknown constant, which we would expect to be nearly constant for conspecifics operating in comparable conditions [161]. However, variability in density may instead be akin to thermal expansion. Measurement of per member movement within a flock as a function of density is an area for future research.

Locusts, specifically *Locusta migratoria* are known to amass swarms [162, 163] that dwarf starling flocks and can cover $> 10^5$ acres. One study found the density of the airborne locust swarm is $0.001 - 0.5$ m^{-3}, with roughly $2 - 4$ m between neighboring flyers [164]. In contrast, a differ-

ent study [165] documented localized density variations, with greater density in the aggregation interior than on the edges. Swarm density for populations in excess of a billion members is critical for cohesion. Minimal working distance would logically be driven by collision avoidance and maximum distance is capped when information transmission becomes imperceptible. Simulations of massive locust swarms show a pure attraction between members is not effective in modeling these swarms as the simulation tends to create tight spherical swarm models [166]. The addition of a repulsive term weighted greater than the attraction term for short length-scales results in a dispersed yet cohesive swarm model [163].

In contrast to flying aggregations, *Solenopsis invicta* ants form cohesive clumps by grappling onto one another [2]. The clumps of ants can spread, drip, and withstand applied loads, displaying elastic behavior [167]. A manifestation of this clump is the ant raft (Figure A.1**b**), which is formed by colonies during floods for survival [2, 168]. Ant rafts are porous, allowing them to be both strong and lightweight, and giving the raft buoyancy whilst prohibiting water ingress, as seen in Figure A.1**c**. Paradoxically, ants cluster to greater densities (N/V) to form aggregate material densities (mass/V) that are lower than the individual ants' material density due to the ability of the clump to entrap air when fully or partially submerged. This behavior is analogous to a fluid immiscible with water and specific gravity less than unity floating atop a water surface. Unlike fluid molecules, ants do not move radially as the raft forms, but on average travel via random walks of 3.1 radii before settling on the raft edge [2].

Phase Transition

Transitioning between phases is a common occurrence in many working fluids used today. A fluid may evaporate from a more organized phase (i.e. a liquid) to a less organized phase (i.e. a gas) through the addition of energy from heat or the reduction of pressure. Organismal aggregations also exhibit different levels of organization which can be characterized as different 'phases.' The transition between phases occurs in a manner analogous to evaporation and condensation, which

is accompanied by changes in temperature and pressure. Temperature is a measure of the thermal motion of molecules, and pressure a measure of the physical molecular interactions in bounded fluids. The organismal analog to temperature is the increased physical activity of individuals, which increases the likelihood of physical interactions between members (pressure) so long as there is no commensurate increase in aggregate volume.

Transition from one phase to another may be triggered by the need to forage or mate or in response to external threats. However, the process by which this transition occurs is not well understood. Animal aggregations provide many examples of phase transitions which are analogous to those found in fluids. For example, the formation and dissolution of locust swarms is analogous to vapor condensing into liquid and evaporating back to vapor. Though several studies have examined locusts in their natural environment [169, 170, 171], field experiments with locust swarms are difficult because of the immense size of their aggregations. For example, a single *Locusta migratoria* swarm may spread across 100 km^2, exceed 10^{10} members, and its center of mass may travel up to 100 km a day [162, 163, 166]. Thus an understanding of locust swarm formation has begun to emerge from experiments performed in laboratory settings with the insects tethered or enclosed in a small arena. Swarming develops as individuals cluster ($O(10)$ members), growing to form terrestrial 'marching bands' that collect additional members as they travel [172, 163]. Locust movement in bands is accompanied by an increase in O_P as solitary locusts congregate and display net migration. Locust nymphs, juvenile and flightless, utilize cannibalization when forming marching bands to establish and maintain collective movement [165, 173]. When members get too close, they bite one another, which in turn promotes motion. Adult marching bands take to the air at a critical mass which is subject to wind, temperature, and sunlight, a complex relationship which is not well-understood [163, 174, 175]. The process of locust aggregation and transition to flight is comparable to the formation of raindrops, as low O_P vapor molecules nucleate onto water-insoluble particles in the atmosphere [176] during phase change. At a critical size, the droplet falls

and continues to collect vapor molecules during its travel. Yet another analogy is the flocculation and subsequent settling of suspended bacteria [177].

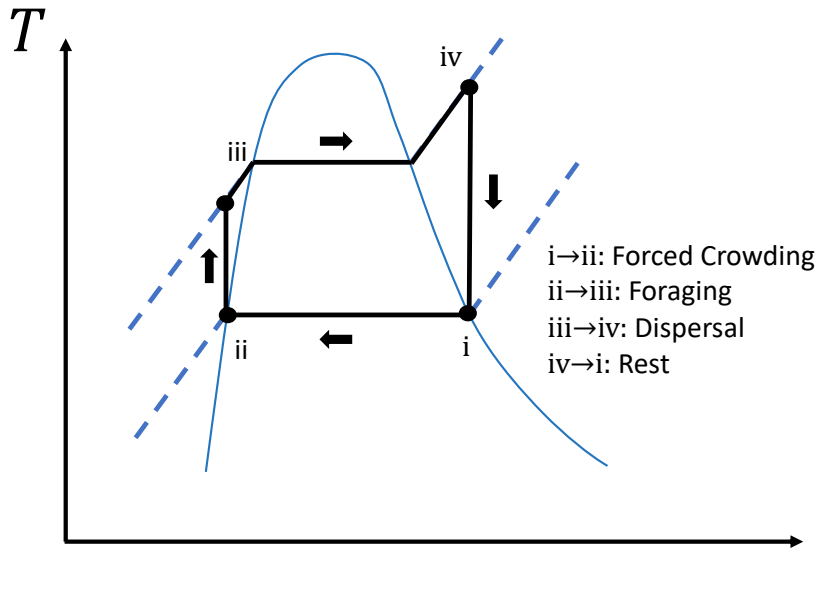

Figure A.3: Temperature (T) vs. specific volume (v) diagram relating locust phase change to phase change in a typical two-phase working fluid.

Schistocerca gregaria locusts likewise provide an analogue of phase transitions in fluids. These insects have two phases, a gregarious (liquid) and solitary (vapor) phase, each of which is associated with changes in behavior [174, 178]. To illustrate the resemblance to fluidic phase transition, we employ a generic temperature-specific volume (T-v) diagram in Figure A.3. A rise in in temperature and pressure corresponds to increases in internal energy, and increases in specific volume denote reduction in locust aggregate density. The cyclic nature of swarm formation and disbandment begins at (i), a saturated vapor, the point where solitary locusts are poised to assemble. Accompanying such a phase change is a decrease in internal energy, i.e. depleted levels of stored food energy. In a vapor, a drop in energy reduces molecular motion, resulting in a phase transition, with accompanying organization and cohesion (liquid). Forced crowding, which raises insects' serotonin levels, occurs as the insects transition from phase (i) to (ii). Serotonin is pro-

duced as a result of tactile, visual, and olfactory detection of other locusts. Within approximately 2 hr of forced crowding [178, 166] the serotonin levels increase sufficiently to elicit full transition to the gregarious phase, state (ii). Foraging commences at (ii) and continues to (iii) as the cohesive swarm [162] rolls through thousands of acres increasing internal energy (stored food energy), temperature, and pressure, until the locusts are satiated at (iii). Next, the swarm dissolves as members leave the group and transition back to a solitary state, from (iii) to (iv). From (iv) to (i), the locusts expend energy to the point where internal energy drops sufficiently to drive the cycle again.

Changes in phase also may be tied to changes in the behavior of organisms within an aggregation. For example, crowd density heavily influences individual human behavior [179]. A crowd of pedestrians can be treated as a continuum so long as the typical distance between members is much less than the characteristic length scale of the space in which they are moving [179, 180]. At sufficient velocities, humans exhibit flow separation around flow obstacles [180]. Crowds are approximately locally homogeneous, forming body-centric square patterns with high degrees of polarity [181]. In the 1990s, studies of crowd motion abandoned the use of Navier-Stokes equations and derived equations which merge unsteady continuity and social theories, including functions for walking speed and discomfort as a function of density [179, 180]. These nonlinear partial differential equations are amenable to an analytic solution and are applicable to unsteady flows. Furthermore, they result in two flow regimes, subcritical (tranquil) and supercritical (rapid) flow, defined by wave-like motion that can appear in the flow, similar to highway patterns [182]. Thus, crowds maintain a strong parallel to open channel flow [183, 184]. At very high crowd densities, the equations of motion resemble two-dimensional Navier-Stokes equations with Newtonian friction replaced by Rayleigh-like friction, and generally neglect advective terms.

A.1.2 Viscosity

Viscosity is the resistance of a fluid to deformation in response to an externally applied shear stress. A fluid's viscosity allows neighboring fluid particles to influence one another through this shear stress. Here, we highlight how members of aggregations 'shear' one another, through physical contact, or social pressures and interactions between neighbors. Near-neighbor interactions give aggregations form and responsiveness, and allow boundary conditions to impact the behavior of the entire group. Clumps of *Solenopsis invicta* ants provide such an example. Researchers measured the continuum property of viscosity of ant clusters by considering ants as molecules and subjecting the clusters to rheometry tests. The viscosity of ant groups was measured as $\sim 10^6$ cP by allowing a sphere to settle into a beaker of ants, as a sphere might sink into a viscous fluid [167], with a corresponding shear rate of $\dot{\gamma} = 1.9 \times 10^{-3}$ s^{-1}. In a plate-plate rheometer, the stress required to maintain the imposed ant flow was approximately constant at 70 Pa for $\dot{\gamma} = 10^{-3}$ s^{-1} to 10^{1} s^{-1}. Thus, the ant aggregations shear thin dramatically with increasing shear rate. Experiments with live and dead ants produce identical values of viscosity, indicating that ants become passive when forced to flow. Live ants subjected to a constant stress creep and maintain constant strain rates. A ball of ants, for example, placed on water surface, slumps to form a flattened raft, much like when a drop of viscous fluid spreads on a solid surface [2], behaving as a porous material [2, 185, 186] with density of ≈ 0.2 g/mL. Under oscillatory strain, ant aggregations are viscoelastic, able to store and dissipate energy, similar to colloidal gels of Brownian particles in a solvent [167]. The possibility of viscoelastic behavior in aggregations of animals which flow in response to external perturbations but are unable to link together does not seem to have been explored.

In organismal aggregations which do not physically link with each other, such as flocks of birds and schools of fish, viscosity may be analogous to social forces. For example, humans in crowds do not enjoy being in contact with one another. As crowd density increases, motion slows as if the

crowd's viscosity increases, strengthening the friction as individuals slide past one another [187]. Rates of passage though halls and doors drop dramatically if this viscous nature is not controlled [188]. A particularly high profile example is the fatal 2015 Mina stampede that occurred on the Jamaraat Bridge in Saudi Arabia, a result of critically high crowd congestion [189]. This disaster followed a similar incident [190] and bridge redesign in 2004. Surprisingly, placing a barrier in a flow of pedestrians at a building exit can decrease the travel time of all those exiting by preventing jamming at the door threshold and increase flow rate through the exit [188]. This phenomenon, known as Braess' paradox, can perhaps be extended to preventing clogs of particle-laden flows with high Bagnold numbers [191], $\mathrm{Ba} = \rho_\mathrm{p} d^2 \lambda^{1/2} \dot{\gamma}/\mu$, where ρ_d is the particle density, d is the particle diameter, λ is the linear particle concentration, and μ is the interstitial fluid viscosity. Such an extension to particle-laden flow jamming has not been explored in the literature to the authors knowledge. Herds of sheep and cattle also likely experience a type of viscosity as they flow through a gate into a pen or along a fence. This viscosity seems to be a result of closely packed (e.g. congested) neighbors interfering with their neighbors ability to locomote freely.

A.1.3 Surface tension

Surface tension refers to the propensity of liquids to behave elastically at a liquid-air interface and arises from intermolecular attraction. A liquid is more attracted to itself than the surrounding gas. Surface tension enables droplet cohesion and the ability to reform shape after perturbation. The same can be said for organismal aggregations such as schools, flocks, and clumps of ants that have coherent boundaries and maintain structure throughout aggregate motion. Individuals within these groups are similarly more attracted to their neighbors than to the surrounding void. This attraction may comprise physical links or a social force between conspecifics. These groups thus have the ability to self-heal and reform in response to environmental perturbations and threats. The aggregative social dynamics which cohere animal groups through a surface tension-like force

have long been used to model the collective movement of animal groups. The Boids model, for example, successfully recreated realistic flocking behavior by requiring members steer to avoid crowding nearby conspecifics, steer so as to align with nearby conspecific, and steer towards the center of mass of the aggregation [192]. This last rule is a useful analogue of surface tension as it provides an inward pull towards the group center.

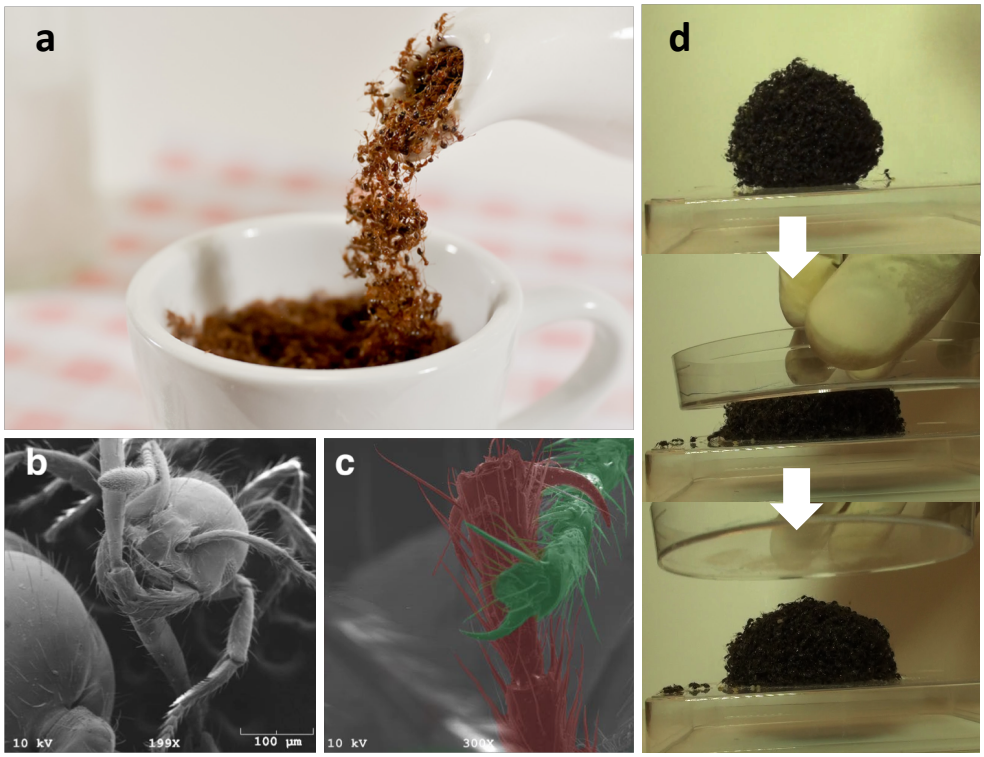

Figure A.4: **(a)** Ants pouring from a teapot, and SEM images of ant-to-ant linkages **(b)** with mandible-tarsus [2], and **(c)** tarsus-tarsus linking [2], and **(d)** a cluster of ants being compressed between two parallel plates and regaining form when compression is released. Photo credits: Nathan Mlot & David Hu, Georgia Institute of Technology.

Ants are well known for their ability to collectively accomplish tasks ranging from foraging to tunneling to construction [2, 193, 194, 168, 167]. The method by which ants build bridges [195] and floating rafts [2], by grappling onto nearest neighbors [193], is particularly pertinent to this review as it illustrates how organismal aggregations can resist external forces and maintain shape. While individual ants do not behave like fluid molecules and while the interactions between ants

grappling onto one another are quite different from molecular interactions, the contiguous mass created by this behavior exhibits surface tension-like properties. Grappling ant groups will, for example, drip from a downward hanging point like water droplets dripping or flow from a leaky faucet [186, 185], like that seen in Figure A.4**a**. When shaken about in a beaker, ants readily grapple together and form a ball which may be stretched and pulled apart by hand [2]. The strength of the 'ant-fluid' material is a function of the number of grappling connections ants make with neighbors and the length of those linkages [193], as seen in Figure A.4**b,c**. On average, an ant connects at 6 points to its neighbors and is connected to 4.8 different neighbors. If a ball of ants is briefly compressed between two plates, they will spring back to nearly its original shape once the external force is removed [167], as seen in Figure A.4**d**. This repeatable behavior corresponds to how a water droplet behaves when compressed between two superhydrophobic surfaces. Researchers estimated the surface tension of a cluster, $\sigma = F/\delta \sim 10^3$ dyn/cm by measuring ant grappling force F and spacing δ, and found a value that is 10 times the surface tension of water for a raft that is one-fifth the density of water [2]. The resulting capillary length for ants is 3 cm. A fluid with such properties would have a droplet spreading time of 10^3 seconds, nearly an order of magnitude greater than the spreading time of an ant raft. The tendency of some prey fish species, such as herring (Figure 5.1k,l) to form into cohesive balls [196], large spherical aggregations on which dolphins, orcas [197, 198], and seabirds feed, also reveals an aggregative social force analogous to the surface tension which pulls a small water droplet into a spherical shape [199].

Stationary midge swarms by *Dasyhelea flavifrons*, *Corynoneura scutellata*, and *Cladotanytarsus atridorsum* provide surface tension-like behavior, but are in stark contrast to ants, as members do not grapple one another. Instead, social forces provide the attraction needed to keep a cohesive aggregation. Midge swarms are comprised primarily of males and seek to attract females for reproduction [200, 201, 202]. The swarms have a zero mean velocity [203] and assemble at landmarks [204]. They take the shape of columns which are generally 2-m above ground, range from $1-5$

m in height, and are comprised of approximately 10^2 - 10^4 members [205]. It has been shown that midges influence each other's motion far beyond their nearest neighbors [200]. Member attraction to the center of the swarm enables cohesion [200, 203], and is a result of non-polar alignment with one another. Non-polarizing behavior is comparable to freely moving particles which rebound at the surface to reorient for ballistic flight toward the center [203]. Within the swarm, midges fly in a zig-zag pattern both horizontally and vertically [206] and experience $3-4\ g$ when changing direction at the swarm surface, where acceleration is highest [207, 203]. Acceleration is zero as midges pass through the center. Maximum speed in laboratory conditions was found [207] to be around 1.1 m/s, corresponding to a Reynolds number range of $\mathrm{Re} = 240-280$.

A.2 Summary

In this Chapter we review collective motion to detail how documented aggregate behavior displays fluidic properties. We propose that locust migratory swarms from formation to separation behave as a working fluid on a traditional $T-v$ diagram transitioning from collective (liquid) to individual motion (vapor). We also detail how groups of fire ants display resistance to flow (viscosity) and elastic behavior while maintaining self attraction through linkages (surface tension). We detail how human motion in groups also display viscosity, as density of crowding increased the ability for like particles to flow past one another decreased as such as with highly viscous fluids.

APPENDIX B: PUBLICATIONS AND PRESENTATIONS

Journal papers

Smith, N. M., Ebrahimi, H., Ghosh, R., & Dickerson, A. K. (2018). High-speed microjets issue from bursting oil gland reservoirs of citrus fruit. Proceedings of the National Academy of Sciences, 115(26), E5887-E5895.

Smith, N. M., Clayton, G. V., Khan, H. A., & Dickerson, A. K. (2018). Mosquitoes modulate leg dynamics at takeoff to accommodate surface roughness. Bioinspiration & Biomimetics, 14(1), 016007.

Smith, N. M., Dickerson, A. K., & Murphy, D. (2019). Organismal aggregations exhibit fluidic behaviors: a review. Bioinspiration & Biomimetics, 14(3), 031001.

Smith, N. M., Dickerson, A. K., & Balsalobre, J. (Submitted). Landing mosquitoes bounce when engaging a substrate.

Conference presentations

Smith, N.M. and Ghosh, R. and Dickerson, A.K. “Citrus Jets" Society for Integrative and Comparative Biology. Jan 2017. New Orleans, LA

Smith, N.M. and, Ghosh, R. and Dickerson, A.K. “Microjets of citrus fruits" American Physical Society: Division of Fluid Dynamics. Nov 2017. Denver, Colorado

Smith, N.M. and Clayton, G. and Dickerson, A.K. “Mosquitoes modulate takeoff to accomadate surface irregularities" Society for Integrative and Comparative Biology. Jan 2018. San Francisco, CA

Smith, N.M. and Balsalobre, J. and Dickerson, A.K. “Mosquitoes utilize multples bounces to engage landing substrates " Society for Integrative and Comparative Biology. Jan 2020. Austin, TX

APPENDIX C: ADDITIONAL VIDEOS AND FIGURES

C.1 Mosquito Takeoffs

C.1.1 Supplementary Movie Captions

Movie S1: Video of a female *Aedes aegypti* mosquito utilizing a leg-strike takeoff, slowed 33x.
https://youtu.be/cVOF19JkTNY

Movie S2: Video of a female *Aedes aegypti* mosquito utilizing a push takeoff, slowed 133x.
https://youtu.be/erTRIi5kUMM

Movie S3: Video of a female *Aedes aegypti* mosquito utilizing a push takeoff on a polished acrylic surface with tarsi slipping during pushing action, slowed 133x.
https://youtu.be/sOsMBITdmks

C.2 Mosquito Landings

C.2.1 Supplementary movie captions

Movie S1: A female *Ae. aegypti* mosquito landing on a purple substrate with negligible tangential velocity and experiencing minor proboscis deformation. Tarsi do not leave the substrate following first contact, resulting in a single bounce. Slowed 133x.
https://youtu.be/0iZbOvcpRfE

Movie S2: A female *Ae. aegypti* mosquito landing on a purple substrate with significant tangential velocity, body rotation, and large proboscis deformation. Tarsi leave the substrate after initial contact, resulting in two bounces. Slowed 133x.

https://youtu.be/_2h5hdSpxRY

Movie S3: A female *Ae. aegypti* mosquito landing on a purple substrate with large proboscis deformation and collapse. Slowed 133x.

https://youtu.be/kRa9rHNQCm4

C.2.2 Supplementary figures and table

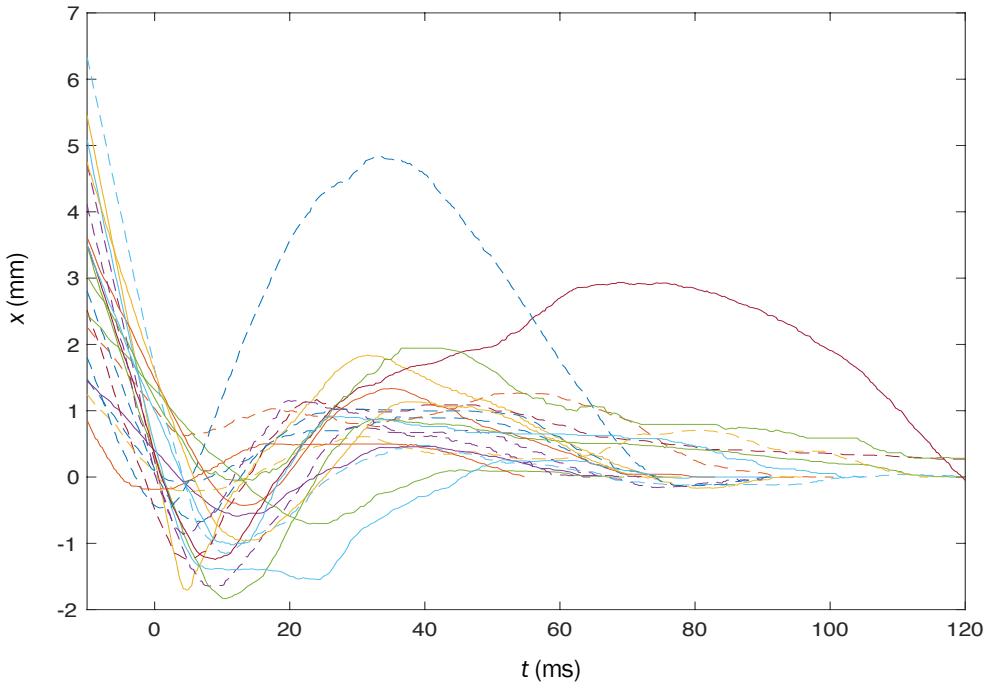

Figure C.1: Normal-to-substrate displacement for all 20 analyzed landings without smoothing. The tracked point on the mosquito is the interface of the proboscis with the head. The final resting position the tracked point corresponds to $x = 0$. First contact of any portion of the mosquito with the landing surface corresponds to $t = 0$. Dashed-curves indicate the proboscis is the first member to contact the substrate, while solid lines indicate tarsi initiate contact.

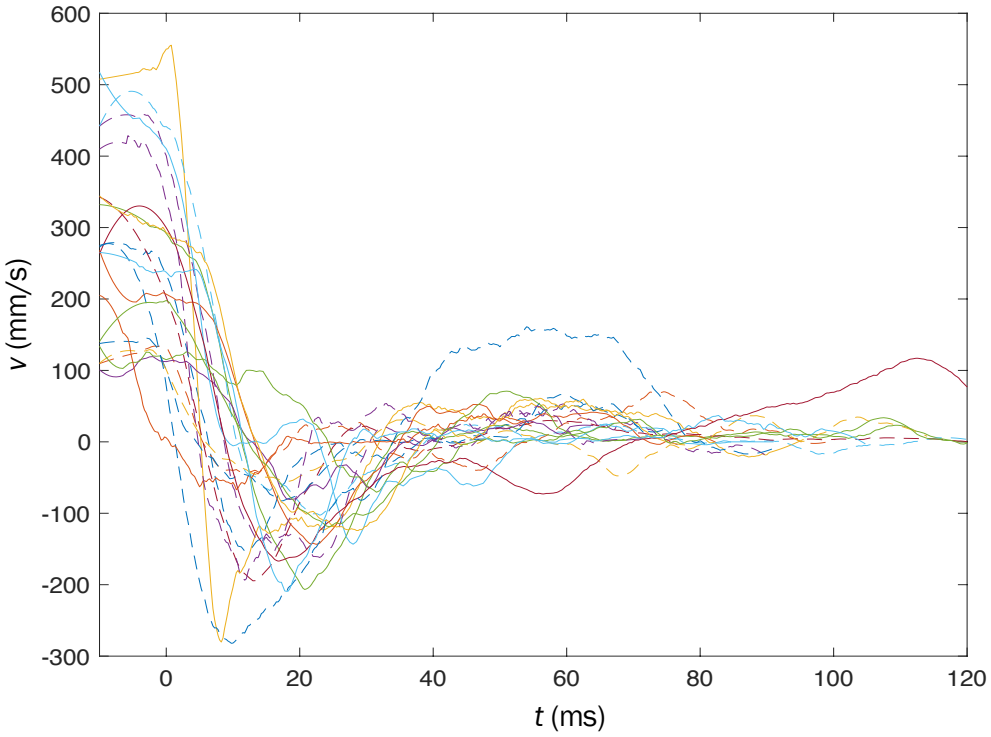

Figure C.2: Normal-to-substrate velocity for all 20 analyzed landings. The tracked point on the mosquito is the interface of the proboscis with the head. First contact of any portion of the mosquito with the landing surface corresponds to $t = 0$. Dashed-curves indicate the proboscis is the first member to contact the substrate, while solid lines indicate tarsi initiate contact. Curves are smoothed with a Savitzky-Golay filter at 10% span.

Table C.1: Free vibration properties of mosquitoes measured following the impulsive cession of a vibrating floor at 25 and 50 Hz.

	25 Hz (N = 4)	50 Hz (N = 4)
ζ	0.44 ± 0.03	0.28 ± 0.06
k (N/m)	0.118	0.103
c (N-s/m)	3.9×10^{-4}	2.3×10^{-4}

C.3 Citrus Jets

C.3.1 Citrus jet instability

Free jets issuing from circular orifices experience capillary instability and break up even when orifices are perfectly circular, the fluid is inviscid, and flow is laminar [208]. Previous studies

show that jet stability is influenced by inlet conditions and orifice geometry [209, 210, 211], and that asymmetric jets are less stable, encouraging breakup. The orifice geometry through which citrus jets issue is elliptical in nature, but shrouded by irregular edges of the torn flavedo. We measure 10 orifices and find they have an eccentricity range of $\varepsilon = \sqrt{1-b^2/a^2} = 0.33-0.99$, and hydraulic diameter of $D_h = 114$ μm on average. As witnessed with elliptical jets, the citrus oil exhibits major and minor axes switching (Movie S3), a consequence of initial perturbations in the jet imposed by eccentric orifices.

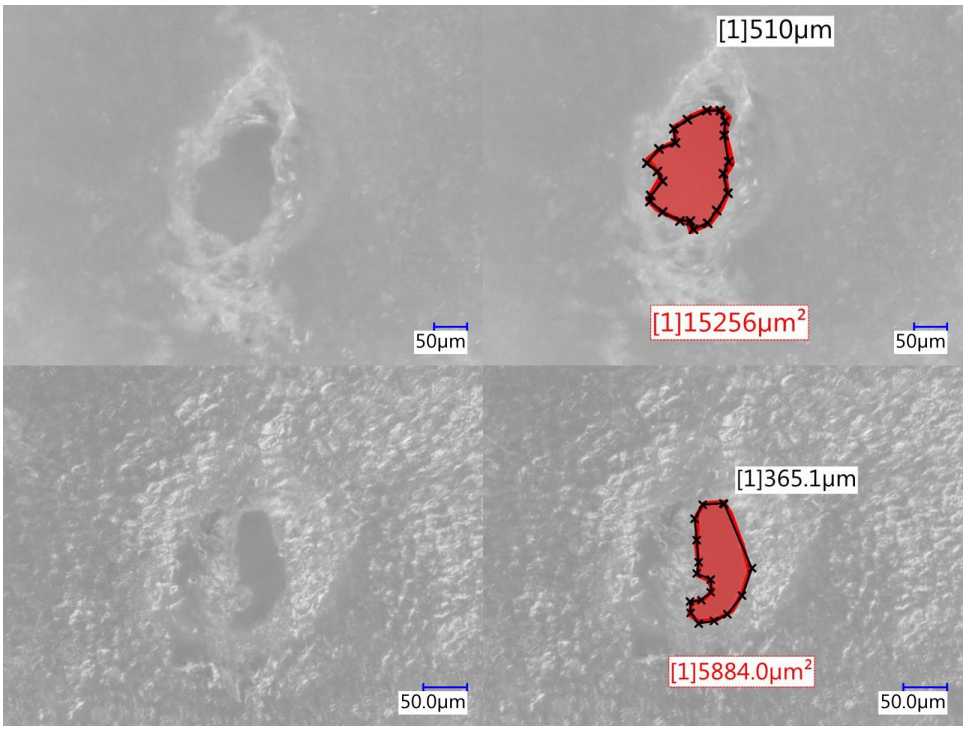

Figure C.3: Orifice shapes following two jetting events, with the orifice accentuated in red in the righthand panels.

Instability in citrus jets may be classified into two breakup regimes, driven by jet velocity V_0. The initial breakup regime of Rayleigh instability begins when the liquid Weber number $\mathrm{We} = \rho V_0^2 d_h/\gamma > 8$, resulting in $V_0 > 1.6$ m/s, also signaling the transition from dripping to jetting [212] (Movie S4). The end of the Rayleigh breakup regime occurs when $\mathrm{We} > 137$, corresponding to $V_0 > 6.6$ m/s, and triggering entrance into the first wind induced breakup regime. Citrus jets

regularly pass this issuance velocity resulting in unpredictable breakup distances. Another source of instability is the ragged office perimeters produced by the non-uniform tearing the citrus flavedo upon jet issuance, as seen in Fig.C.3. The longest breakup distances we observe from citrus peels approach 2 mm, far shorter than we were able to create artificially using orange oil shot through needles with $D_h = 160\ \mu$m (Movie S3).

C.3.2 Supplementary Movie Captions

Movie S1: Video sequence of oil jetting for all citrus species tested. (*Citrus sinensis* slowed 83x. *Citrus aurantifolia, Citrus paradisi, Citrus limon,* and *Citrus reticulata* slowed 133x.)
https://youtu.be/9Zm2VGQ1SAw

Movie S2: Cross-sectional view of Florida navel orange peel bending to the point of jetting. The albedo is compressed while the outer layer, or flavedo, experiences tension. (slowed 133x)
https://youtu.be/4vQjQ1hsfSk

Movie S3: Comparison of jet instability witnessed in natural (slowed 233x) and artificial (slowed 533x) orifices.
https://youtu.be/7VIwVjF47wU

Movie S4: An orange oil jet undergoing the transition from jetting to dripping. (slowed 266x)
https://youtu.be/eW9No75W-F8

C.3.3 Supplementary Figures

We include supplementary figures to support the assertion that oil gland size and fruit size are independent.

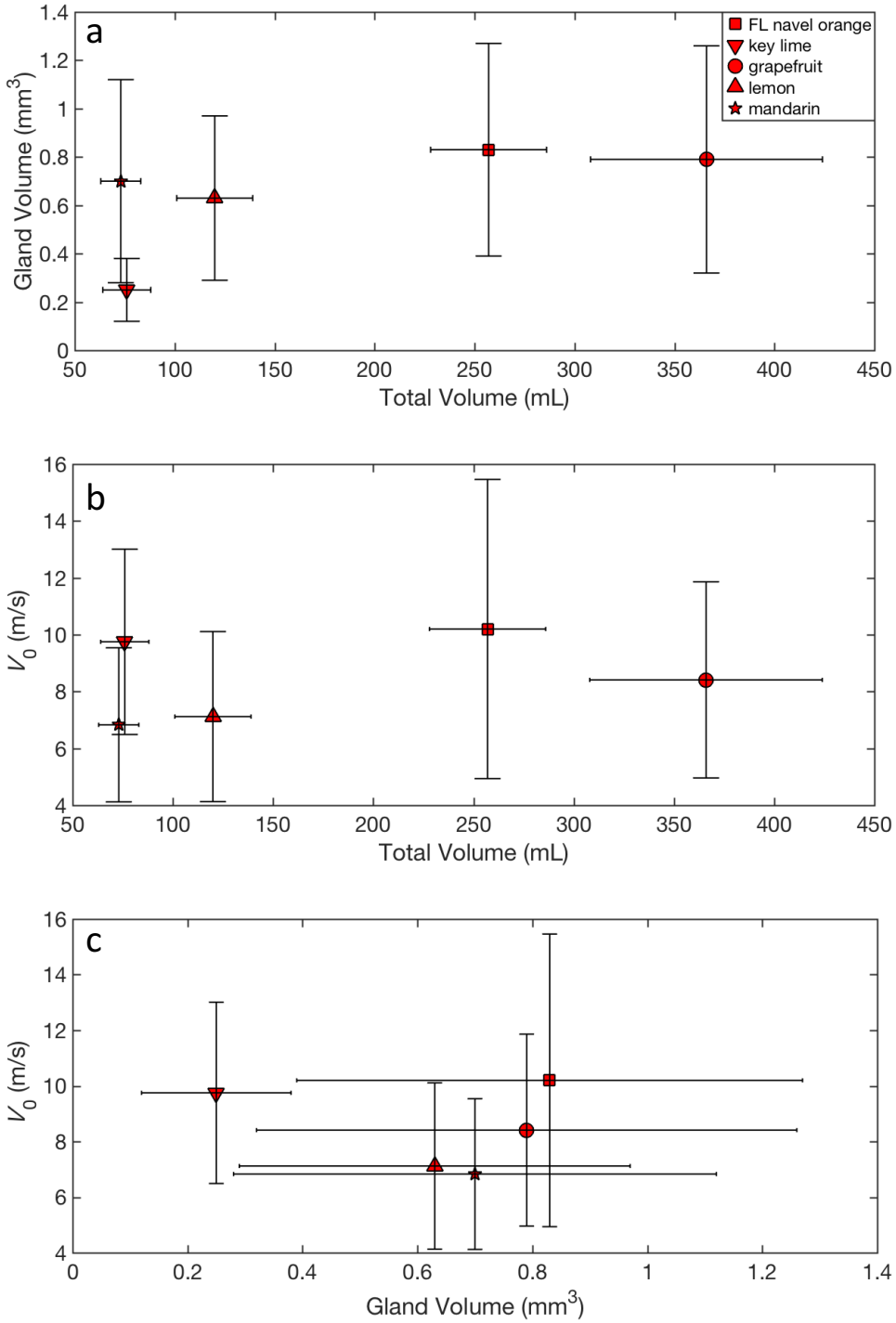

Figure C.4: **(a)** The relation between gland volume (N= 100 for each species) and bulk fruit volume (N= 30 for each species). **(b)** The relation between jet exit velocity (N= 100 for each species) and bulk fruit volume. **(c)** The relation between jet exit velocity and oil gland reservoir volume.

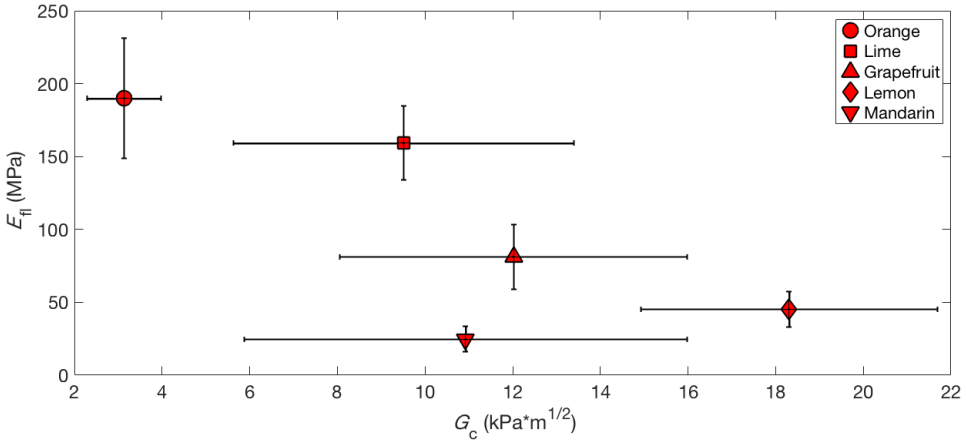

Figure C.5: The relation between flavedo stiffness E_{fl} (N= 5 for each species) and strain energy release rate G_{c} (N= 5 for each species).

LIST OF REFERENCES

[1] 2014. https://www.smithsonianmag.com/smart-news/scientists-use-twitter-pics-study-spiders-ants-and-birds-180970237/.

[2] Mlot, N. J., Tovey, C. A. & Hu, D. L., 2011 Fire ants self-assemble into waterproof rafts to survive floods. *Proceedings of the National Academy of Sciences* **108**, 7669–7673.

[3] Ballerini, M., Cabibbo, N., Candelier, R., Cavagna, A., Cisbani, E., Giardina, I., Orlandi, A., Parisi, G., Procaccini, A., Viale, M. *et al.*, 2008 Empirical investigation of starling flocks: a benchmark study in collective animal behaviour. *Animal behaviour* **76**, 201–215.

[4] Floreano, D. & Wood, R. J., 2015 Science, technology and the future of small autonomous drones. *Nature* **521**, 460–466.

[5] Wang, T., Si, Y., Li, N., Dong, Z. & Jiang, L., 2019 Bioinspired tip-guidance liquid jetting and droplet emission at a rotary disk via a surface energy gradient. *ACS nano* .

[6] BROOKS, R. & FLYNN, A., 1998 Fast, cheap and out of control: A robot invasion of the solar system. s. 478-485. *Journal of the British Interplanetary Society* **42**.

[7] Wood, R. J., 2008 The first takeoff of a biologically inspired at-scale robotic insect. *IEEE transactions on robotics* **24**, 341–347.

[8] Beard, R., Lee, D., Quigley, M., Thakoor, S. & Zornetzer, S., 2005 A new approach to future mars missions using bioinspired technology innovations. *Journal of Aerospace Computing, Information, and Communication* **2**, 65–91.

[9] Chahl, J., Thakoor, S., Le Bouffant, N., Stange, G., Srinivasan, M. V., Hine, B. & Zornetzer, S., 2003 Bioinspired engineering of exploration systems: a horizon sensor/attitude reference

system based on the dragonfly ocelli for mars exploration applications. *Journal of Robotic Systems* **20**, 35–42.

[10] Ristroph, L., Bergou, A. J., Guckenheimer, J., Wang, Z. J. & Cohen, I., 2011 Paddling mode of forward flight in insects. *Physical review letters* **106**, 178103.

[11] Bomphrey, R. J., Nakata, T., Phillips, N. & Walker, S. M., 2017 Smart wing rotation and trailing-edge vortices enable high frequency mosquito flight. *Nature* **544**, 92.

[12] Young, J., Walker, S. M., Bomphrey, R. J., Taylor, G. K. & Thomas, A. L., 2009 Details of insect wing design and deformation enhance aerodynamic function and flight efficiency. *Science* **325**, 1549–1552.

[13] Wagner, H., 1982 Flow-field variables trigger landing in flies. *Nature* **297**, 147.

[14] Srinivasan, M. V., Zhang, S.-W., Chahl, J. S., Barth, E. & Venkatesh, S., 2000 How honeybees make grazing landings on flat surfaces. *Biological cybernetics* **83**, 171–183.

[15] Smith, N. M., Dickerson, A. K. & Murphy, D., 2019 Organismal aggregations exhibit fluidic behaviors: a review. *Bioinspiration & biomimetics* **14**, 031001.

[16] Furlani, E., 2004 Temporal instability of viscous liquid microjets with spatially varying surface tension. *Journal of Physics A: Mathematical and General* **38**, 263.

[17] Menezes, V., Kumar, S. & Takayama, K., 2009 Shock wave driven liquid microjets for drug delivery. *Physics of Fluids* **106**.

[18] Carter, J. C., Alvis, R. M., Brown, S. B., Langry, K. C., Wilson, T. S., McBride, M. T., Myrick, M., Cox, W. R., Grove, M. E. & Colston, B. W., 2006 Fabricating optical fiber imaging sensors using inkjet printing technology: A ph sensor proof-of-concept. *Biosensors and Bioelectronics* **21**, 1359–1364.

[19] Huffard, C. L., 2006 Locomotion by abdopus aculeatus (cephalopoda: Octopodidae): walking the line between primary and secondary defenses. *Journal of experimental biology* **209**, 3697–3707.

[20] Hibbitts, T. D. & Hibbitts, T. J., 2015 *Texas Lizards: A Field Guide*. University of Texas Press.

[21] Farahani, Y. F., Amin, G., Sardari, S. & Ostad, N., 2016 Effect of ecballium elaterium fruit on *Candida albicans*, *Aspergillus fumigatus* and *Escherchia coli*. *International Journal of Biological Research* **4**, 44–45.

[22] Dickerson, A., 2018 Citrus fruits inspire the next generation of airborne drug delivery. *ONdrugDelivery Magazine* pp. 30–34.

[23] Bode-Oke, A. T., Zeyghami, S. & Dong, H., 2017 Aerodynamics and flow features of a damselfly in takeoff flight. *Bioinspiration & Biomimetics* **12**, 056006.

[24] Chen, M. W., Zhang, Y. L. & Sun, M., 2013 Wing and body motion and aerodynamic and leg forces during take-off in droneflies. *Journal of the Royal Society Interface* **10**, 20130808.

[25] Sunada, S., Kawachi, K., Watanabe, I. & Azuma, A., 1993 Performance of a butterfly in take-off flight. *Journal of Experimental Biology* **183**, 249–277.

[26] Ellington, C., 1980 Wing mechanics and take-off preparation of thrips (thysanoptera). *Journal of Experimental Biology* **85**, 129–136.

[27] Pond, C. M., 1972 The initiation of flight in unrestrained locusts, schistocerca gregaria. *Journal of Comparative Physiology A: Neuroethology, Sensory, Neural, and Behavioral Physiology* **80**, 163–178.

[28] Muijres, F., Chang, S., vanVeen, W., Spitzen, J., Biemans, B., Koehl, M. & Dudley, R., 2017 Escaping blood-fed malaria mosquitoes minimize tactile detection without compromising on take-off speed. *Journal of Experimental Biology* **220**, 3751–3762.

[29] Trimarchi, J. & Schneiderman, A., 1995 Initiation of flight in the unrestrained fly, drosophila melanogaster. *Journal of Zoology* **235**, 211–222.

[30] Brooks, R. A. & Flynn, A. M., 1989 Fast, cheap and out of control. Technical report, Massachusetts Inst of Tech Cambridge Artificial Intelligence Lab.

[31] Card, G. & Dickinson, M., 2008 Performance trade-offs in the flight initiation of drosophila. *Journal of Experimental Biology* **211**, 341–353.

[32] Li, L., Rutlin, M., Abraira, V. E., Cassidy, C., Kus, L., Gong, S., Jankowski, M. P., Luo, W., Heintz, N., Koerber, H. R. *et al.*, 2011 The functional organization of cutaneous low-threshold mechanosensory neurons. *Cell* **147**, 1615–1627.

[33] Christophers, S. R., 1960 *Aedes aegypti: The yellow fever mosquito*. CUP Archive.

[34] Parker, J. E., Angarita-Jaimes, N., Abe, M., Towers, C. E., Towers, D. & McCall, P. J., 2015 Infrared video tracking of anopheles gambiae at insecticide-treated bed nets reveals rapid decisive impact after brief localised net contact. *Scientific reports* **5**, 13392.

[35] Srinivasan, M., Zhang, S., Lehrer, M. & Collett, T., 1996 Honeybee navigation en route to the goal: visual flight control and odometry. *Journal of Experimental Biology* **199**, 237–244.

[36] Cardé, R. T., Gibson, G. *et al.*, 2010 Host finding by female mosquitoes: mechanisms of orientation to host odours and other cues. *Olfaction in vector-host interactions* **2010**, 115–142.

[37] Altshuler, D. L. & Srinivasan, M. V., 2018 Comparison of visually guided flight in insects and birds. *Frontiers in neuroscience* **12**, 157.

[38] Danilovich, S., Krishnan, A., Lee, W.-J., Borrisov, I., Eitan, O., Kosa, G., Moss, C. F. & Yovel, Y., 2015 Bats regulate biosonar based on the availability of visual information. *Current Biology* **25**, R1124–R1125.

[39] Norberg, U. M. & Rayner, J. M., 1987 Ecological morphology and flight in bats (mammalia; chiroptera): wing adaptations, flight performance, foraging strategy and echolocation. *Philosophical Transactions of the Royal Society of London. B, Biological Sciences* **316**, 335–427.

[40] Dickerson, A. K., Olvera, A. & Luc, Y., 2018 Void entry by aedes aegypti (diptera: Culicidae) mosquitoes is lower than would be expected by a randomized search. *Journal of Insect Science* **18**, 9.

[41] Saraf, N., Villegas, M., Willenberg, B. J. & Seal, S., 2019 Multiplex viral detection platform based on a aptamers-integrated microfluidic channel. *ACS omega* **4**, 2234–2240.

[42] Parker, H. B., Beyer, G. E. & Pothier, O. L., 1903 Report of the working party i, yellow fever institute: a study of the etiology of yellow fever. *Yellow Fever Institute Bulletin* .

[43] Baird, E., Boeddeker, N., Ibbotson, M. R. & Srinivasan, M. V., 2013 A universal strategy for visually guided landing. *Proceedings of the National Academy of Sciences* **110**, 18686–18691.

[44] Hubel, D. H. & Wiesel, T. N., 1970 Stereoscopic vision in macaque monkey: cells sensitive to binocular depth in area 18 of the macaque monkey cortex. *Nature* **225**, 41–42.

[45] Nityananda, V., Tarawneh, G., Rosner, R., Nicolas, J., Crichton, S. & Read, J., 2016 Insect stereopsis demonstrated using a 3d insect cinema. *Scientific reports* **6**, 18718.

[46] Manzanera, R. J. & Smith, S., 2015 Flight in nature ii: How animal flyers land. *The Aeronautical Journal* **119**, 281–299.

[47] Jack, A., 1953 *Feathered wings: A study of the flight of birds*. Methuen.

[48] Lee, D. N., Davies, M. N., Green, P. R. *et al.*, 1993 Visual control of velocity of approach by pigeons when landing. *Journal of experimental biology* **180**, 85–104.

[49] Altenbach, J. S., 1979 Locomotor morphology of the vampire bat: Desmodus rotundus. Technical report.

[50] Horridge, G. A., 1977 Insects which turn and look. *Endeavour* **1**, 7–17.

[51] Srinivasan, M. V., 1992 Distance perception in insects. *Current Directions in Psychological Science* **1**, 22–26.

[52] Evangelista, C., Kraft, P., Dacke, M., Reinhard, J. & Srinivasan, M. V., 2010 The moment before touchdown: landing manoeuvres of the honeybee apis mellifera. *Journal of Experimental Biology* **213**, 262–270.

[53] Pfaff, M. & Varjú, D., 1991 Mechanisms of visual distance perception in the hawk moth macroglossum-stellatarum. *ZOOLOGISCHE JAHRBUCHER-ABTEILUNG FUR ALLGEMEINE ZOOLOGIE UND PHYSIOLOGIE DER TIERE* **95**, 315–321.

[54] Shen, C. & Sun, M., 2017 Wing and body kinematics measurement and force analyses of landing in fruit flies. *Bioinspiration & biomimetics* **13**, 016004.

[55] Yao, J. & Yeo, K., 2019 Free hovering of hummingbird hawkmoth and effects of wing mass and wing elevation. *Computers & Fluids* **186**, 99–127.

[56] Dickerson, A. K., Shankles, P. G., Madhavan, N. M. & Hu, D. L., 2012 Mosquitoes survive raindrop collisions by virtue of their low mass. *Proceedings of the National Academy of Sciences* **109**, 9822–9827.

[57] Sutcliffe, J. F., 1994 Sensory bases of attractancy: morphology of mosquito olfactory sensilla–a review. *Journal of the American Mosquito Control Association* **10**, 309.

[58] Peña Torres, J., Navarro Aranda, M., Parra Moreno, H. J. & Duque Luna, J. E., 2016 Design and construction of a trap for the surveillance of Aedes (Stegomyia) aegypti (Diptera: Culicidae). *Revista de la Universidad Industrial de Santander. Salud* **48**, 285–294. ISSN 0121-0807.

[59] Bernáth, B., Anstett, V. & Guerin, P. M., 2016 Anopheles gambiae females readily learn to associate complex visual cues with the quality of sugar sources. *Journal of Insect Physiology* **95**, 8–16. ISSN 0022-1910. (doi:http://dx.doi.org/10.1016/j.jinsphys.2016.08.011).

[60] Hoel, D. F., Obenauer, P. J., Clark, M., Smith, R., Hughes, T. H., Larson, R. T., Diclaro, J. W. & Allan, S. A., 2011 Efficacy of ovitrap colors and patterns for attracting aedes albopictus at suburban field sites in north-central florida. *Journal of the American Mosquito Control Association* **27**, 245–251. (doi:10.2987/11-6121.1).

[61] Gilbert, I., Gouck, H. *et al.*, 1957 Influence of surface color on mosquito landing rates. *Journal of Economic Entomology* **50**.

[62] Prestwich, G., 1984 Defense mechanisms of termites. *Annual Review of Entomology* **29**, 201–232.

[63] de Mello, A. P., Azevedo, N. R., da Silva, A. M. B. & Gusmão, M. A. B., 2016 Chemical composition and variability of the defensive secretion in nasutitermes corniger (Motschulsky, 1885) in urban area in the brazilian semiarid region. *Entomotropica* **31**, 82–90.

[64] Suter, R. B. & Stratton, G. E., 2013 Predation by spitting spiders: elaborate venom gland, intricate delivery system. In *Spider Ecophysiology*, pp. 241–251. Springer.

[65] Yang, P. J., Pham, J., Choo, J. & Hu, D. L., 2014 Duration of urination does not change with body size. *Proceedings of the National Academy of Sciences* **111**, 11932–11937.

[66] Triep, M., Hess, D., Chaves, H., Brücker, C., Balmert, A., Westhoff, G. & Bleckmann, H., 2013 3D flow in the venom channel of a spitting cobra: do the ridges in the fangs act as fluid guide vanes? *PloS One* **8**, e61548.

[67] Velasco, R. & Licciardello, C., 2014 A genealogy of the citrus family: clarification of the genetic relationships among species opens new possibilities for enhancing citrus diversity and disease resistance. *Nature Biotechnology* **32**, 640–643.

[68] Maffei, M. E., Gertsch, J. & Appendino, G., 2011 Plant volatiles: production, function and pharmacology. *Natural Product Reports* **28**, 1359–1380.

[69] Koul, O., Walia, S. & Dhaliwal, G., 2008 Essential oils as green pesticides: potential and constraints. *Biopesticides International* **4**, 63–84.

[70] Nannapaneni, R., Muthaiyan, A., Crandall, P. G., Johnson, M. G., O'Bryan, C. A., Chalova, V. I., Callaway, T. R., Carroll, J. A., Arthington, J. D., Nisbet, D. J. *et al.*, 2008 Antimicrobial activity of commercial citrus-based natural extracts against *Escherichia coli* O157: H7 isolates and mutant strains. *Foodborne Pathogens and Disease* **5**, 695–699.

[71] Weldon, P. J., Carroll, J. F., Kramer, M., Bedoukian, R. H., Coleman, R. E. & Bernier, U. R., 2011 Anointing chemicals and hematophagous arthropods: responses by ticks and mosquitoes to *Citrus* (Rutceae) peel exudates and monoterpene components. *Journal of Chemical Ecology* **37**, 348–359.

[72] Underhill, S. J., McLauchlan, R. L., Dahler, J. M. & Bertram, J., 1998 Flavedo and albedo changes in 'Eureka' lemons caused by static compression and impact loading. *Journal of Texture Studies* **29**, 437–452.

[73] Kirbaşlar, F. G., Tavman, A., Dülger, B. & Türker, G., 2009 Antimicrobial activity of turkish citrus peel oils. *Pakistan Journal of Botany* **41**, 3207–12.

[74] Knight, T. G., Klieber, A. & Sedgley, M., 2002 Structural basis of the rind disorder oleocellosis in washington navel orange (*Citrus sinensis L. Osbeck*). *Annals of Botany* **90**, 765–773.

[75] Matura, M., Goossens, A., Bordalo, O., Garcia-Bravo, B., Magnussona, K., Wrangsjö, K. & Karlberg, A.-T., 2002 Oxidized citrus oil (r-limonene): a frequent skin sensitizer in Europe. *Journal of the American Academy of Dermatology* **47**, 709–714.

[76] Fisher, K. & Phillips, C., 2008 Potential antimicrobial uses of essential oils in food: is citrus the answer? *Trends in Food Science & Technology* **19**, 156–164.

[77] Nazaroff, W. W. & Weschler, C. J., 2004 Cleaning products and air fresheners: exposure to primary and secondary air pollutants. *Atmospheric Environment* **38**, 2841–2865.

[78] Ladanyia, M. & Ladaniya, M., 2010 *Citrus fruit: biology, technology and evaluation*. Academic Press.

[79] Ben-Yehoshua, S., Burg, S. P. & Young, R., 1985 Resistance of citrus fruit to mass transport of water vapor and other gases. *Plant Physiology* **79**, 1048–1053.

[80] Bennici, A. & Tani, C., 2004 Anatomical and ultrastructural study of the secretory cavity development ofcitrus sinensis and citrus limon: evaluation of schizolysigenous ontogeny. *Flora-Morphology, Distribution, Functional Ecology of Plants* **199**, 464–475.

[81] Smith, N. M., Ebrahimi, H., Ghosh, R. & Dickerson, A. K., 2018 High-speed microjets issue from bursting oil gland reservoirs of citrus fruit. *Proceedings of the National Academy of Sciences* **115**, E5887–E5895.

[82] Smith, N. M., Clayton, G. V., Khan, H. A. & Dickerson, A. K., 2018 Mosquitoes modulate leg dynamics at takeoff to accommodate surface roughness. *Bioinspiration & biomimetics* **14**, 016007.

[83] Hedrick, T. L., 2008 Software techniques for two-and three-dimensional kinematic measurements of biological and biomimetic systems. *Bioinspiration & biomimetics* **3**, 034001.

[84] Parry, D. & Brown, R., 1959 The jumping mechanism of salticid spiders. *Journal of Experimental Biology* **36**, 654–664.

[85] Burrows, M. & Sutton, G., 2008 The effect of leg length on jumping performance of short- and long-legged leafhopper insects. *Journal of Experimental Biology* **211**, 1317–1325.

[86] Sutton, G. P. & Burrows, M., 2008 The mechanics of elevation control in locust jumping. *Journal of Comparative Physiology A* **194**, 557–563.

[87] Sutton, G. & Burrows, M., 2010 The mechanics of azimuth control in jumping by froghopper insects. *Journal of Experimental Biology* **213**, 1406–1416.

[88] Suratwala, T., Steele, W., Feit, M., Shen, N., Dylla-Spears, R., Wong, L., Miller, P., Desjardin, R. & Elhadj, S., 2016 Mechanism and simulation of removal rate and surface roughness during optical polishing of glasses. *Journal of the American Ceramic Society* **99**, 1974–1984.

[89] Tchvialeva, L., Zeng, H., Markhvida, I., McLean, D. I., Lui, H. & Lee, T. K., 2010 Skin roughness assessment. In *New Developments in Biomedical Engineering*. InTech.

[90] Wu, C., Kong, X. & Wu, D., 2007 Micronanostructures of the scales on a mosquito's legs and their role in weight support. *Physical Review E* **76**, 017301.

[91] Zhang, J., Song, G., Li, Y., Qiao, G., Song, A. & Wang, A., 2013 A bio-inspired jumping robot: Modeling, simulation, design, and experimental results. *Mechatronics* **23**, 1123–1140.

[92] Tolley, M. T., Shepherd, R. F., Karpelson, M., Bartlett, N. W., Galloway, K. C., Wehner, M., Nunes, R., Whitesides, G. M. & Wood, R. J., 2014 An untethered jumping soft robot. In *Intelligent Robots and Systems (IROS 2014), 2014 IEEE/RSJ International Conference on*, pp. 561–566. IEEE.

[93] Zhao, J., Xu, J., Gao, B., Xi, N., Cintron, F. J., Mutka, M. W. & Xiao, L., 2013 Msu jumper: A single-motor-actuated miniature steerable jumping robot. *IEEE Transactions on Robotics* **29**, 602–614.

[94] Aoyama, H., Himoto, A., Fuchiwaki, O., Misaki, D. & Sumrall, T., 2005 Micro hopping robot with ir sensor for disaster survivor detection. In *Safety, Security and Rescue Robotics, Workshop, 2005 IEEE International*, pp. 189–194. IEEE.

[95] Kovac, M., Fuchs, M., Guignard, A., Zufferey, J.-C. & Floreano, D., 2008 A miniature 7g jumping robot. In *Robotics and Automation, 2008. ICRA 2008. IEEE International Conference on*, pp. 373–378. IEEE.

[96] Noh, M., Kim, S.-W., An, S., Koh, J.-S. & Cho, K.-J., 2012 Flea-inspired catapult mechanism for miniature jumping robots. *IEEE Transactions on Robotics* **28**, 1007–1018.

[97] Kikuchi, F., Ota, Y. & Hirose, S., 2003 Basic performance experiments for jumping quadruped. In *Intelligent Robots and Systems, 2003.(IROS 2003). Proceedings. 2003 IEEE/RSJ International Conference on*, volume 4, pp. 3378–3383. IEEE.

[98] Armour, R., Paskins, K., Bowyer, A., Vincent, J. & Megill, W., 2007 Jumping robots: a biomimetic solution to locomotion across rough terrain. *Bioinspiration & biomimetics* **2**, S65.

[99] Fiorini, P., Hayati, S., Heverly, M. & Gensler, J., 1999 A hopping robot for planetary exploration .

[100] Howe, S. D., O'Brien, R. C., Ambrosi, R. M., Gross, B., Katalenich, J., Sailer, L., Webb, J., McKay, M., Bridges, J. C. & Bannister, N. P., 2011 The mars hopper: an impulse-driven, long-range, long-lived mobile platform utilizing in situ martian resources. *Proceedings of the Institution of Mechanical Engineers, Part G: Journal of Aerospace Engineering* **225**, 144–153.

[101] Montminy, S., Dupuis, E. & Champliaud, H., 2008 Mechanical design of a hopper robot for planetary exploration using sma as a unique source of power. *Acta Astronautica* **62**, 438–452.

[102] Yoshimitsu, T., Kubota, T., Nakatani, I., Adachi, T. & Saito, H., 2003 Micro-hopping robot for asteroid exploration. *Acta Astronautica* **52**, 441–446.

[103] Ackerman, E., 2012 Boston dynamics sand flea robot demonstrates astonishing jumping skills. *IEEE Spectrum Robotics Blog* **2**.

[104] Sutton, G. P. & Burrows, M., 2011 Biomechanics of jumping in the flea. *Journal of Experimental Biology* **214**, 836–847.

[105] Bennet-Clark, H. & Lucey, E., 1967 The jump of the flea: a study of the energetics and a model of the mechanism. *Journal of Experimental Biology* **47**, 59–76.

[106] Burrows, M., 2007 Anatomy of the hind legs and actions of their muscles during jumping in leafhopper insects. *Journal of Experimental Biology* **210**, 3590–3600.

[107] Josephson, R., 1993 Contraction dynamics and power output of skeletal muscle. *Annual review of physiology* **55**, 527–546.

[108] Bleischwitz, R., de Kat, R. & Ganapathisubramani, B., 2016 Aeromechanics of membrane and rigid wings in and out of ground-effect at moderate reynolds numbers. *Journal of Fluids and Structures* **62**, 318 – 331. ISSN 0889-9746. (doi:https://doi.org/10.1016/j.jfluidstructs.2016.02.005).

[109] Bomphrey, R. J., Nakata, T., Phillips, N. & Walker, S. M., 2017 Smart wing rotation and trailing-edge vortices enable high frequency mosquito flight. *Nature* **544**, 92–95. ISSN 0028-0836.

[110] Nakata, T., Phillips, N., Simões, P., Russell, I. J., Cheney, J. A., Walker, S. M. & Bomphrey, R. J., 2020 Aerodynamic imaging by mosquitoes inspires a surface detector for autonomous flying vehicles. *Science* **368**, 634–637.

[111] Xiong, J., Ghosh, R., Ma, L., Ebrahimi, H., Hamouda, A., Vaziri, A. & Wu, L., 2014 Bending behavior of lightweight sandwich-walled shells with pyramidal truss cores. *Composite Structures* **116**, 793–804.

[112] Xiong, J., Ghosh, R., Ma, L., Vaziri, A., Wang, Y. & Wu, L., 2014 Sandwich-walled cylindrical shells with lightweight metallic lattice truss cores and carbon fiber-reinforced composite face sheets. *Composites Part A: Applied Science and Manufacturing* **56**, 226–238.

[113] Vinauger, C., Lutz, E. K. & Riffell, J. A., 2014 Olfactory learning and memory in the disease vector mosquito aedes aegypti. *Journal of Experimental Biology* **217**, 2321–2330.

[114] Dekker, T. & Cardé, R. T., 2011 Moment-to-moment flight manoeuvres of the female yellow fever mosquito (aedes aegypti l.) in response to plumes of carbon dioxide and human skin odour. *Journal of Experimental Biology* **214**, 3480–3494.

[115] Beeuwkes, J., Spitzen, J., Spoor, C., Van Leeuwen, J. & Takken, W., 2008 3-d flight behaviour of the malaria mosquito anopheles gambiae ss inside an odour plume. *Proc Neth Entomol Soc Meet* **19**, 137–146.

[116] Balebail, S., Raja, S. K. & Sane, S. P., 2019 Landing maneuvers of houseflies on vertical and inverted surfaces. *PloS one* **14**.

[117] Dickerson, A. K. & Hu, D. L., 2014. Mosquitoes actively remove drops deposited by fog and dew.

[118] van Breugel, F., Riffell, J., Fairhall, A. & Dickinson, M. H., 2015 Mosquitoes use vision to associate odor plumes with thermal targets. *Current Biology* **25**, 2123–2129.

[119] Hawkes, F. & Gibson, G., 2016 Seeing is believing: the nocturnal malarial mosquito anopheles coluzzii responds to visual host-cues when odour indicates a host is nearby. *Parasites & vectors* **9**, 320.

[120] Muir, L. E., Thorne, M. J. & Kay, B. H., 1992 Aedes aegypti (diptera: Culicidae) vision: spectral sensitivity and other perceptual parameters of the female eye. *Journal of medical Entomology* **29**, 278–281.

[121] Muir, L. E., Kay, B. H. & Thorne, M. J., 1992 Aedes aegypti (diptera: Culicidae) vision: response to stimuli from the optical environment. *Journal of medical entomology* **29**, 445–450.

[122] Mashayek, A. & Ashgriz, N., 2011 Dynamics of liquid droplets. In *Handbook of Atomization and Sprays*, pp. 97–123. Springer.

[123] Clift, R. & Gauvin, W., 1971 Motion of entrained particles in gas streams. *The Canadian Journal of Chemical Engineering* **49**, 439–448.

[124] Hasegawa, T., Suganuma, M. & Watanabe, H., 1997 Anomaly of excess pressure drops of the flow through very small orifices. *Physics of Fluids* **9**, 1–3.

[125] Anderson, T. L., 2017 *Fracture mechanics: fundamentals and applications*. CRC press.

[126] Fidelibus, M., Teixeira, A. & Davies, F., 2002 Mechanical properties of orange peel and fruit treated pre–harvest with gibberellic acid. *Transactions of the ASAE* **45**, 1057.

[127] Singh, K. K. & Reddy, B. S., 2006 Post-harvest physico-mechanical properties of orange peel and fruit. *Journal of Food Engineering* **73**, 112–120.

[128] Griffith, A. A., 1921 Vi. the phenomena of rupture and flow in solids. *Philosophical transactions of the royal society of london. Series A, containing papers of a mathematical or physical character* **221**, 163–198.

[129] Irwin, G. R., 1997 Analysis of stresses and strains near the end of a crack traversing a plate .

[130] Tada, H., Paris, P. C. & Irwin, G. R., 1973 The stress analysis of cracks. *Handbook, Del Research Corporation* **34**.

[131] Folias, E., 1970 On the theory of fracture of curved sheets. *Engineering fracture mechanics* **2**, 151–164.

[132] Holzapfel, A. G., 2000 *Nonlinear Solid Mechanics II*. John Wiley & Sons, Inc.

[133] Jiménez, N., Picó, R., Redondo, J., Camarena, F. & Roig, B., 2010 FDTD techniques applied to acoustic propagation in vegetable tissue: the elastodynamic behavior of the orange fruit. In *Proceedings of the 20th International Congress on Acoustics*. International Congress on Acoustics.

[134] Buehler, M. J., Abraham, F. F. & Gao, H., 2003 Hyperelasticity governs dynamic fracture at a critical length scale. *Nature* **426**, 141–146.

[135] Liu, T., Long, R. & Hui, C.-Y., 2014 The energy release rate of a pressurized crack in soft elastic materials: effects of surface tension and large deformation. *Soft Matter* **10**, 7723–7729.

[136] Patek, S. & Caldwell, R., 2005 Extreme impact and cavitation forces of a biological hammer: strike forces of the peacock mantis shrimp odontodactylus scyllarus. *Journal of Experimental Biology* **208**, 3655–3664.

[137] Yafetto, L., Carroll, L., Cui, Y., Davis, D. J., Fischer, M. W., Henterly, A. C., Kessler, J. D., Kilroy, H. A., Shidler, J. B. & Stolze-Rybczynski, J. L., 2008 The fastest flights in nature: high-speed spore discharge mechanisms among fungi. *PLoS One* **3**, e3237.

[138] Edwards, J., Whitaker, D., Klionsky, S. & Laskowski, M. J., 2005 Botany: a record-breaking pollen catapult. *Nature* **435**, 164–164.

[139] Rho, J.-Y., Kuhn-Spearing, L. & Zioupos, P., 1998 Mechanical properties and the hierarchical structure of bone. *Medical Engineering & Physics* **20**, 92–102.

[140] Barthelat, F., Tang, H., Zavattieri, P., Li, C.-M. & Espinosa, H., 2007 On the mechanics of mother-of-pearl: a key feature in the material hierarchical structure. *Journal of the Mechanics and Physics of Solids* **55**, 306–337.

[141] Cranford, S. W. & Buehler, M. J., 2012 *Biomateriomics*, volume 165. Springer Science & Business Media.

[142] Ashby, M., Gibson, L., Wegst, U. & Olive, R., 1995 The mechanical properties of natural materials. i. material property charts. In *Proceedings of the Royal Society of London A:*

Mathematical, Physical and Engineering Sciences, volume 450, pp. 123–140. The Royal Society.

[143] Chen, I. H., Yang, W. & Meyers, M. A., 2015 Leatherback sea turtle shell: A tough and flexible biological design. *Acta Biomaterialia* **28**, 2–12.

[144] Raabe, D., Sachs, C. & Romano, P., 2005 The crustacean exoskeleton as an example of a structurally and mechanically graded biological nanocomposite material. *Acta Materialia* **53**, 4281–4292.

[145] Ghosh, R., Ebrahimi, H. & Vaziri, A., 2014 Contact kinematics of biomimetic scales. *Applied Physics Letters* **105**, 233701.

[146] Liu, G., Ghosh, R., Mousanezhad, D., Vaziri, A. & Nayeb-Hashemi, H., 2017 Thermal conductivity of biomimetic leaf composite. *Journal of Composite Materials* p. 0021998317733316.

[147] Porter, M. M., Adriaens, D., Hatton, R. L., Meyers, M. A. & McKittrick, J., 2015 Why the seahorse tail is square. *Science* **349**, aaa6683.

[148] Zhang, Y., Yao, H., Ortiz, C., Xu, J. & Dao, M., 2012 Bio-inspired interfacial strengthening strategy through geometrically interlocking designs. *Journal of the Mechanical Behavior of Biomedical Materials* **15**, 70–77.

[149] Wegst, U. G., Bai, H., Saiz, E., Tomsia, A. P. & Ritchie, R. O., 2015 Bioinspired structural materials. *Nature Materials* **14**, 23–36.

[150] Fu, Y., Tippets, C. A., Donev, E. U. & Lopez, R., 2016 Structural colors: from natural to artificial systems. *Wiley Interdisciplinary Reviews: Nanomedicine and Nanobiotechnology* **8**, 758–775.

[151] Marvi, H. & Hu, D. L., 2012 Friction enhancement in concertina locomotion of snakes. *Journal of The Royal Society Interface* p. rsif20120132.

[152] Karaboga, D., 2005 An idea based on honey bee swarm for numerical optimization. Technical report, Technical report-tr06, Erciyes university, engineering faculty, computer engineering department.

[153] Vicsek, T. & Zafeiris, A., 2012 Collective motion. *Physics Reports* **517**, 71–140.

[154] Cavagna, A., Cimarelli, A., Giardina, I., Orlandi, A., Parisi, G., Procaccini, A., Santagati, R. & Stefanini, F., 2008 New statistical tools for analyzing the structure of animal groups. *Mathematical biosciences* **214**, 32–37.

[155] Olsen, D. & Murphy, D., 2018 (submitted) Random sequential addition simulations of animal aggregations. .

[156] Cambuí, D. S. & Rosas, A., 2012 Density induced transition in a school of fish. *Physica A: Statistical Mechanics and its Applications* **391**, 3908–3914.

[157] Becco, C., Vandewalle, N., Delcourt, J. & Poncin, P., 2006 Experimental evidences of a structural and dynamical transition in fish school. *Physica A: Statistical Mechanics and its Applications* **367**, 487–493.

[158] Hildenbrandt, H., Carere, C. & Hemelrijk, C. K., 2010 Self-organized aerial displays of thousands of starlings: a model. *Behavioral Ecology* **21**, 1349–1359.

[159] Hereford, J. M. & Blum, C., 2011 Flockopt: A new swarm optimization algorithm based on collective behavior of starling birds. In *NaBIC*, pp. 17–22.

[160] Ballerini, M., Cabibbo, N., Candelier, R., Cavagna, A., Cisbani, E., Giardina, I., Lecomte, V., Orlandi, A., Parisi, G., Procaccini, A. *et al.*, 2008 Interaction ruling animal collective

behavior depends on topological rather than metric distance: Evidence from a field study. *Proceedings of the national academy of sciences* **105**, 1232–1237.

[161] Brodie, J., 1976 The flight behaviour of starlings at a winter roost. *Br. Birds* **69**, 51–60.

[162] Topaz, C. M. & Bertozzi, A. L., 2004 Swarming patterns in a two-dimensional kinematic model for biological groups. *SIAM Journal on Applied Mathematics* **65**, 152–174.

[163] Topaz, C. M., Bernoff, A. J., Logan, S. & Toolson, W., 2008 A model for rolling swarms of locusts. *The European Physical Journal Special Topics* **157**, 93–109.

[164] Edelstein-Keshet, L., Watmough, J. & Grunbaum, D., 1998 Do travelling band solutions describe cohesive swarms? an investigation for migratory locusts. *Journal of mathematical biology* **36**, 515–549.

[165] Ariel, G. & Ayali, A., 2015 Locust collective motion and its modeling. *PLoS Computational Biology* **11**, e1004522.

[166] Edelstein-Keshet, L., 2001 Mathematical models of swarming and social aggregation. In *Proceedings of the 2001 International Symposium on Nonlinear Theory and Its Applications, Miyagi, Japan*, pp. 1–7. Citeseer.

[167] Tennenbaum, M., Liu, Z., Hu, D. & Fernandez-Nieves, A., 2016 Mechanics of fire ant aggregations. *Nature materials* **15**, 54.

[168] Phonekeo, S., Dave, T., Kern, M., Franklin, S. V. & Hu, D. L., 2016 Ant aggregations self-heal to compensate for the ringelmann effect. *Soft matter* **12**, 4214–4220.

[169] Baker, P. & Cooter, R., 1979 The natural flight of the migratory locust, locusta migratoria l. *Journal of Comparative Physiology A: Neuroethology, Sensory, Neural, and Behavioral Physiology* **131**, 79–87.

[170] Rainey, R. C. *et al.*, 1989 *Migration and meteorology. Flight behaviour and the atmospheric environment of locusts and other migrant pests.* Oxford University Press.

[171] Waloff, Z., Rainey, R. C. *et al.*, 1951 Field studies on factors affecting the displacements of desert locust swarms in eastern africa. *Field Studies on Factors affecting the Displacements of Desert Locust Swarms in eastern Africa.* .

[172] Buhl, J., Sumpter, D. J., Couzin, I. D., Hale, J. J., Despland, E., Miller, E. R. & Simpson, S. J., 2006 From disorder to order in marching locusts. *Science* **312**, 1402–1406.

[173] Bazazi, S., Buhl, J., Hale, J. J., Anstey, M. L., Sword, G. A., Simpson, S. J. & Couzin, I. D., 2008 Collective motion and cannibalism in locust migratory bands. *Current Biology* **18**, 735–739.

[174] Kennedy, J. S., 1951 The migration of the desert locust (schistocerca gregaria forsk.). i. the behaviour of swarms. ii. a theory of long-range migrations. *Philosophical Transactions of the Royal Society of London. Series B, Biological Sciences* pp. 163–290.

[175] Uvarov, B. *et al.*, 1977 *Grasshoppers and locusts. A handbook of general acridology Vol. 2. Behaviour, ecology, biogeography, population dynamics.* Centre for Overseas Pest Research.

[176] Rosinski, J. & Kerrigan, T., 1969 The role of aerosol particles in the formation of raindrops and hailstones in severe thunderstorms. *Journal of the Atmospheric Sciences* **26**, 695–715.

[177] Hassanpourfard, M., Nikakhtari, Z., Ghosh, R., Das, S., Thundat, T., Liu, Y. & Kumar, A., 2015 Bacterial floc mediated rapid streamer formation in creeping flows. *Scientific reports* **5**, 13070.

[178] Anstey, M. L., Rogers, S. M., Ott, S. R., Burrows, M. & Simpson, S. J., 2009 Serotonin mediates behavioral gregarization underlying swarm formation in desert locusts. *science* **323**, 627–630.

[179] Hughes, R. L., 2003 The flow of human crowds. *Annual Review of Fluid Mechanics* **35**, 169–182.

[180] Hughes, R. L., 2002 A continuum theory for the flow of pedestrians. *Transportation Research Part B: Methodological* **36**, 507–535.

[181] Smith, R., 1993 Volume flow rates of densely packed crowds. *Engineering for crowd safety* pp. 313–319.

[182] Nomura, Y., Saito, S., Ishiwata, R. & Sugiyama, Y., 2016 Hopf bifurcation analysis for a dissipative system with asymmetric interaction: Analytical explanation of a specific property of highway traffic. *Physical Review E* **93**, 012215.

[183] Gerhart, P. M., Gerhart, A. L. & Hochstein, J. I., 2016 *Munson's Fluid Mechanics*. Wiley Global Education.

[184] Lighthill, M. J. & Whitham, G., 1955 On kinematic waves i. flood movement in long rivers. *Proc. R. Soc. Lond. A* **229**, 281–316.

[185] Bonabeau, E., Theraulaz, G., Deneubourg, J.-L., Lioni, A., Libert, F., Sauwens, C. & Passera, L., 1998 Dripping faucet with ants. *Physical Review E* **57**, 5904.

[186] Theraulaz, G., Bonabeau, E., Sauwens, C., Deneubourg, J.-L., Lioni, A., Libert, F., Passera, L. & Solé, R., 2001 Model of droplet dynamics in the argentine ant linepithema humile (mayr). *Bulletin of mathematical biology* **63**, 1079–1093.

[187] Kirchner, A., Nishinari, K. & Schadschneider, A., 2003 Friction effects and clogging in a cellular automaton model for pedestrian dynamics. *Phys. Rev. E* **67**, 056122. (doi:10.1103/PhysRevE.67.056122).

[188] Frank, G. A. & Dorso, C. O., 2011 Room evacuation in the presence of an obstacle. *Physica A: Statistical Mechanics and its Applications* **390**, 2135–2145.

[189] Salamati, P. & Rahimi-Movaghar, V., 2016 Hajj stampede in Mina, 2015: need for intervention. *Archives of Trauma Research* **5**, e36308.

[190] Ahmed, Q. A., Arabi, Y. M. & Memish, Z. A., 2006 Health risks at the Hajj. *The Lancet* **367**, 1008–1015.

[191] Bagnold, R. A., 1954 Experiments on a gravity-free dispersion of large solid spheres in a newtonian fluid under shear. *Proceedings of the Royal Society of London A: Mathematical, Physical and Engineering Sciences* **225**, 49–63. ISSN 0080-4630. (doi:10.1098/rspa.1954.0186).

[192] Reynolds, C. W., 1987 Flocks, herds and schools: A distributed behavioral model. In *ACM SIGGRAPH Computer Graphics*, volume 21, pp. 25–34. ACM.

[193] Foster, P. C., Mlot, N. J., Lin, A. & Hu, D. L., 2014 Fire ants actively control spacing and orientation within self-assemblages. *Journal of Experimental Biology* **217**, 2089–2100.

[194] Hu, D., Phonekeo, S., Altshuler, E. & Brochard-Wyart, F., 2016 Entangled active matter: From cells to ants. *The European Physical Journal Special Topics* **225**, 629–649.

[195] Reid, C. R., Lutz, M. J., Powell, S., Kao, A. B., Couzin, I. D. & Garnier, S., 2015 Army ants dynamically adjust living bridges in response to a cost–benefit trade-off. *Proceedings of the National Academy of Sciences* **112**, 15113–15118.

[196] Nøttestad, L. & Axelsen, B. E., 1999 Herring schooling manoeuvres in response to killer whale attacks. *Canadian Journal of Zoology* **77**, 1540–1546.

[197] Pitman, R. L. & Durban, J. W., 2012 Cooperative hunting behavior, prey selectivity and prey handling by pack ice killer whales (orcinus orca), type b, in antarctic peninsula waters. *Marine Mammal Science* **28**, 16–36.

[198] Nøttestad, L., Fernö, A. & Axelsen, B. E., 2002 Digging in the deep: killer whales' advanced hunting tactic. *Polar Biology* **25**, 939–941.

[199] Clua, É. & Grosvalet, F., 2001 Mixed-species feeding aggregation of dolphins, large tunas and seabirds in the azores. *Aquatic Living Resources* **14**, 11–18.

[200] Attanasi, A., Cavagna, A., Del Castello, L., Giardina, I., Melillo, S., Parisi, L., Pohl, O., Rossaro, B., Shen, E., Silvestri, E. *et al.*, 2014 Collective behaviour without collective order in wild swarms of midges. *PLoS Computational Biology* **10**, e1003697.

[201] González, M. A., Alarcón-Elbal, P. M., Venter, G. J., López, S. *et al.*, 2017 Flight and swarming behaviour of culicoides species (diptera: Ceratopogonidae) on a livestock farm in northern spain. *Veterinaria italiana* **53**, 157–166.

[202] BLACKWELL, A., MORDUE, A. J., YOUNG, M. R. & MORDUE, W., 1992 The swarming behaviour of the scottish biting midge, culicoides impunctatus (diptera: Ceratopogonidae). *Ecological entomology* **17**, 319–325.

[203] Kelley, D. H. & Ouellette, N. T., 2013 Emergent dynamics of laboratory insect swarms. *Scientific reports* **3**, 1073.

[204] Downes, J., 1969 The swarming and mating flight of diptera. *Annual review of entomology* **14**, 271–298.

[205] Neems, R. M., Lazarus, J. & Mclachlan, A. J., 1992 Swarming behavior in male chironomid midges: a cost-benefit analysis. *Behavioral Ecology* **3**, 285–290.

[206] Okubo, A. & Chiang, H., 1974 An analysis of the kinematics of swarming ofanarete pritchardi kim (diptera: Cecidomyiidae). *Researches on population ecology* **16**, 1–42.

[207] McLachlan, A., Ladle, R. & Crompton, B., 2003 Predator–prey interactions on the wing: aerobatics and body size among dance flies and midges. *Animal Behaviour* **66**, 911–915.

[208] Rayleigh, L., 1878 On the instability of jets. *Proceedings of the London Mathematical Society* **1**, 4–13.

[209] Blaisot, J. & Adeline, S., 2003 Instabilities on a free falling jet under an internal flow breakup mode regime. *International Journal of Multiphase Flow* **29**, 629–653.

[210] Amini, G. & Dolatabadi, A., 2012 Axis-switching and breakup of low-speed elliptic liquid jets. *International Journal of Multiphase Flow* **42**, 96–103.

[211] Amini, G. & Dolatabadi, A., 2011 Capillary instability of elliptic liquid jets. *Physics of Fluids* **23**, 084109.

[212] van Hoeve, W., Gekle, S., Snoeijer, J. H., Versluis, M., Brenner, M. P. & Lohse, D., 2010 Breakup of diminutive Rayleigh jets. *Physics of Fluids* **22**.